

https://dspace.org/

An investigation into the causes of the differece in the corrosion behaviour of WC-Co and WC-VC-Co hardmetals

Sebeya, Thabo Thomas

2013-08-28
http://hdl.handle.net/10539/13100

Downloaded from a DSpace repository. https://dspace.org/

An Investigation into the Causes of the Difference in the Corrosion Behaviour of WC-Co and WC-VC-Co Hardmetals

Thabo Thomas Sebeya

A dissertation submitted to the Faculty of Engineering and the Built Environment, University of the Witwatersrand, Johannesburg, in fulfillment of the requirements for the degree of Master of Science in Engineering.

Johannesburg, 2013

Declaration

I, Thabo Sebeya, declare that the dissertation is my own work except where otherwise acknowledged. It is being submitted for the Degree of Master of Science in Engineering in the University of the Witwatersrand, Johannesburg. It has not been submitted previously at this or any other university for any degree or examination.

_____

(Candidate Signature)

_____ day of _____ (year)_____

Abstract

The aim of this work was to investigate the cause of the difference in the corrosion behaviour of WC-Co and WC-VC-Co alloys. Two alloys of WC-Co and WC-10VC-Co with increasing Co content of up to 30 wt% and a WC-67VC-10Co alloy were analyzed in 1N sulfuric acid at room temperature.

The binder composition of the alloys was analyzed by scanning and transmission electron microscopy with energy dispersive X-ray analysis, and X-ray diffraction. Additionally, density, hardness and magnetic properties were measured and potentiodynamic polarisation scans were undertaken. The following possible causes of the differences in corrosion behaviour were also investigated: differences in the composition of the binder, differences in the fcc/hcp Co ratio, and differences in the binder surface fraction exposed to the corrodant. The addition of VC to WC-Co lowered the density of the resulting component compared to straight WC-Co grades, due to the lower density of VC. The hardness of the specimens decreased with higher Co content, and increased with increasing VC content. Magnetic saturation measurements showed no significant difference between the WC-10Co and WC-67VC-10Co alloys, indicating that the high VC content did not change the solubility of W in Co. Rietveld analysis showed that the fcc/hcp Co ratio was higher in WC-10VC-30Co than in WC-30Co. Corrosion occurred mainly by the oxidation of the cobalt binder phase. A corrosion surface film formed only on the high VC content alloy. All the specimens exhibited pseudopassivity, but the extent of the pseudopassivity region for the WC-grade was 2.4 times than for the WC-VC-grade material. The corrosion current densities for WC-10Co and WC-67VC-10Co were similar, as were the magnetic saturation results. However, the fcc Co: hcp Co ratios of these and other samples, indicated that the high fcc: hcp ratio mirrored the greater corrosion depth, which occurred with VC additions and reduced with increasing Co additions. This is in disagreement with the conclusion of Broccardo (2003) that the corrosion current densities were similar.

Dedication

In memory of my mother
Mpho Alice Sebeya

She has been all supportive through my studies, sacrificing for me to study, but she was unfortunate not to see me graduating.

May God Bless Her, Rest in Peace Mom.

Acknowledgements

I wish to express my sincere gratitude and many thanks to the following:

Prof. S. B. Luyckx, for supervision, and for cheer, and being there when I was in a difficult situation.

Prof. L. A. Cornish, for supervision, and for discussions and making it possible for me.

Prof. M. J. Witcomb, for supervision, and for teaching me so many microscopy techniques.

Dr M. Sephton, for her patience in assisting me to solve corrosion studies and letting me use her equipment.

Dr. C. Machio, for discussions and guidance.

Dr Herman, for the Rietveld Refinement XRD data.

Mr A. Seema and Mrs C. Lalkhan of the Electron Microscope Unit at Wits University for the training provided in the use of the scanning electron microscope.

Mr A. Xoseka, for the metallographic preparation of my specimens and printing pictures from negatives. Mrs Loukie Adlem for assisting with the operation and use of FEGSEM at NMISA, Pretoria.

Thanks to my wife and family for supporting me, for understanding through thick and thin.

The financial support of the National Research Foundation (NRF), Vanadium Technology (Vanitec) and the South Africa-Norway Tertiary Education Development (SANTED), and to the DST/NRF Centre of Excellence in Strong Materials is gratefully acknowledged.

Not to forget, thanks to almighty God (Heavenly Father).

Table of Contents

Chapter 1 - Introduction 1

Chapter 2 - Literature review 5

2.1. Cemented carbides 5

2.2. Structure of WC-Co 6

2.3. Properties of VC and WC 8

2.4. Hardmetal incorporating vanadium carbide 9

2.5. Corrosion of WC-based hardmetals 133

Chapter 3 - Experimental Procedure 225

3.1. Sample selection and preparation 25

3.2. X-ray diffraction 26

3.3. Scanning electron microscopy 27

3.4. Image analysis 28

3.5. Transmission electron microscopy 28

3.5.1 Lattice parameter determination using the TEM 28

3.5.2 EDX analysis in the TEM 31

3.5.2.1. Plasma cleaner 32

3.5.2.2. Low temperature, double tilt TEM holder 32

3.6. Density measurements 32

3.7. Hardness measurements 33

3.8. Magnetic saturation measurements 33

3.9. Corrosion tests 34

3.9.1. Electrochemical tests 34

3.9.2. Immersion tests (Broccardo, 2003) 36

Chapter 4 - Results 37

4.1. Scanning electron microscopy (SEM) 37

4.1.1. Microstructural analysis 37
4.2. Density measurements 39
4.3. Hardness measurements 411
4.4. Determination of W and V content in the binder 43
4.4.1. Energy dispersive X-ray analysis (EDX) 43
4.4.2. Magnetic saturation 46
4.5. Determination of fcc-Co/hcp-Co ratio in the binder 47
4.5.1. X-ray diffraction (XRD) 47
4.5.2. TEM microstructure 53
4.5.3. Lattice parameter determination using the TEM 56
4.6. Results of corrosion tests 57
4.6.1. Electrochemical corrosion tests 57
4.6.2. Immersion corrosion testing 62
4.6.3. Depth of corroded layer on immersion corrosion samples 674
Chapter 5 - Discussion 69
5.1. Characteristics of the test specimens 69
5.1.1. Density 69
5.1.2. Hardness test 69
5.1.3. Magnetic saturation 71
5.1.4. Microstructures of specimens 72
5.1.5. Specimen phase composition 73
5.1.6. Electrochemical corrosion tests 74
5.2. Hypotheses 76
5.2.1. Composition differences in the binder 767
5.2.2. Difference in the fcc-Co/hcp-Co ratio 778

5.2.3. Difference in the Co surface fraction exposed to corrosion 78

Chapter 6 - Conclusions 80

References 82

Appendix A - X-ray diffraction analysis 88

Appendix B - Publications from this work 92

List of Figures

1.1. Schematic representation of the effect of VC additions on the corrosion rate of WC-Co materials according to Broccardo (2003). ……..……2

2.1. The hcp structure [www.chem.ox.uk/heyes/structure_of soilds/Coords/79 Met-hcp.cmdf]. ……...7

2.2. The fcc structure [www.chem.ox.ac.uk/heyes/structure_of_solids/Coords/ Met-hcp.cmdf]. .8

2.3. SEM image of the layer formed on the surface of the WC-Co composite after a full polarization scan (Human and Exner, 1996). ……15

2.4. Effect of magnetic saturation, 4πr, on electrochemical behavior of cemented carbides with different cobalt binder content in aerated 1N H_2SO4 (Mori, 2003). ……16

2.5. Corrosion rate from electrochemical tests determined by Tafel extrapolation (Broccardo *et al*., 2003). ……..18

2.6. Potentiodynamic scans of WC-10Co alloys in 1M H_2SO_4 with increasing Ru additions and 0.4VC (Potgieter, 2011). ……...20

2.7. The effect of increasing ruthenium on corrosion rate of WC-Co alloys in 1M H_2SO_4 (Potgieter, 2011). ……..21

2.8. Cyclic polarization curves, showing the pitting loop for AISI H12 tool steel samples coated with VC films at 20 °C with different C/V ratios in 3.5% NaCl solution. ……...…….23

2.9. SEM microstructures of a AISI H12 tool steel sample coated with a 200 nm thick VC film, after corrosion in 3.5% NaCl solution. The images show the pits (a) and the details of one pit with the exposed substrate in the bottom (b). ……..…….24

3.1. Electron diffraction pattern from an aluminium thin foil showing the (600) ring, the outer of the doublet, used as a standard to calculate the camera, λL. ……29

3.2. zone axis pattern from a WC grain in the WC-10VC-30C0 alloy. …….……30

3.3. Identification of the WC spots in Figure 3.2. ……...……..30

3.4. pattern of an fcc Co grain in the WC-10VC-30Co alloy, with faint spots derived from the stacking faults which are hcp Co. 31

3.5. Corrosion cell used for the experiments. 35

4.1. SEM image in backscattered electron mode of the WC-10Co alloy, showing WC (light) and Co (dark). 38

4.2. SEM image in backscattered electron mode of the WC-30Co alloy, showing WC (light) and Co (dark). 38

4.3. SEM image in backscattered electron mode of the WC-67VC-10Co alloy, showing Co (light), (V,W,Co)C (medium) and pores (dark). 38

4.4. SEM image in backscattered electron mode of the WC-10VC-30Co alloy, showing WC (light), (V,W,Co)C (medium) and Co (dark). 38

4.5. Optical micrograph of the WC-67VC-10Co alloy showing cracks radiating from an indentation produced at a load of 30kg. ……42

4.6. Optical micrograph of the WC-10Co alloy showing slightly curved edges of the hardness indentation, and no evidence of cracking at a 30kg load. 42

4.7. SEM image in secondary electron mode of the WC-67VC-10Co alloy showing the contamination spot (centre) resulting from a EDX spot analysis of a (V,W,Co)C grain. 44

4.8. EDX spectrum from the (V,W,Co)C phase, showing a small amount of Co. 45

4.9. XRD pattern of the WC-10Co alloy. 47

4.10. XRD pattern from the WC-67VC-10Co alloy showing the absence of any WC phase. 48

4.11. XRD pattern of WC-30Co showing the presence of fcc-Co and hcp-Co. 48

4.12. XRD pattern of WC-10VC-30Co showing the presence of fcc-Co and hcp-Co. 49

4.13. Rietveld pattern of WC-VC-Co alloy showing V_8C_7 (red lines), measured data (blue) and calculated data (green). 50

4.14. Rietveld pattern of WC-VC-Co alloy showingWC (red lines), measured data (blue) and calculated data (green). 50

4.15. Rietveld pattern showing the difference between the calculated and measured data (red) and hcp Co (black lines). 50

4.16. Rietveld pattern showing the difference between the calculated and measured data (red) and fcc Co (black lines). 51

4.17. TEM image of the WC-30Co alloy showing stacking faults in Co. 53

4.18. TEM image of the WC-10VC-30Co alloy showing parallel stacking faults in Co. 54

4.19. TEM image of the WC-30Co alloy showing the triangular cross-section of some WC grains containing faults and dislocations. 54

4.20. TEM image of the WC-30Co alloy showing dislocations in the WC grains. 55

4.21. TEM image of the WC-10VC-30Co alloy showing dislocations and voids (V) in the WC grains. 55

4.22. Low magnification TEM image of the WC-10VC-30Co alloy, showing large (V,W,Co)C grains and very small WC grains. 56

4.23. (a) TEM diffraction pattern of the mixed carbide grain, (V,W,Co)C, in the WC-10VC-30Co alloy, (b) image in (a) after being subjected to a high pass band filter and auto contrast/brightness to emphasise the ordering intensities. 57

4.24. Potentiodynamic polarisation scans obtained from one specimen of WC-10Co alloy, after each re-polishing, showing reproducibility. 58

4.25. Potentiodynamic polarisation scans obtained from the one of WC-67VC-10Co alloy, after each re-polishing, showing reproducibility. 58

4.26. SEM image in backscattered electron mode of the WC-10Co alloy, before electrochemical corrosion testing, showing WC (light) and Co (dark). 60

4.27. SEM image in secondary electron mode of the WC-10Co alloy, after electrochemical corrosion testing, showing some attack on WC grains (light) as well as the removal of Co. 60

4.28. SEM image in secondary electron mode of the WC-10Co alloy, after electrochemical corrosion testing, showing some attack on WC grains (light) as well as the removal of Co. 61

4.29. SEM image in backscattered electron mode of the WC-67VC-10Co alloy, before electrochemical corrosion testing, showing Co (light), (V,W,Co)C (medium) and defects (dark). 61

4.30. SEM image in secondary electron mode of the WC-67VC-10Co alloy, after electrochemical corrosion testing, showing no Co and a corrosion product. 62

4.31. SEM image in backscattered electron mode of the corroded WC-10Co alloy, showing no Co (holes (dark)), and WC (light). 63

4.32. SEM image in backscattered electron mode of the corroded WC-10VC-10Co alloy, showing no Co (holes (dark)), and no attack on the WC (light) and (V,W,Co)C(medium grey) .63

4.33. SEM image in backscattered electron mode of the corroded WC-12Co alloy, showing no Co (holes (dark)) and WC (light). 64

4.34. SEM image in backscattered electron mode of the corroded WC-10VC-12Co alloy showing no Co (holes (dark)), and no attack on the WC (light) and (V,W,Co)C (medium). 64

4.35. SEM image in backscattered electron mode of the corroded WC-10VC-15Co alloy showing no Co (holes (dark)) and no attack on WC and (V,W,Co)C. 65

4.36. SEM image in backscattered electron mode of the corroded WC-30Co alloy showing no Co (holes (dark)) and WC (light). 65

4.37. SEM image in backscattered electron mode of the corroded WC-10VC-30Co alloy, showing no Co (holes (dark)), and no attack on WC(light) and (V,W,Co)C (medium). 66

4.38. SEM image in backscattered electron mode of a polished cross section of the WC-9Co alloy showing the corroded and the uncorroded regions (Broccardo, 2003). 66

4.39. Comparison of the corrosion depth of the WC-Co alloys with cobalt content (wt%). 68

4.40. Comparison of the corrosion depth of the WC-10VC-Co alloys with cobalt content (wt%). 68

5.1. Schematic diagram showing the indentation from a pyramidal indenter in a material that work hardens, with arrows representing directions of easy flow (Tabor, 1970). 70

List of Tables

2.1. The major developments in WC-base hardmetals (Brookes, 1992). 6

2.2. Properties of WC and VC (Exner, 1979). 9

2.3. Hardness and toughness of WC-VC-Co alloys with varying Co content and grain size (Luyckx, 1997). 10

2.4. Costing for the conventional WC-Co and WC-VC-Co materials based on the same cobalt content (Whitefield, 2011). ……..……..…12

2.5. Corrosion parameters of the various WC-VC-Co samples in 1M HCl and 1M H_2SO_4 (Konadu *et al.*, 2010). 19

3.1. Starting powder composition for each sample. 25

4.1. Phases present in alloys determined using backscattered SEM images and EDX. ……...39

*4.2.*Comparison of densities. 40

4.3. Hardness values of the alloys using a 30kg load, and a microhardness value using a 300g load. 41

4.4. Average overall composition (wt%) excluding carbon of the alloys measured by EDX in the JEOL 840 SEM. 43

4.5. Composition (wt%), excluding carbon of the mixed carbide and binder phases, as measured by EDX in the Jeol 840 SEM. 44

4.6. Composition (at.%) of the mixed carbide phases, as measured by EDX in the SEM. 45

4.7. Mixed carbide compositions in the WC-VC-Co alloys of different Co content, ignoring carbon (Witcomb *et al*., 1997) obtained by EDX in TEM. ……...46

4.8. Magnetic saturation measurements. 46

4.9. Quantitative analysis of chemical composition of the phases present in the alloys (wt%). .. 51

4.10. Lattice parameters of the phases present in the alloys obtained from Rietveld analysis (nm). 52

4.11. Ratio of fcc-Co to hcp-Co in the alloys. 53

4.12. Lattice parameters of the phases in the WC-10VC-30Co alloy. 56

4.13. Electrochemical corrosion parameters. 59

4.14. Depth of the corroded layers on the immersion tested samples..... 67

Chapter 1
Introduction

The study of cemented carbides has become of worldwide interest since they were first produced commercially by powder metallurgy techniques by Krupp in Germany under the trade name *Widia* (*wie Diamat*-like diamond) in the 1930s (Brookes, 1998). WC-Co is widely used for mining tools, metal and wood cutting tools, and in some areas where wear is too excessive for other materials. These applications often occur in a corrosive environment.

The original cemented carbides comprised a hard tungsten carbide phase embedded in a more ductile binder phase, usually cobalt (Brookes, 1992). The cobalt can be substituted with other metals such as chromium, nickel, iron, or a combination of these in order to improve toughness and corrosion resistance (Brookes, 1992). Recently, additions of ruthenium have also been shown to also improve WC-Co corrosion properties in sulfuric acid (Shing, (2001); Potgieter *et al*. (2011)).

The addition of VC to WC-Co alloys has yielded some properties which are better than those of conventional WC-Co alloys. Small amounts (~ 1%) of VC are commonly added to the WC-Co alloys as a grain refiner (Fukatsu *et al*. (1991); Moyle and Northrop, 1989), while the addition of a larger amount has been shown to produce WC-VC-Co materials which are suitable for applications in abrasive and erosive environments due to their higher hardness (Luyckx, 1997). The corrosion resistance of WC-VC-Co has also been found to be superior to that of conventional WC-Co alloys of equal cobalt content (Human, 1994; Schollenberger, 1996; Broccardo, 2003). During initial investigations into the corrosion behaviour of a WC-10VC-10Co sample, the material maintained its shape after immersion corrosion tests in sulfuric acid, while WC-10Co disintegrated after the same length of time, three days (Manyatsa, 2000). Therefore, it appeared to be advantageous to add VC to WC-Co to improve the corrosion resistance. In line with this thinking, Broccardo (2003) performed tests on WC-10VC-Co with increasing cobalt contents. Broccardo (2003) observed that the corrosion rate of WC-VC-Co decreased with increasing cobalt binder content, while the corrosion rate of WC-Co increased with cobalt content (Figure 1.1). Unlike Broccardo (2003), who kept the VC content constant

and varied the Co content of the WC-Co test specimens, Konadu *et al.* (2010) kept the Co constant and varied the VC content and observed that the corrosion current densities in hydrochloric and sulfuric acids increased for VC contents used for WC grain size refinement and then decreased with increasing VC content.

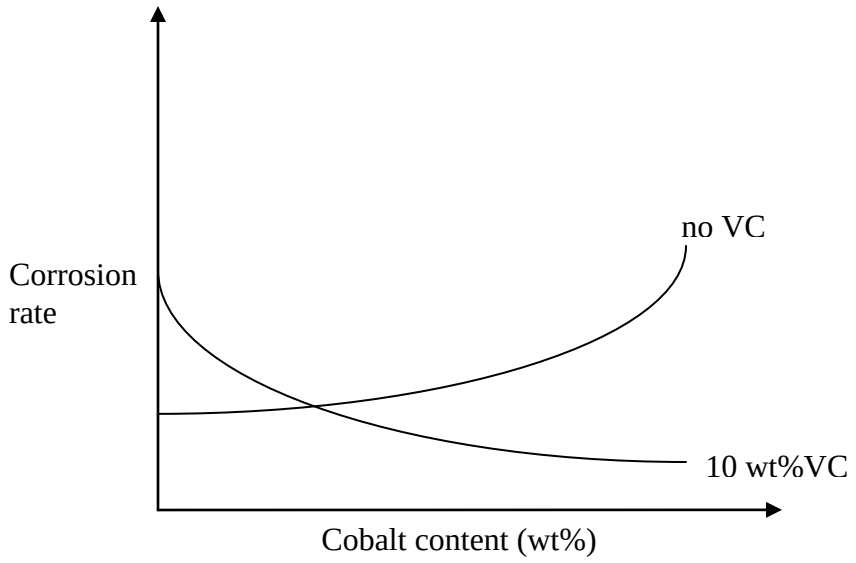


Figure 1.1. Schematic representation of the effect of VC additions on the corrosion rate of WC-Co materials according to Broccardo (2003).

The graph in Figure 1.1 is only a schematic representation, because there were difficulties associated with the measurements of the weight loss of sample Broccardo (2003). Since the corrosion product could have been trapped under the surface of the WC skeleton, these problems were also reported by Schollenberger (1991).

This work is a follow-up on the investigation undertaken by Broccardo (2003). In his study, Broccardo (2003) tested the corrosion resistance by two methods: electrochemical (potentiodynamic polarisation resistance) and immersion tests. However, the cause of the difference in the corrosion rate of the two hardmetals (WC-Co and WC-VC-Co) was not explained. The present project was an attempt to find the cause of this difference. Since the largest difference in corrosion behaviour was found in materials with a high cobalt content (30 wt%), it was expected that the cause of the difference in behaviour would be most noticeable in

these materials. Therefore, the materials investigated in this project were WC-30Co and WC-10VC-30Co. The compositions indicated here refer to the starting powders in weight percent and not to the final phases formed during the preparation of the materials. During the sintering process, with WC and Co, pure VC transforms into the mixed carbide phase, (V,W,Co)C (Luyckx, 1997).

In order to clarify and explain the difference of the corrosion behaviour between the WC-Co and WC-VC-Co alloys, three hypotheses were formulated on the basis of previous work and related literature (Schuhmacher and Ostermann (1973); Tomlinson and Linzell (1988); Human (1994); Exner 1996; Mori (2003); Broccardo (2003)).

The first hypothesis was that the composition of the binder should be different in the WC-Co and WC-VC-Co alloys, and this would affect the corrosion resistance. Thus, it was necessary to determine the W and V content in the binder of the WC-VC-Co alloy and the W content of the binder of the WC-Co alloy. In order to prove or disprove this hypothesis, transmission and scanning electron microscopy (TEM and SEM), energy dispersive X-ray spectroscopy (EDX) and magnetic saturation measurements were employed.

The second hypothesis was that the difference in corrosion behaviour between the WC-Co and WC-VC-Co alloys was caused by a higher fcc/hcp Co ratio in the alloys with VC, since it has been shown that cubic Co is more corrosion resistant than hexagonal cobalt (Human, 1994; Broccardo, 2003). X-ray diffractometry was employed to test this reasoning, while TEM studies were used to try to determine the stacking fault densities in the two binders.

The third hypothesis was that the lower corrosion rate of the WC-VC-Co alloys observed in literature (Broccardo, 2003) was due to the fact that VC-containing materials have less Co volume percentage for equal Co weight percentage. This implies that most of the corrosion stems from the Co and little derives from the (V,W,Co)C and WC. In order to verify this hypothesis, corrosion tests were carried out and the volume fraction of each phase in each alloy was evaluated.

This work contributes to the WC-Co corrosion literature in one way. It focuses on how a third carbide, VC affects the binder composition and how the composition affects the corrosion properties of the hard metal. As already noted, Konadu *et al*. (2010) reported on the effect of increasing VC content on the corrosion behaviour of WC-Co in acidic media (HCl and H_2SO_4) and aimed to understand whether the VC participated in the corrosion processes. Shing *et al*. (2001) and recently Potgieter *et al*. (2011), on the other hand, physically introduced a third element, Ru, in to the Co binder. The work could have the potential to improve the economy of South Africa by finding new applications for vanadium, which is produced in large amounts in South Africa.

Chapter 2

Literature review

This chapter summarizes the background to WC-cemented carbides which are often called ‘hardmetals’. The origin, production route, development and properties of hardmetals are presented, as well as the structure of the binder at different temperatures, and the corrosion dependence on the ratio of cubic-Co to hexagonal-Co in the binder. A summary is given of the improvements to the corrosion behaviour of WC-Co when adding vanadium carbide at different WC and Co contents.

2.1. Cemented carbides

Cemented carbides are made of hard carbide particles cemented together with a ductile metal such as cobalt or nickel. They are generally called ‘hardmetals’ because of their high hardness, typically of the order of 1500 HV30, and their metallic lustre. Such materials are used mainly in metal cutting (drilling, milling), wear resistance tools (drawing dies, compression tools) and mining tools (Brookes, 1992).

The carbide phase provides the hardness, while the binder contributes to toughness. The combination of these phases determines the impact resistance and the overall hardness of the tools. For example, the higher the cobalt content of the tools, the higher the impact resistance, while, in contrast, increasing tungsten carbide makes the tools harder, but decreases the impact resistance. An analogy is that the tungsten carbide behaves as "bricks" and the binder material as the "mortar". Cemented carbides were discovered about 80 years ago and since then, their development and production has grown rapidly. Of the carbides, tungsten carbide based hardmetals have become the most important group. The historical development and improvement in properties of hardmetals based on tungsten carbide is summarized in Table 2.1 (Brookes, 1992).

Table 2.1. The major developments in WC-base hardmetals (Brookes, 1992).

Date	**WC-base sintered carbides**
1923-25	WC-Co
1929-31	WC-TiC-Co
1930-31	WC-TaC(VC,NbC)-Co
1933	WC-TiC-TaC(NbC)-Co
1938	WC-Cr_3C_2-Co
1947-70	Sub-micronmetre WC-Cr_3C_2-Co
1956	WC-TiC-Ta(Nb)-C r_3C_2-Co
1959	WC-TiC-HfC-Co
1968-69	WC-TiC-Ta(Nb)-HfC-Co
1968-69	WC-TiC-Nb(Ta)-HfC-Co
1965-78	TiC, TiN, Ti(C,N), HfC, HfN and Al_2O_3 Chemical vapor deposition (CVD) coatings on a WC-based hardmetal
1965-75	Hot isostatic pressing
1969-71	Thermochemical surface hardening
1974-77	Polycrystalline diamond (PCD) coatings on a WC-based hardmetal
1973-78	Multi-carbide, carbonitride/nitride and multiple carbide/carbonitride/nitride/ oxide coatings
1976-79	Complex carbides with Ru additions
1981	Many TiN coatings with AlON (Aluminium oxynitrides layers)
1992-96	CVD diamond coatings
1995-96	CVD cubic boron nitride coating
2000	WC-(V,W)C-Co

2.2. Structure of WC-Co

The structure of the WC-Co hardmetal is crystalline with phases of WC and Co. WC has the hexagonal closed packed (hcp) structure. The cobalt possesses a hexagonal structure which is stable at room temperature and a cubic structure above 417°C. These structures are illustrated in

Figures 2.1 and 2.2. The importance of the cobalt structure will become apparent in Section 2.5 in connection with the corrosion of hardmetals and from X-ray diffraction results in Chapter 4.

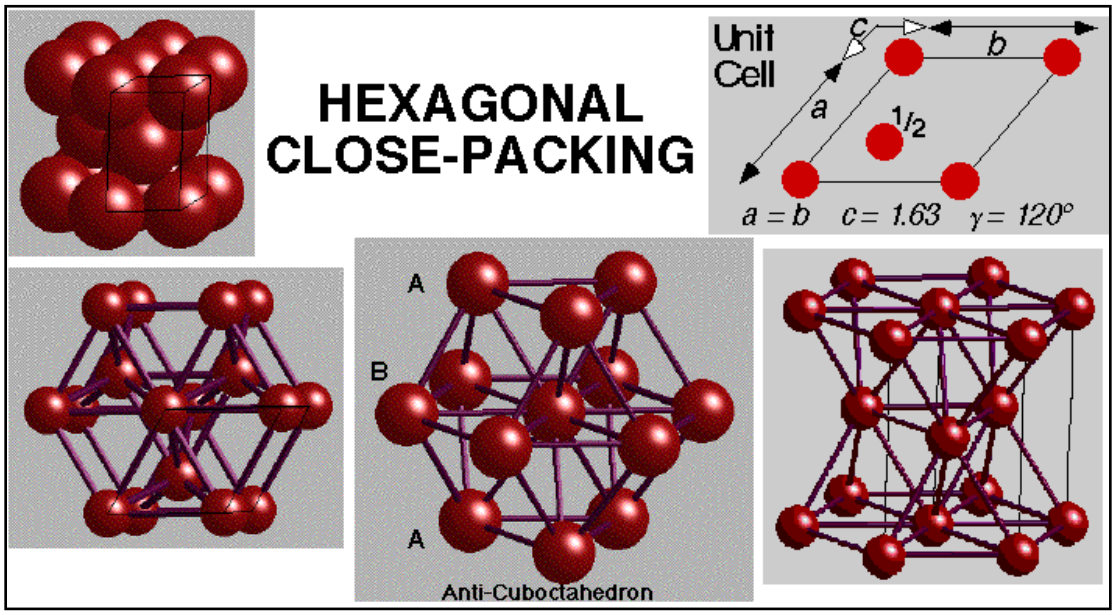


Figure 2.1.The hcp structure
[http://www.chem.ox.ac.uk/icl/heyes/structure_of_solids/lecture1/lec1.html].

The cobalt hexagonal close packed crystal structure belongs to the space group P63/mmc. Figure 2.1 shows the hexagonal unit cell with characteristics:

- $a = b$, $c = 1.63a$, $\alpha = \beta = 90°$, $\gamma = 120°$
- 2 atoms in the unit cell: (0, 0, 0) ($^2/_3$, $^1/_3$, $^1/_2$)

For fcc, face-centred cubic, the characteristics are:

- $a = b = c$, $\alpha = \beta = \gamma = 90°$,
- 4 atoms in the unit cell: (0, 0, 0) (0, $^1/_2$, $^1/_2$) ($^1/_2$, 0, $^1/_2$) ($^1/_2$, $^1/_2$, 0)

From these four atom positions, fcc symmetry produces all the other atom sites. The atom stacking arrangement of the close-packed layers ABABAB is hcp, while the ABCABC stacking is fcc, Figure 2.2. The hcp and fcc structures both have a coordination number of 12 and the same atomic packing factors of 0.74.

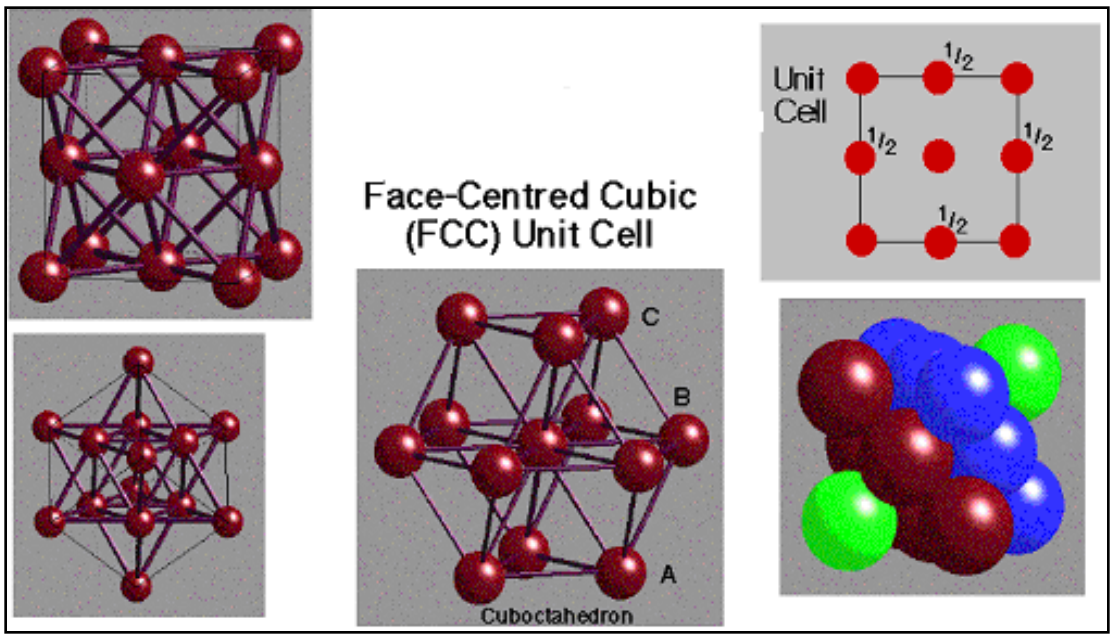


Figure 2.2. The fcc structure
[http://www.chem.ox.ac.uk/icl/heyes/structure_of_solids/lecture1/lec1.html].

Cobalt metal that has been cooled from T > 500°C partially retains a close-packed structure with a random stacking sequence. "Normal" hcp cobalt is actually 90% ABABAB and 10% ABCABC - *i.e.* non-ideal hcp (www.chem.ox.ac.uk/heyes/structure_of_solids/Coords/Met-hcp.cmdf).

2.3. Properties of VC and WC

Table 2.2 lists the properties of WC and VC which are most relevant to the performance of cemented carbides in their conventional applications, ranging from metal cutting to rock drilling, and from wear resistance to high pressure components (Brookes, 1992). The hardness of VC at room temperature is appreciably higher than the hardness of WC. This also implies that VC is more brittle than WC. The solubility of VC in cobalt is less than that of WC, which may imply that VC has less resistance to chemical wear. The wettability of VC by cobalt is inferior to the wettability of WC, and the thermal conductivity and resistance to oxidation of VC is inferior to that of WC (Exner, 1979).

Table 2.2. Properties of WC and VC (Exner, 1979).

Property	**WC**	**VC**
Density ($g.cm^{-3}$)	15.7	5.7
Crystal structure	Hexagonal	Cubic
Lattice parameter (nm)	a = 2.91, c = 2.84	a = 0.422
Melting temperature (°C)	2800	2700
Nominal carbon content (wt%)	6.13	19.08
Hardness (HV 0.05)	2200	2900
Elastic modulus (GPa)	696	422
Thermal expansion coefficient ($K^{-1}.10^{-6}$)	5.2	7.2
Solubility in Co at 1250 °C (wt%)	9.0	6.0

2.4. Hardmetal incorporating vanadium carbide

VC is commonly added to fine grained hardmetals, in small amounts (~1wt%), as a WC grain refiner/WC grain growth inhibitor (Fukatsu *et al*. (1991); Moyle and Northrop, 1989), but Luyckx *et al.* (1997) experimented with larger amounts of VC (10 wt%) and showed that the WC-VC-Co alloys were suitable for applications in abrasive and corrosive environments, on account of their improved hardness, and the fact that their corrosion resistance was superior to those of conventional WC-Co alloys of equal cobalt content. Decreasing the VC grain size helps in improving properties of the WC-VC-Co alloys such as hardness, toughness, erosion resistance and abrasion resistance. During the sintering of the WC-Co alloys, control of the WC grains is one of the primary concerns, since the average grain size and size distribution have a critical effect on many physical properties (Luyckx *et al.*, 1997).

Luyckx *et al.* (1997) also studied the properties of WC-VC-10Co alloys produced using two types of vanadium powders, V_2O_5 and V_8C_7, as starting materials. The alloys were sintered at 1330°C and were found to contain eta phase (Co_3W_3C or Co_4W_2C or Co_6W_6C). The presence of the eta phase was attributed to a high level of oxygen in the powders, which removed carbon and made the material more brittle. The hardness values of the materials produced from both V_2O_5 and V_8C_7 were similar and significantly higher than for the conventional WC-Co alloy of equal cobalt content. The toughness of the material manufactured from V_8C_7 powder was higher than

that made from V_2O_5 powder due to less eta phase, and the toughness of both materials was higher than that of WC-Co alloys of equal hardness. This material was compared with WC-10Co and WC-6Co. The results are summarised in Table 2.3 (Luyckx *et al.*, 1997).

Table 2.3. Hardness and toughness of WC-VC-Co alloys with varying Co content and grain size (Luyckx, 1997).

Alloy	**Average hardness (HV_{30})**	**Average toughness ($MNm^{-3/2}$)**
WC-10VC-10Co from V_2O_5 (with η phase particles)	1512	9.1
WC-10VC-10Co from V_8C_7 (with η phase particles)	1581	11.4
WC-6Co (without η phase)	1574	9.5
WC-6Co (fine grain size)	1550	10.4
WC-10Co (fine grain size)	1350	12.6
WC-10Co (coarse grain size)	1230	15.3
WC-11Co (fine grain size)	1330	13.4

Luyckx *et al.* (1996) showed that the microstructures of all grades of WC-VC-Co with different cobalt percentages exhibited three phases, namely: WC, (V,W)C and (Co), where (Co) is the solid solution based on cobalt. Obbard *et al.* (2001) determined the field boundaries for the formation of WC-(V,W)C_x-Co materials without eta phase or free carbon in the temperature range of the sintering process.

Lee *et al.* (2003) reported that when VC was added to inhibit grain growth, the crystal shape of WC grains changed from triangular prisms with truncated corners in WC-Co samples to triangular prisms without truncation. This shape change was related to the variation of surface energy, which has a significant influence on the coarsening process of WC grains.

Whitefield (2011) and Whitefield and Luyckx *et al.* (1997, 1999, 2000), used 10wt% VC as a substitute for the WC and this partial replacement was a novel approach in producing a new type of hardmetal alloy for industrial and mining applications. The work related to the optimisation

and evaluation of this new WC-VC-Co hardmetal. The production route of the material was by powder metallurgy techniques due to the high melting points of the tungsten carbide and vanadium carbide. Critical process operations such as milling and sintering were closely monitored and optimised. After sintering, the properties of the hardmetal were evaluated using standard hardmetal quality control procedures, as well as additional techniques such as field emission scanning electron microscopy and transmission electron microscopy. Field testing was also undertaken to determine how this material would compare to other commercially available materials.

The materials produced possessed some unique properties. The (W,V)C phase was found to contain Co and should therefore be more correctly called (W,V,Co)C – mixed carbide phase (Whitefield *et al.,* 1997). Initially, the material was prone to crack initiation from and propagation through the mixed carbide phase. This problem was overcome by using starting powders with a finer grain size, or by refining the powders by extended milling times. This reduced the grain size of the (W,V,Co)C in the sintered material to less than the critical value for crack initiation and growth.

The hardness of the WC-VC-Co materials was found to be superior to conventional Nanograde (approximately 500µm) WC-Co materials with the same cobalt content (Whitefield *et al.*, 1997). The toughness of the WC-VC-Co materials was found to be similar or greater than Nanograde WC-Co alloys with approximately the same hardness. The density of the materials produced with 10wt% Co and 10wt% VC were 2 $g.cm^{-3}$ less dense than for conventional Nanograde WC-Co grades with the same cobalt content. This would give significant weight savings in most applications.

Field testing was done at two different mines, one mining iron ore and the other silica, Whitefield (2011). On the silica mine, the results were disappointing as the WC-VC-Co was worn away quickly in comparison to the commercial grade of carbide used. It was noted that the grade normally used had a nickel binder, providing significant improvement in corrosion resistance over the WC-VC-Co with only a cobalt binder. For a fair comparison, a Ni binder should have been used for the VC alloy. On the iron ore mine, the WC-VC-Co materials

performed well and gave the same life as the grade of material then used. Due to the concern of chipping and damaging the conveyor belt, the WC-VC-Co grade had 12 wt% cobalt binder, whereas the grade normally used was WC with 6-10 wt% Co, without nickel, as the environment did not have a low pH as the silica mine. If a WC-VC-10wt% Co material had been used, the resistance would have been superior to the grade currently used. Thus, the high Co content compromised the results.

An analysis was also conducted to determine whether there was any cost advantage to these WC-VC-Co materials, since only the raw materials differ and processing is the same, the cost of the production would be equal, but overall there is a slightly greater expense for the WC-VC-Co materials as the VC is of significantly higher cost than the WC (Table 2.4).

Table 2.4. Costing for the conventional WC-Co and WC-VC-Co materials based on the same cobalt content (Whitefield, 2011).

Powder costs	**WC-10 wt%Co**	**WC-10 wt%VC-10 wt%Co**
Tungsten carbide price 250 units/kg	225	180
Vanadium carbide price 725 units/kg	0	72.5
Cobalt price 350 units/kg	35	35
Raw material costs for 1kg	260	287.5
Processing costs		
Milling price 4 units/hour	24	24
Spray drying price 15 units/hour	15	15
Pressing price 150 units/kg	150	150
Sintering price 120 units/kg	120	120
Brazing price 300 units/kg	300	300
Processing costs for 1kg sintered parts	609	609
Total cost to produce 1kg of parts	869	896.5

2.5. Corrosion of WC-based hardmetals

The corrosion behaviour of WC-Co and how it is affected by additions of VC forms the main focus of this research; therefore the most significant literature pertaining to the corrosion of these hardmetals is discussed in this section.

Corrosion of WC-Co hardmetals occurs mainly by the oxidation of the cobalt binder phase (Human, 1994). It is therefore expected that the overall corrosive failure of the hardmetal occurs by the selective dissolution of the binder phase, leaving behind a WC skeleton. The tungsten carbide phase can also corrode, but this only seems to be significant at very high potentials. Equations 2.1 and 2.2 show the corrosion process (Human, 1994):

$$Co \rightarrow Co^{2+} + 2e^{-} \qquad 2.1$$

$$WC + 5H_2O \rightarrow WO_3 + CO_2 + 10H^{+} + 10e^{-} \qquad 2.2$$

Human (1994) found that the corrosion of binder phase was strongly influenced by tungsten dissolution in the binder during liquid phase sintering. He also found that corrosion currents at potentials up to ~800 mV vs. Saturate Calomel Reference Electrode (SCE) were primarily due to the oxidation of cobalt. Human compared pure cobalt with the cobalt binder in WC-Co alloys and found that there was a difference in corrosion behaviour of the two cobalt phases. Due to the presence of tungsten and carbon in the cobalt binder: pure Co did not passivate, while the Co binder in WC-Co underwent pseudo-passivation under potentiodynamic polarization conditions. Thus, one might expect that the corrosion behaviour of the WC-VC-Co alloy would be different from the WC-Co alloy because of the added presence of vanadium in solution in the cobalt.

Human and Exner (1994, 1998) systematically studied the effect of several parameters, including grain size, binder content and binder composition, on the corrosion resistance of hardmetals. They found that the grain size had no effect on the potentiodynamic polarization behaviour of WC-Co hardmetals in 1N H_2SO_4 solution, even when the grain size varied between 1 and 5 μm. They further established that for plain WC-Co hardmetals, the corrosion rate increases with increasing Co content.

Human and Exner (1996) have shown that the corrosion behavior of WC-Co follows Stern's linear rule of mixtures (Equation 2.3)

$$i^{WC-Co} = A_A^{WC} \cdot i^{WC} + A_A^{Co} \cdot i^{Co} \qquad 2.3$$

where i^{WC-Co} is the electrochemical current density of the WC-Co alloy, A_A^{WC} is the cross sectional area fraction of the WC phase, i^{WC} is the current density of the WC, A_A^{Co} is the cross sectional area fraction of the binder phase and i^{Co} is the current density of Co(W,C), representative of the binder which is a solid solution of W and C in cobalt.

Human and Exner (1994,1996) also took into account the relative WC and binder areas, mathematically modelled the polarization curves of WC-Co alloys from pure WC and Co(W,C) alloys, and found a small deviation of the individual phases from the behaviour of WC-Co alloys. They compared two model assumptions: in the first model the possible influence of a tungsten depleted region at the phase boundaries was considered by modeling the depleted region as pure cobalt and the remaining binder as a Co(W, C) alloy:

$$i^{WC.\,Co} = A_A{}^{WC}.\, i^{WC} + A_A{}^{Co(W,C)}.\, i^{Co(W,C)} + A_A{}^{Co(0)}.\, i^{Co(0)} \qquad 2.4$$

where $i^{WC.\,Co}$, $i^{Co(W,C)}$, $i^{Co(0)}$ were the current densities of WC-Co composite, Co(W,C) alloy and pure cobalt respectively and $A_A{}^{WC}$, $A_A{}^{Co(W,C)}$, $A_A{}^{Co(0)}$ were the area fractions of the WC phase, inner binder regions respectively.

In the second model, the binder region was considered to behave as a uniform Co(W,C) alloy and the total current density was given as:

$$i^{WC.\,Co} = A_A{}^{WC}.\, i^{WC} + A_A{}^{Co(W,C)}.\, i^{Co(W,C)} \qquad 2.5$$

From the results of the two models, the second model resulted in a more accurate representation of the WC-Co composite and there was no justification for assuming a significant influence of a

tungsten depleted zone (first model). This was further substantiated by the microstructural changes which occurred during potentiostatic tests (Figure 2.3). A WC-Co composite was polarised to potentials between those of pure cobalt and the cobalt alloy. At such potentials pure cobalt should corrode actively while the alloy should remain inert and consequently two such regions can be distinguished in the microstructure, which is the principle of electrochemical etching. The resulted micrographs did not however provide any evidence of a tungsten depleted region at the WC-Co interfaces. Rather, polarisation resulted in fine pitting uniformly across the binder. There was evidence of some exaggerated attack at the WC-Co interfaces but this was irregular and greatest at points of WC-WC contact. This might have been due to higher tensile stresses in such regions of the binder owing to thermal mismatch, as reported by Spiegler *et al*. (1992).

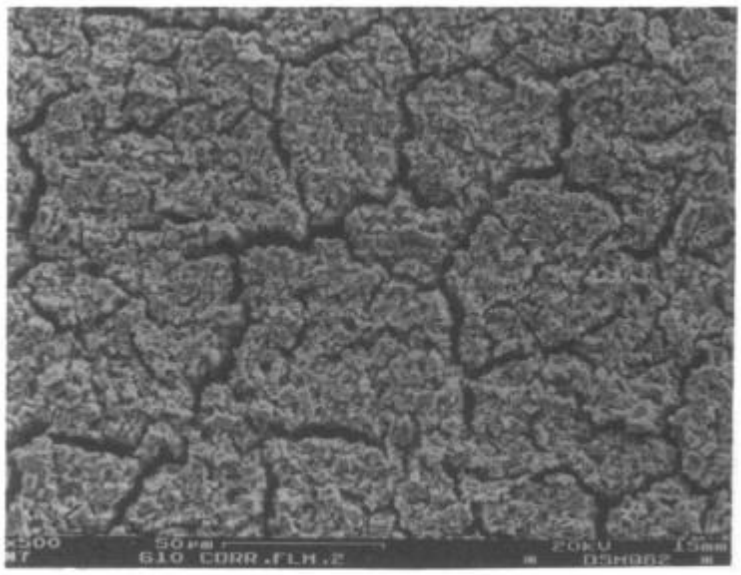


Figure 2.3. SEM image of the layer formed on the surface of the WC-Co composite after a full polarization scan (Human and Exner, 1996).

Mori *et al*. (2003) studied the effect of magnetic saturation of the binder on corrosion behaviour of WC-based hardmetals (Figure 2.4). The Co content was kept constant while varying the carbon content. The carbon content affects the amount of W atoms that go into solution in the Co. Magnetic saturation measures the carbon and tungsten content in the cobalt, and this content affects corrosion, as stated earlier. The magnetic saturation of Co decreases linearly with

increasing content of W (Tillwick and Joffe, 1973). Mori *et al*. (2003) found that as the magnetic saturation of WC-Co hardmetals increased, that is, with decreasing W content in the Co, the corrosion resistance decreased. The effect of the magnetic saturation on the hardmetals with additions of refractory carbides such as VC, TiC, TaC and Cr_3C_2 had not been explained or tested, and is an area that required further research.

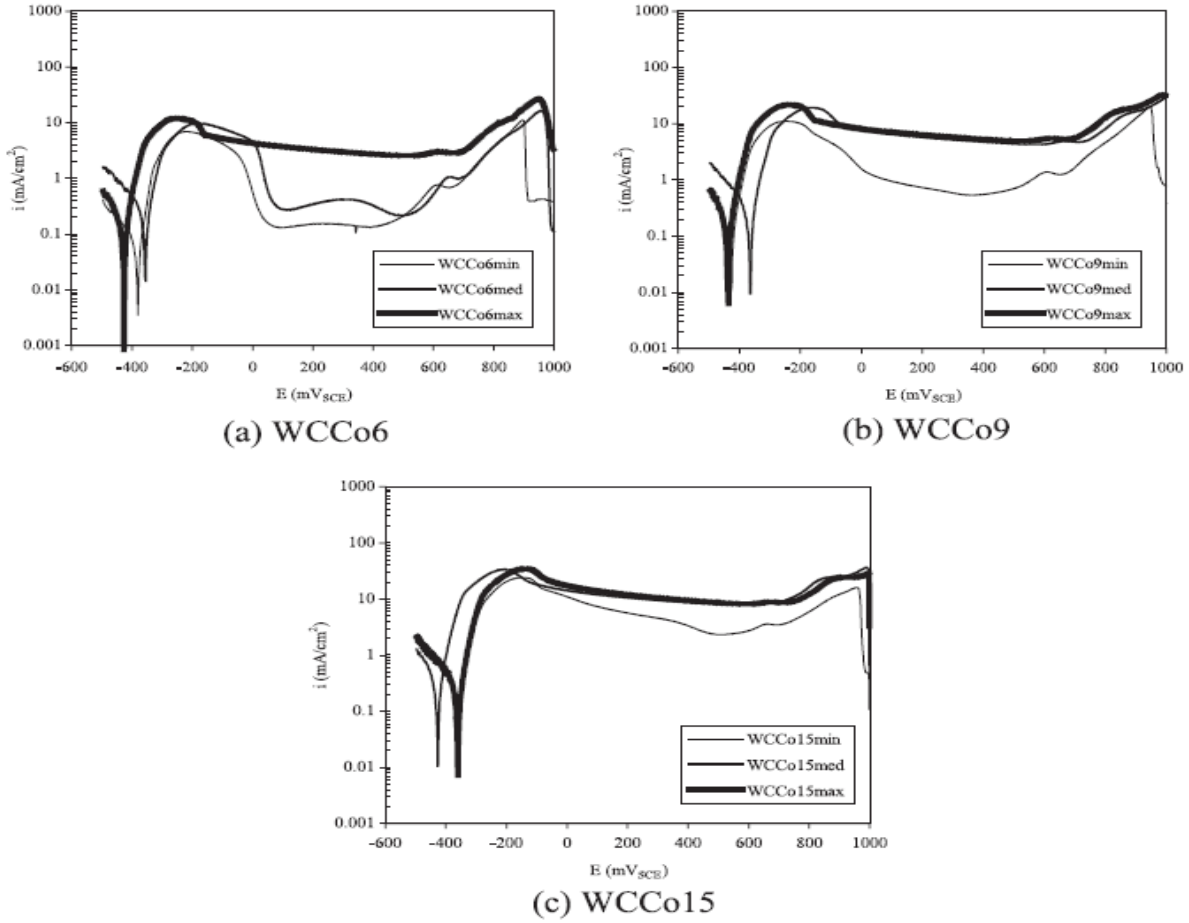


Figure 2.4. Effect of magnetic saturation, 4 r, on electrochemical behavior of cemented carbides with different cobalt binder contents in aerated 1N H_2SO_4, where min, med and max refer to the magnetic saturation (Mori *et al*., 2003).

According to Schuhmacher and Ostermann (1973), the corrosion rate of WC-6wt% Co in a concentrated HCl solution increased with decreasing grain size. This observation was later disproved by Human and Exner (1994, 1998). There appears to be no consensus on corrosion behavior in H_2SO_4 solutions. Tomlison and Linzell (1988) first reported that there was no effect

of WC grain size on the corrosion rate of WC- (6-20) wt% Co in 0.01 M H_2SO_4 and Na_2SO_4 solutions. However, a year later, Tomlinson and Ayerst (1989) reported that an increase in the WC grain size resulted in decreasing corrosion resistance in 0.01 M H_2SO_4 and Na_2SO_4 solutions. Luyckx and Love (2004) undertook a study of WC grades with varying grain sizes, but of equal cobalt content. They made the hypothesis that the corrosion rate should decrease with increasing cobalt mean free path, due to the decreasing total area of the WC-Co interface. However, due to large scatter, it was only possible to conclude that in the 1N H_2SO_4 solution used in the tests, the difference in corrosion between the different grades was small. As already indicated, Human and Exner (1994, 1998), showed that grain size does not affect the corrosion rate in H_2SO_4. In general, it is difficult to compare observations by different researchers because the test specimens are different and the different researchers do not characterize their specimens to the same degree. However, generally, there appears to be agreement that W in Co alters corrosion behavior.

Broccardo (2003) studied the effect of relatively large additions of VC on the corrosion behaviour of WC-Co hardmetals. He found that as the cobalt content increased, the WC-10VC-Co alloy showed increasing resistance to corrosion, and that the corrosion resistance of WC-10VC-Co materials was greater than that of the WC-Co alloys of equivalent Co content, (Figure 2.5). The cause for this difference in corrosion behaviour between WC-Co and WC-VC-Co alloys was not explained, but the finding was in agreement with other workers (Human, 1994), since it is known that vanadium stabilizes the fcc-Co phase. Broccardo (2003) indicated that since cubic Co was more corrosion resistant than hexagonal Co (Human, 1994), the VC increased the corrosion resistance of the Co binder phase by increasing the fcc-to-hcp Co ratio. The same trend of reducing corrosion rate with increasing cobalt contents in the VC grades was observed by Human (1994) and Broccardo *et al*. (2003) (Figure 2.5).

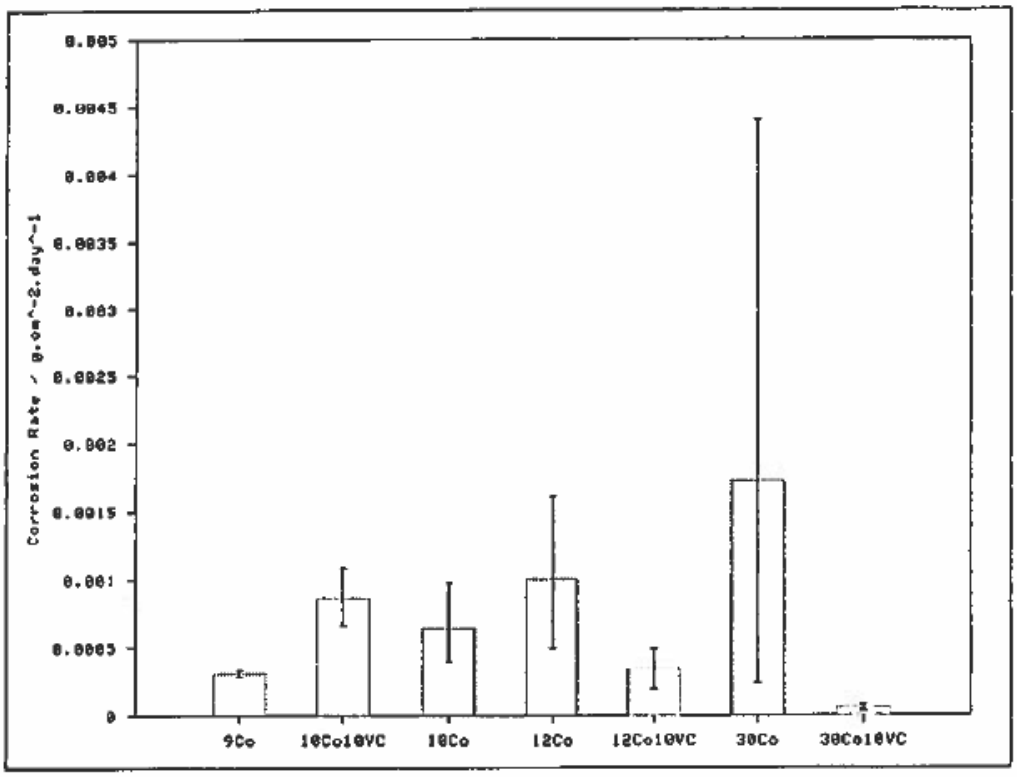


Figure 2.5. Corrosion rate from electrochemical tests determined by Tafel extrapolation (Broccardo *et al*., 2003).

Virtanen *et al.* (2009) investigated the effect of WC grain size on the corrosion behavior of WC-Co hardmetals in alkaline solutions, where passivation of the Co binder was possible, and found that grades with finer grains had improved corrosion resistance. These grades (with fine grains) had increased content of W and C in the Co binder, whose effect had, as already noted, been discussed by Human and Exner (1998). These elements were mostly concentrated in a narrow seam in the binder at the WC/Co interface. The higher the W and C concentration in the cobalt binder, the larger was the content of fcc Co in the binder matrix. The results by Virtanen *et al.* (2009) appeared to indicate that the grain size affected the fcc Co phase by helping stabilize it and therefore helping alter the corrosion behavior as discussed by Broccardo (2003). The role of grain size on corrosion (Virtanen *et al.*, 2009) could be difficult to justify, because the grades used also had grain refiners like Cr_2C_3, which are known to improve corrosion resistance, and it can be argued that the observations could not necessarily be attributed to the effect of grain size alone. The clearest observation from Virtanen's work was the monotonous decrease of corrosion current density with decreasing magnetic saturation, that is, increasing W content in binder.

Work done by Azuma (1995) indicated that the addition of Ca ions in neutral and alkaline solutions reduced the corrosion of hard metals through the precipitation of the $CaWO_4$ on sample surfaces. Similar observations were made by Virtanen *et al.* (2009) at elevated temperatures. Virtanen *et al.* (2009) found that Ca ions in alkaline solutions reduced the anodic currents by up to 5 times, by forming a surface layer on the WC-Co hardmetal surface, which remained stable even at high temperatures.

Konadu *et al.* (2010), following up on the work of Broccardo (2003), determined the effect of increasing VC on the corrosion of WC-Co in 1M H_2SO_4 and 1M HCl acid solutions. Their test samples had 10 wt%Co and VC contents of 0, 0.4, 10 and 27 wt%. In Broccardo's (2003) work, the VC content was fixed at 10 wt%, while the cobalt content was varied. Konadu *et al.* (2010) showed that the corrosion current densities were highest for the 0.4 wt% VC sample, but then decreased with increasing VC content (Table 2.5). Konadu *et al. (*2010) did not determine the ratio of the fcc and hcp Co in their samples. Surface analysis showed that potentiodynamic polarization led to the formation of passive films of hydrated WO_3. No VC-based corrosion product was observed after testing in HCl. However, in H_2SO_4, $VOSO_4.H_2O$ formed in high VC content alloys and appeared to be harmful to the corrosion resistance, since their current densities were higher in 1M H_2SO_4 than in 1M HCl (Table 2.5). The poor corrosion resistance of WC-VC-Co samples observed by Konadu *et al. (*2010) was in line with that of Tomlinson and Ayerst (1989) who noted that the presence of vanadium in WC-Co-Cr interfered with the passivation conferred by small amounts of chromium on the cobalt binder. It therefore appears from literature that the effect of VC on the corrosion resistance of WC-Co is not uniform, and is solution dependent.

Table 2.5. Corrosion parameters of the various WC-VC-Co samples in 1M HCl and 1M H_2SO_4 (Konadu *et al.*, 2010).

Sample	**1M HCl**		**1M H_2SO_4**	
	E_{corr} (V) (SSE)	i_{corr} (μA cm^{-2})	E_{corr} (V) (SSE)	i_{corr} (μA cm^{-2})
WC-10Co	-0.189	1.1	-0.235	5.6
WC-0.4VC-10Co	-0.317	11	-0.271	9.3
WC-10VC-12Co	-0.915	1.0	-0.274	4.5
WC-27VC-11Co	-0.213	0.3	-0.263	2.8

Concurrent work by Potgieter *et al.* (2011) varied the amount of ruthenium in plain WC-10Co and WC-10Co containing 0.4 wt% VC. As the ruthenium content was increased, the corrosion resistance of WC-10Co increased proportionally, although the 0.4 wt% VC sample showed slower open circuit at varying voltage compared to the WC-10Co alloy. Figure 2.6 shows that all polarization curves in 1M H_2SO_4 underwent same typical active-passive transition behavior at varying voltages. In Human, Exner and Roebuck's (1996, 1998) work, which did not use modified specimens, the specimens did not exhibit the same behavior in the same solution, but exhibited direct passivation. Ruthenium, in small additions, was used in stainless steel for corrosion improvements by Potgieter *et al.* (1993). Broccardo (2003) reported no corrosion improvements at low cobalt content (10 wt% Co) with or without VC addition, although VC addition lowered the corrosion rate at high cobalt contents. However, Potgieter *et al.* (2011) reported the difference was observed at the same cobalt content with addition of small amounts of ruthenium (0.4 wt% to 2 wt%). The corrosion rate showed a decrease as ruthenium increased, although at 1.0 wt% and 1.5 wt% Ru, the corrosion rates were similar. The corrosion rate decreased with Ru addition of up to 2 wt%, but a further Ru increase from 2 wt% to 3 wt% did not show any corrosion improvement (Figure 2.6).

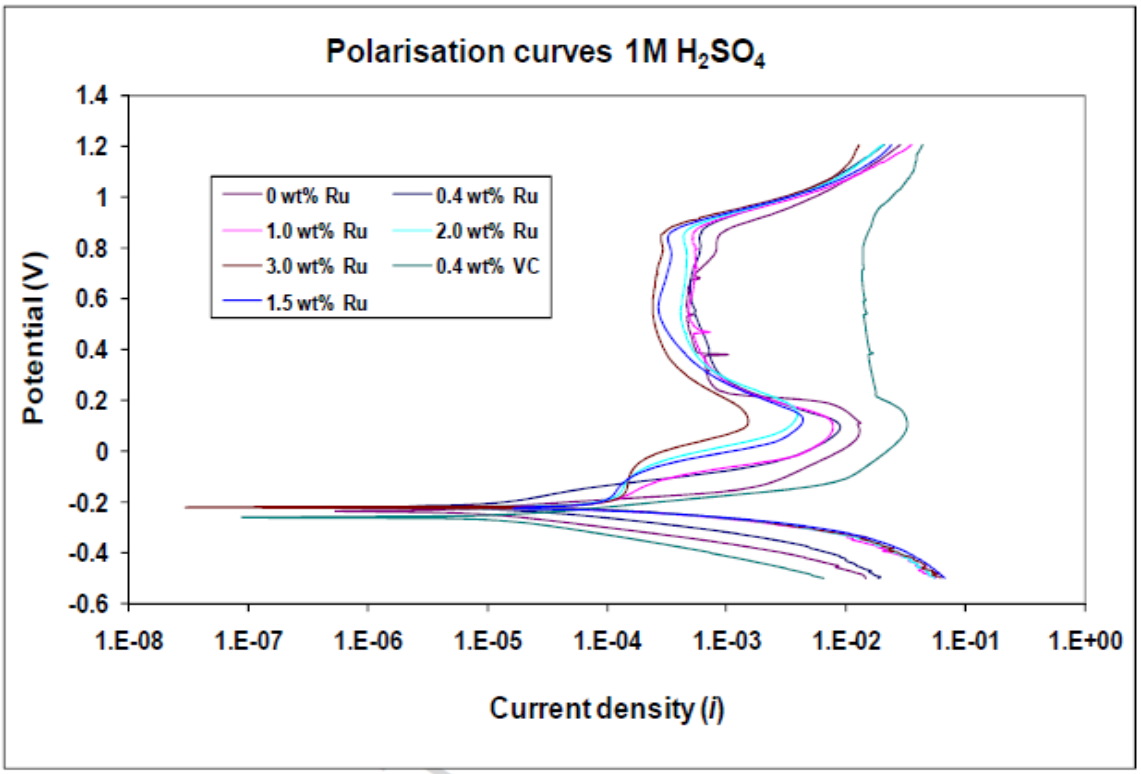


Figure 2.6. Potentiodynamic scans of WC-10Co alloys in 1M H_2SO_4 with increasing Ru additions and 0.4VC (Potgieter *et al.*, 2011).

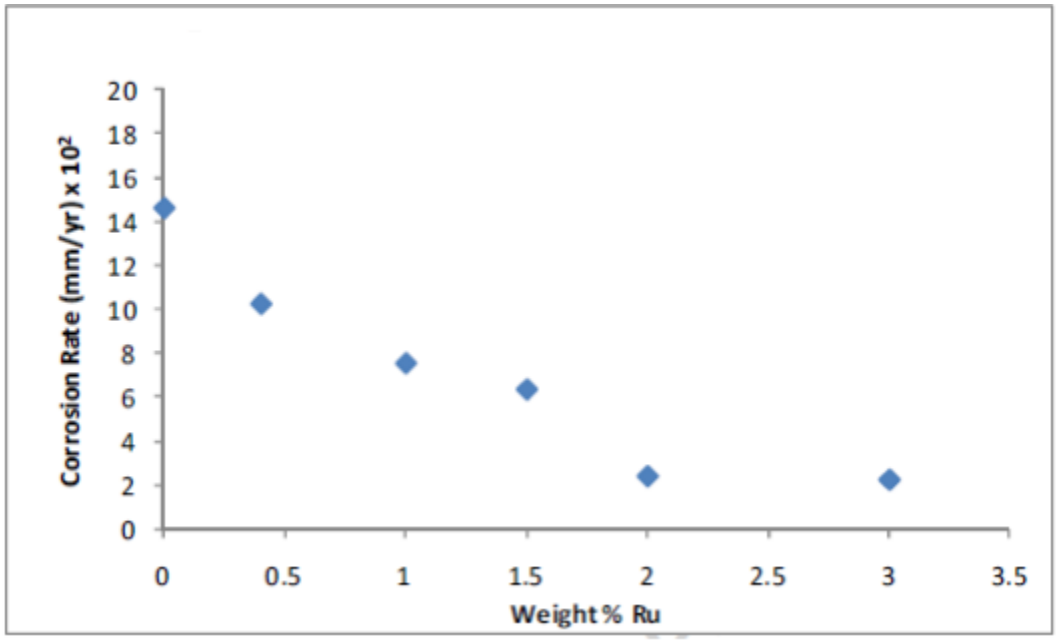


Figure 2.7. Effect of increasing ruthenium on corrosion rate of WC-10Co alloys in 1M H_2SO_4 (Potgieter *et al.*, 2011).

2.6. Corrosion of VC

This Section has been included in this literature review because VC is in the materials being investigated. A thorough literature search did not yield any results for the corrosion of cemented VC-based hardmetals. However, there are a few articles on the corrosion of VC coatings.

Bhagga Fazluddin *et al*. (1995) evaluated the corrosion behavior of vanadium carbide coatings applied by thermal diffusion (TD) on carbon steel and mild steel using accelerated electrochemical tests and found that the corrosion resistance of vanadium carbide coating was superior to that of the untreated base alloys. The corrosion behavior of carbide coated substrates was influenced by both the substrate and the coating thickness. This is because VC coatings prepared by thermal diffusion are inherently defective, either cracked and or porous (Kong, Zhou, Long, Wu (2012)), and therefore allow contact between the electrolyte and the substrate. The defective nature of the coatings can for example explain a decrease in the pitting resistance and passive ranges of VC coated stainless steel observed by (Bhagga Fazluddin *et al*., 1995). Higher coating thickness improves corrosion resistance because the corrosive medium diffuses at a slower rate through the micropores in the thicker coatings (Bhagga Fazluddin *et al*., 1995).

Aguzzoli *et al.* (2012) has recently investigated, among others, the corrosion properties of VC thin film coatings in 3.5% NaCl solutions. The coatings bore different C/V ratios and were deposited on AISI H12 steel by DC reactive sputtering at different substrate temperatures. Better corrosion resistance was obtained for higher density films deposited at higher temperatures, again, indicating the importance of defects on the corrosion resistance of VC coatings. Cyclic polarization curves (Figure 2.8) indicated the occurrence of repassivation in the test solution, but the areas of the cyclic curves (loops) were high, implying high susceptibility to pitting corrosion. It is telling that the cyclic curves of the untreated alloy resemble those of the treated alloys, making it possible that the repassivation indicated for the treated alloys was due to the substrate because the corroded surfaces were significantly pitted through (Figure 2.9).

The VC diffusion coatings on carbide steel showed strong passivation behaviour with agreement to Aguzzoli *et al.* (2012). Konadu *et al.* (2010) has reported that the introduction of VC in WC-Co improved the passivation resistance of the hardmetals only in 1M HCl, and at high VC

contents resulted in lower corrosion current densities than for the base alloy in both 1M H_2SO_4 and 1M HCl. Increasing VC content makes the open circuit potential (OCP) more negative than the base alloy in both acidic solutions (1M H_2SO_4 and 1M HCl). Specimens exhibited pseudo passivation in all the acidic media due to the formation of passive films of hydrated WO_3. Tomlinson and Ayerst (1989) also showed the same lack of effect, as the presence of vanadium interfered with the passivation conferred by small amounts of chromium on the cobalt binder. From the literature the effect does not seem to be uniform.

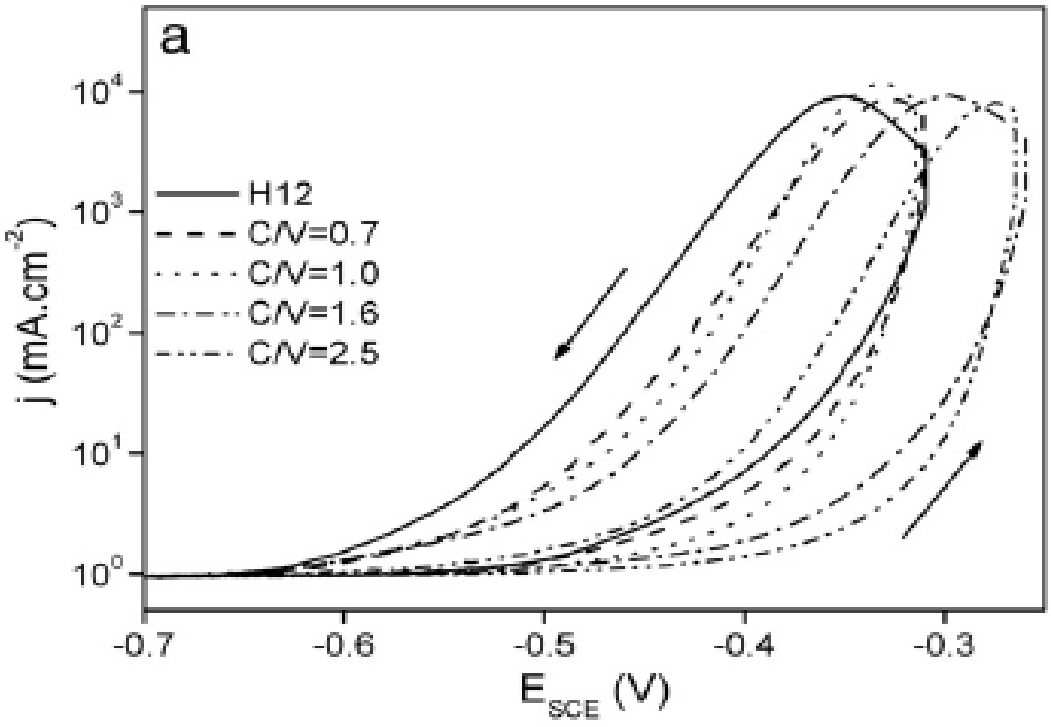


Figure 2.8. Cyclic polarization curves, showing the pitting loop for AISI H12 tool steel samples coated with VC films at 20 °C with different C/V ratios in 3.5% NaCl solution.

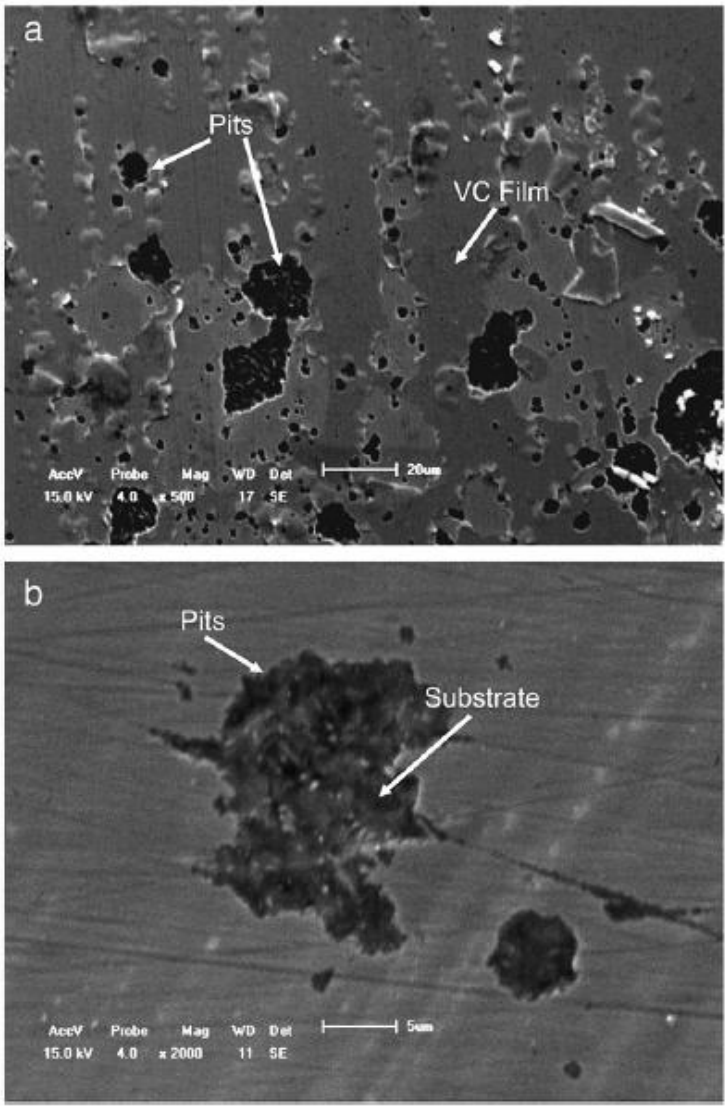


Figure 2.9. SEM microstructures of a AISI H12 tool steel sample coated with a 200 nm thick VC film, after corrosion in 3.5% NaCl solution. The images show the pits (a) and the details of one pit with the exposed substrate in the bottom (b).

Chapter 3

Experimental Procedure

Details of the test specimens, sample preparation procedures and experimental techniques used in this investigation are described in this chapter. The compositions of the materials used in this investigation are given in Table 3.1. Before commencing the testing, the original state of the specimens was determined by scanning electron microscopy (SEM) and energy dispersive X-ray analysis (EDX). As noted earlier, this work was a continuation of the work done by Broccardo (2003), and most of the specimens were a carry-over from that earlier work.

3.1. Sample selection and preparation

Table 3.1. Starting powder composition for each sample. * Immersion corrosion

Samples	**State of sample when examined**	**Composition (wt%)**		
		WC	**Co**	**VC**
WC-9Co	*corroded	91	9	0
WC-10Co	Not corroded and *corroded	90	10	0
WC-12Co	* corroded	88	12	0
WC-30Co	Not corroded and *corroded	70	30	0
WC-10VC-10Co	* corroded	80	10	10
WC-10VC-12Co	*corroded	78	12	10
WC-10VC-15Co	* corroded	75	15	10
WC-10VC-30Co	Not corroded and *corroded	60	30	10
WC-67VC-10Co	Not corroded	23	10	67

Samples of the nominally WC-30Co, WC-10VC-30Co, WC-10Co and WC-67VC-10Co alloys were characterised using X-ray diffraction (XRD), image analysis, transmission electron

microscopy (TEM), hardness measurements, density measurements and observing the corrosion behaviour.

For SEM studies, samples were mounted in a thermosetting resin and polished. The following polishing method was used:

1. Coarse plate of magnetic disc (MD) - Allegro with 80 µm grit to achieve a top flat polished surface that was parallel to the bottom surface.
2. Fine plate of magnetic disc (MD - Allegro with 1200 µm grit was used to achieve a finer polished top surface.
3. Top surface polished with a pan cloth with 3 µm followed by a 1µm diamond spray.

TEM samples were prepared by using a diamond saw to section the alloys into approximately 400 µm thick slices. The slices were then hand-ground on a 15 µm diamond pad to a thickness of about 80 µm. From the thin slices, 3 mm diameter discs were drilled using a Gatan Ultrasonic Disc Cutter. The discs were subsequently argon ion thinned to perforation in a Gatan PIPS ion mill, operating initially at 5 keV at 6^o, ending at 2 keV at 3^o to minimize ion damage.

The corrosion behavior of the specimens was determined as described in Section 3.10. Optical microscopy was used on the cross-sections of the immersion corroded alloys in order to measure the depth of the corroded layer. Magnetic saturation measurements of the WC-10Co and WC-67VC-10Co alloys were carried out in order to determine the amount of tungsten dissolved in the cobalt binder, and to see if this affected the corrosion resistance of the samples. The techniques used are described in detail in the following sections. However, because of the necessity to re-polish specimens after use (Broccardo, 2003), some specimens were reduced to fragments before they could be subjected to all the experiments.

3.2. X-ray diffraction

X-ray diffraction was conducted on uncorroded samples of WC-30Co, WC-10VC-30Co, WC-10Co and WC-67VC-10Co alloys using a Philips PW1710 powder diffractometer operating at 40 kV, utilizing a CuK_α radiation source. The measurements were performed over the diffraction angle range $2\theta = 20^o$ to 100^o using a step size of 0.02^o. The time per step was 20 seconds.

In order to determine the ratio of the amount of fcc to hcp structure in the Co phase, the Rietveld refinement method was used to deconvolute the overlapping peaks of the two structures. Qualitative analysis was performed using information from the Joint Committee on Powder Diffraction Standards (JCPDS) database and quantitative analysis using the Rietveld - Analyse (Program Autoquan, Seifert FPM). The R_{wp} values were all in the range of 6 to 9 %. This is the quality measure of the fit and is explained by Equation 3.1:

$$R_{wp} = \left[\frac{\sum_i w_i \left(y_i - y_{ic} \right)^2}{\sum_i w_i y_i^2} \right]^{\frac{1}{2}} \qquad (3.1)$$

where:

$y_{i\,=}$ intensity at a given angle

$y_{i\,c}$= calculated intensity

$w_{i\,=}$ weight of the value

The measurement conditions are summarised as follows:

Equipment: RD7, CuK_{α}- radiation using a carbon monochromator.

Diffraction angle measurement range: $10 – 90^{o}$

Time per point: 10 seconds

Step size: $0.02 - 0.04^{o}$.

It was not possible to carry out the measurements with a molybdenum anode tube, although it would have been preferable, on account of the high adsorption coefficient of Co for the CuK_{α} radiation.

3.3. Scanning electron microscopy

Scanning electron microscopy (SEM) in both secondary and backscattered (atomic number contrast) modes was undertaken on polished samples in order to determine the microstructures of the alloys, while EDX was used to determine the compositions of the phases with the aid of pure element standards of W, V and Co. The results given were derived from at least five 100s

analyses taken at different locations. Two different SEMs were used: a JEOL JSM-840 equipped with a LINK AN10000 beryllium windowed detector (which could not detect elements below sodium, Z = 11), and a LEO 1525 field emission SEM with an Oxford Instruments ultra-thin windowed EDX detector. Both microscopes were operated at 20 keV.

3.4. Image analysis

Cross-sections of eight corroded WC-Co and WC-10VC-Co alloys were studied by optical microscopy in order to measure the depth of the corroded layers. Only one sample of each composition was available from immersion testing. ImageTool is an interactive image viewer and analysis program for Microsoft Windows 95 or Windows NT. In addition, it is possible, through this software, to measure the average grain size and areas using lineal analysis.

3.5. Transmission electron microscopy

A Philips CM200 TEM operating at 197 kV and equipped with an ultra-thin windowed Oxford Instruments ISIS EDX and a Gatan Imaging Filter (GIF) was employed to study the microstructure and determine the chemical composition of the phases.

3.5.1. Lattice parameter determination using the TEM

Calculations of the lattice parameter of the Co and WC phases in the WC-10VC-30Co alloy were carried out on TEM diffraction patterns using a travelling microscope with a measurement accuracy of 0.01 mm. Firstly, the ring diameter for the (600) ring was measured in two perpendicular directions from an Al (fcc) polycrystalline diffraction pattern, Figure 3.1. This pattern was obtained under the same lens conditions and at the same sample height position as for the area in the alloy from which its diffraction patterns were obtained. The Al diffraction pattern was utilized to calibrate the camera length, *L*, the distance from the specimen to the photographic film. Essentially, this can be considered to be a magnification factor. *L* is given by the formula:

$$L = \frac{ra}{\lambda\sqrt{h^2 + k^2 + l^2}} \qquad (3.2)$$

where:

L is the camera length,

r is the radius of the diffraction pattern ring used,

hkl are the Miller indices of the planes contributing to the spots in the diffraction ring utilised, and λ is the electron wavelength which equals 0.025912 Å at 197 keV.

For aluminium, a = 4.0496 Å (Edington, 1976).

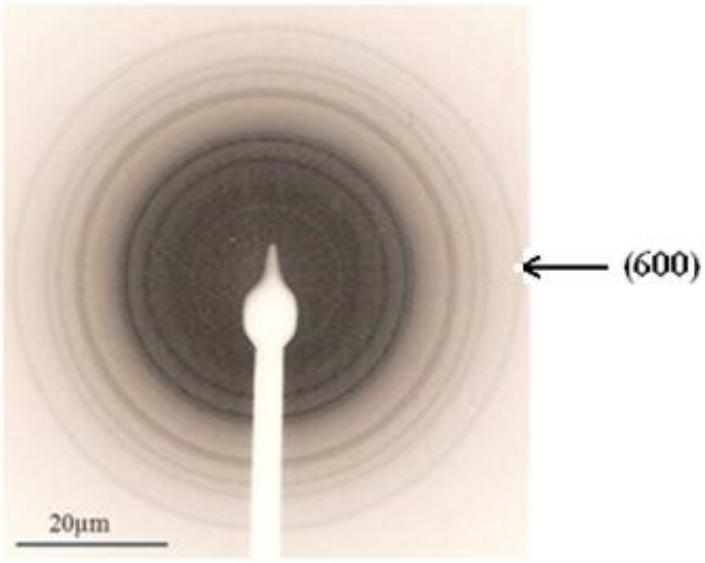


Figure 3.1. Electron diffraction pattern from an aluminium thin film showing the (600) ring, the outer of the doublet, used as a standard to calculate the camera constant, λ*L*.

Secondly, the distances from the centre (000) spot to the neighbouring *hkl* diffraction spots, as well as the angles between the spots (planes), were measured from the diffraction patterns of WC and Co. Examples of the diffraction patterns are given Figures 3.2-3.4. These measurements enabled a consistent indexing of the diffraction spots and from Equation 3.2, and knowing the structure type of the phase, the lattice parameter could be determined. The zone axis or crystal direction [*xyz*] of any given diffraction pattern was determined using Equation 3.3 where $h_1k_1l_1$ and $h_2k_2l_2$ are the Miller indices of two spots in the zone axis diffraction pattern.

$$\begin{aligned}(xyz) &= \left(\begin{vmatrix} k_1 & l_1 \\ k_2 & l_2 \end{vmatrix}, \begin{vmatrix} l_1 & h_1 \\ l_2 & h_2 \end{vmatrix}, \begin{vmatrix} h_1 & k_1 \\ h_2 & k_2 \end{vmatrix}\right) \\ &= (k_1l_2 - l_1k_2,\ l_1h_2 - h_1l_2,\ h_1k_2 - k_1h_2)\end{aligned} \qquad (3.3)$$

(*xyz*) being the reciprocal lattice plane in which the two diffraction spots lie.



Figure 3.2. $[01\bar{1}0]$ zone axis pattern from a WC grain in the WC-10VC-30Co alloy.

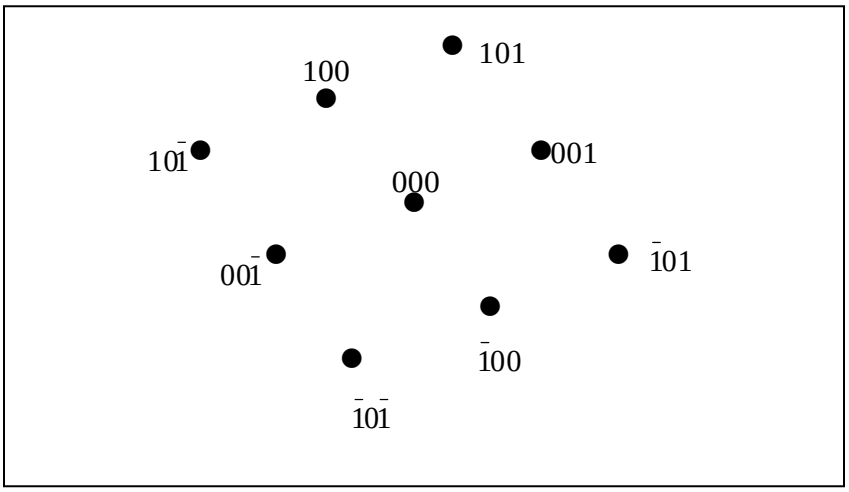


Figure 3.3. Identification of the WC spots in Figure 3.2.

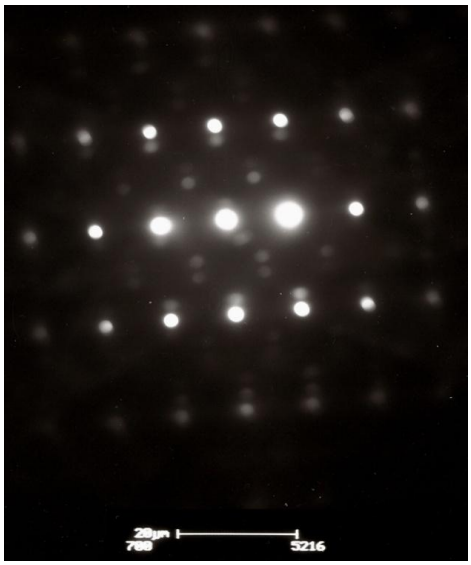


Figure 3.4. [12] pattern of an fcc Co grain in the WC-10VC-30Co alloy, with faint spots derived from the stacking faults which are hcp Co.

3.5.2 EDX analysis in the TEM

The analysis conditions were typically 100-200 s real time, best resolution, 10 nm spot size in TEM mode operation. The influence of the Trigger Noise Peak (inserted in the Oxford EDX system to calibrate the zero energy position) on the carbon peak was removed using the spectrum from a freshly ion milled nickel thin foil that had been plasma cleaned for ten minutes.

EDX analysis in the TEM was a problem due to carbon contamination. The focused electron probe generates an electric field which acts to attract free carbon on the sample surface to the probe position (Fourie, 1987). In addition, the electron beam disassociates the hydrocarbons which are in the microscope vacuum in the path of the electron beam and the resulting carbon atoms deposit on the analysed area. The result is the generation of an ever increasing sized cone of carbon sited on the incident and exit regions of the area of the sample being analysed. With time, this effectively increases sample thickness and the X-ray Bremsstrahlung. In addition, the incident electron beam is gradually deflected off the cone to neighbouring regions such that the X-rays no longer come from the region of interest. The subsequent compositional analysis can indicate a large high carbon content, typically 90 % greater.

Two possible solutions were explored, being plasma cleaning and a low temperature holder.

3.5.2.1 Plasma cleaner

The sample mounted in the TEM sample holder was inserted into a Fischione Model 1020 Plasma Cleaner prior to insertion in the microscope. The part of the holder that would be in the microscope column was cleaned with 25% oxygen, 75% argon plasma. This is a low voltage plasma that removes only the surface contamination on the sample and sample holder. The plasma cleaning efficiency was calibrated using a carbon film on a copper mesh TEM grid. The film was plasma cleaned for one minute, then examined in the TEM. This was continued for one minute plasma cleaning intervals, until the carbon film was completely removed. From this, and from subsequent cleaning experiments, and EDX analyses of hardmetal samples, it was determined that a 20 minute plasma clean was sufficient to remove the carbon from the sample and to prevent the accumulation of carbon contamination spots by the end of typically a 100-200 s EDX analysis. Prior to the insertion of the sample in the sample holder, the latter was plasma cleaned for one hour.

3.5.2.2 Low temperature, double tilt TEM holder

A Gatan low temperature, double tilt, analysis holder was used, hoping that working at around-180^{o}C temperatures would help fix any carbon contamination in place on the sample surface since the mobility of carbon would be reduced.

3.6. Density measurements

The density of the WC-10Co, WC-67VC-10Co, WC-30Co and WC-10VC-30Co samples was measured using the Archimedes' principle. The dry mass of the samples was measured in air, after which the samples were submerged in water, suspended by a wire. The level of water was then topped up to cover the sample in a glass beaker. The density was calculated using Equation 3.4.

$$\rho = \rho(H_2O)\frac{m_{air}}{m_{air} - m_{water}} \qquad (3.4)$$

where:

$\rho(H_2O)$ is the density of water at room temperature,

m_{water} is the mass of sample in water, and

m_{air} is the mass of sample in air (dry).

3.7. Hardness measurements

Vickers hardness measurements were made on a Leco V100 - A2 Hardness Tester, using loads of 30 kg and 300 g. Ten measurements were made on representative multiphase regions of each sample of WC-10Co, WC-30Co and WC-10VC-30Co alloys using a 30 kg load, while a load of 300 g was applied to the mixed carbide phase in the WC-67VC-10Co alloy, since the sample was brittle and cracked at higher loads. Prior to the hardness measurements, the samples were polished, and cleaned with alcohol.

3.8. Magnetic saturation measurements

A magnetic balance was used to measure the magnetic saturation of the samples of WC-10Co and WC-67VC-10Co alloys. In this procedure, a magnetic field was applied to the sample until the magnetization of the sample reached its maximum value, the magnetic saturation. Before use, the balance was calibrated using a standard sample (STB) containing a known amount of tungsten carbide and cobalt, from which the calibration constant, κ, could be determined. The magnetic field required to maintain the sample in equilibrium with its weight was measured. The magnetic saturation, $4\pi\sigma$, was then calculated using the formula:

$$4\pi\sigma = \frac{\kappa \times D.R}{w} \qquad (3.5)$$

where:

κ = calibration constant from the STB calibration,

w = mass of the specimen in grams, and

$D.R$ = the magnetic pull in divisions of the digital readout.

This technique can be used to determine the amount of tungsten in solution in the binder phase of hardmetals. For a given cobalt content (Tillwick and Joffe, 1988), the magnetic saturation

decreases with increasing tungsten in solution. The atomic percentage of tungsten in solution is given by:

$$\text{at.\% W} = \frac{4\pi\sigma - 4\pi\sigma_{Co}}{8} \qquad (3.6)$$

where:

$4\pi\sigma$ is the measured magnetic saturation, and

$4\pi\sigma_{Co}$ is the magnetic saturation of pure cobalt which equals $2020\,\text{gauss.cm}^3\text{.g}^{-1}$.

3.9. Corrosion tests

3.9.1. Electrochemical tests

Electrochemical polarisation tests were performed in 1N sulfuric acid on two samples of each of the WC-10Co and WC-67VC-10Co alloys. The specimens with 30 wt% Co were not corrosion tested because they had been reduced to small pieces by repeated polishing, and so could not be analysed. All the experiments were carried out at room temperature. The potentiostat was a Schlumberger Model 1286 electrochemical interface connected to a computer for control and data-logging. A silver/silver chloride (Ag/AgCl) reference electrode was connected to the cell and a platinum wire was used as the counter electrode. A Luggin probe with a salt bridge was used to protect the reference electrode and minimize solution resistance. The 1.2 litre volume corrosion cell was rectangular in shape, and provided side access to the sample. The corrosion cell was enclosed in a Faraday cage in order to minimize electrical noise from the environment. The experimental setup is shown in Figure 3.5.

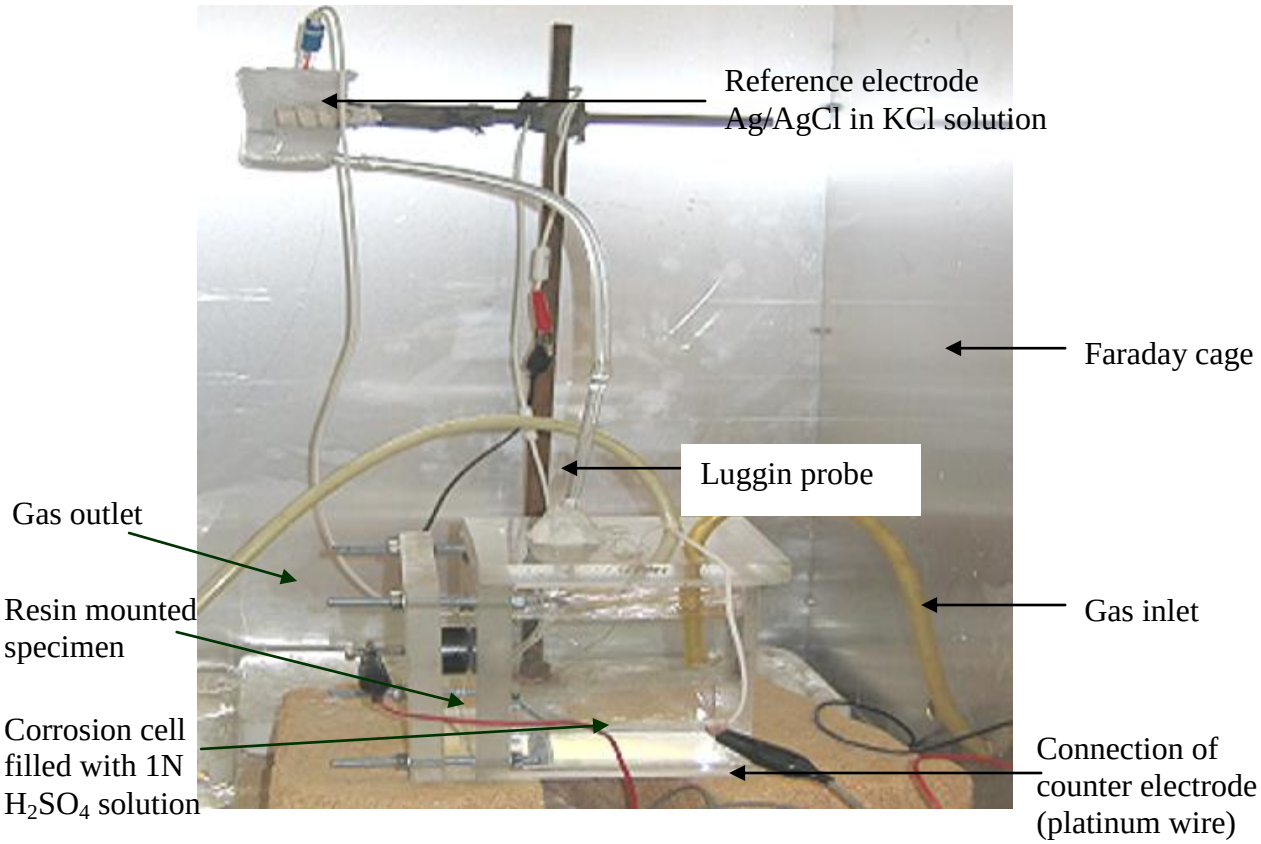


Figure 3.5. Corrosion cell used for the experiments.

The electrolyte was de-aerated with ultra-high purity (99.999%) nitrogen, and fresh solution was used for each experiment. The exposed surface area of the sample was 28.27 mm^2. The sample was polished with 1µm diamond spray, immersed in the electrolyte and allowed to stabilise for 45 minutes at the free corroding potential prior to testing. The potentiodynamic scans were carried out at a scan rate of 1 mV per second, from -700 mV to a potential of +1500 mV relative to the Ag/AgCl reference electrode.

De-aeration was continued throughout the entire course of each experimental run. After every experiment, the samples were observed under an optical microscope and image analysis utilized to determine the penetration depth of the corroded layer. Before the next corrosion test, in order to remove any corrosion product and all of the corroded layer, samples were re-ground using a 80 grit grinding plate, then a finer 1200 grit plate, followed by polishing with 3 and 1 µm diamond sprays.

3.9.2. Immersion tests (Broccardo, 2003)

Immersion corrosion tests were performed in 1N sulfuric acid electrolyte for all samples in Table 3.1, except the WC-67VC-10Co alloy. The temperature was maintained at 50^{o}C in a water bath. No de-aeration or agitation was performed. An Ahllin condenser was used to prevent evaporation of the electrolyte. The samples were exposed to this environment for 48 hours. The mass of the sample after testing (and cleaning of the sample) was compared with the mass before the immersion testing. The mass loss and the samples' surface area before the test (measuring using vernier calipers) were used to calculate the corrosion rate.

Chapter 4

Results

The results of the experimental work are presented in this chapter: first, the results from the characterization of the materials, including the results from corrosion tests, which are particularly important to this project.

4.1. Scanning electron microscopy (SEM)

Scanning electron microscopy (SEM) and energy dispersive X-ray analysis (EDX) were used in order to analyze the microstructure and determine the quantitative composition of the materials.

4.1.1. Microstructural analysis

Figures 4.1 to 4.4 show the microstructures of the four different alloys, acquired in a scanning electron microscope using the backscattered electron mode (BSE). In the BSE micrographs, the light areas represent higher atomic number regions and the darker areas represent lower atomic number regions. The phases in the alloys are summarized in Table 4.1.

.

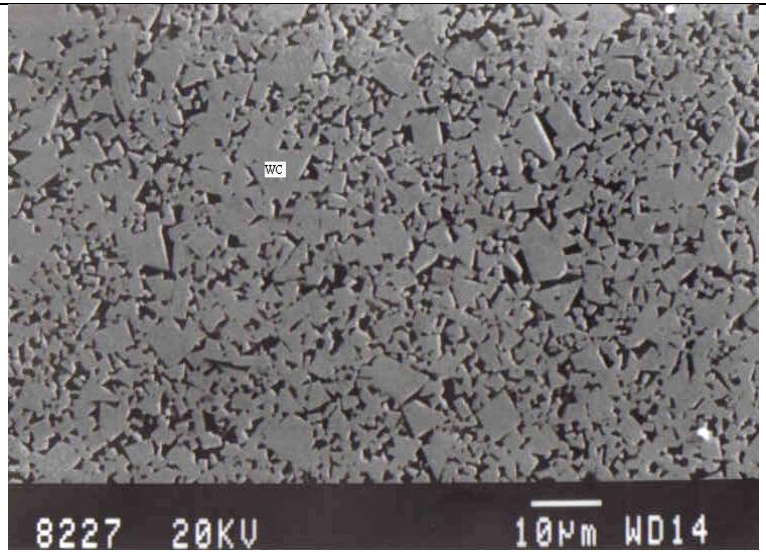


Figure 4.1. SEM image in backscattered electron mode of the WC-10Co alloy, showing WC (light) and Co (dark).

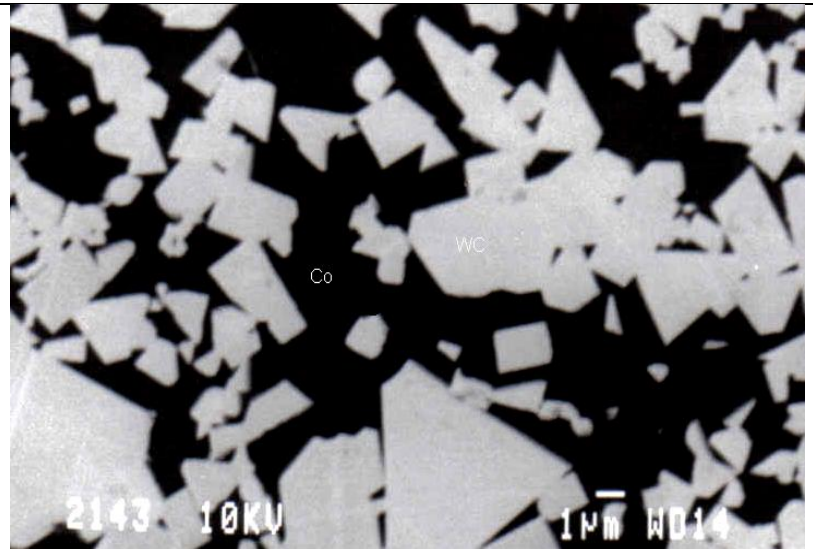


Figure 4.2. SEM image in backscattered electron mode of the WC-30Co alloy showing WC (light) and Co (dark).

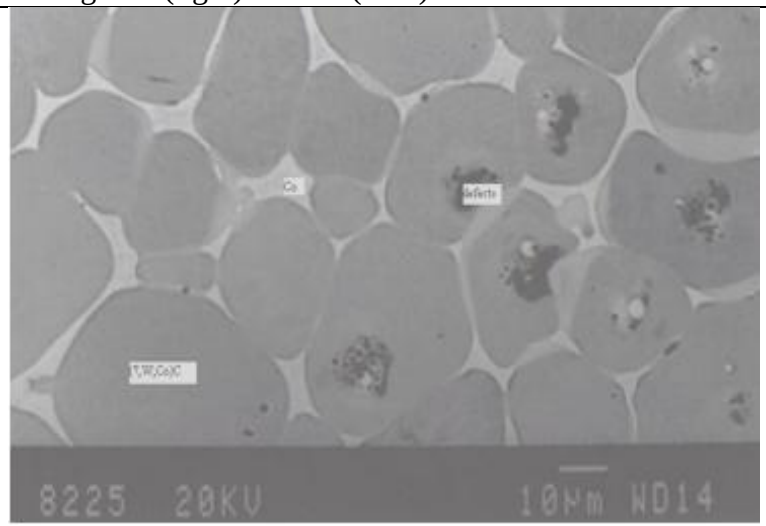


Figure 4.3. SEM image in backscattered electron mode of the WC-67VC-10Co alloy, showing Co (light), (V,W,Co)C(medium) and pores(dark).

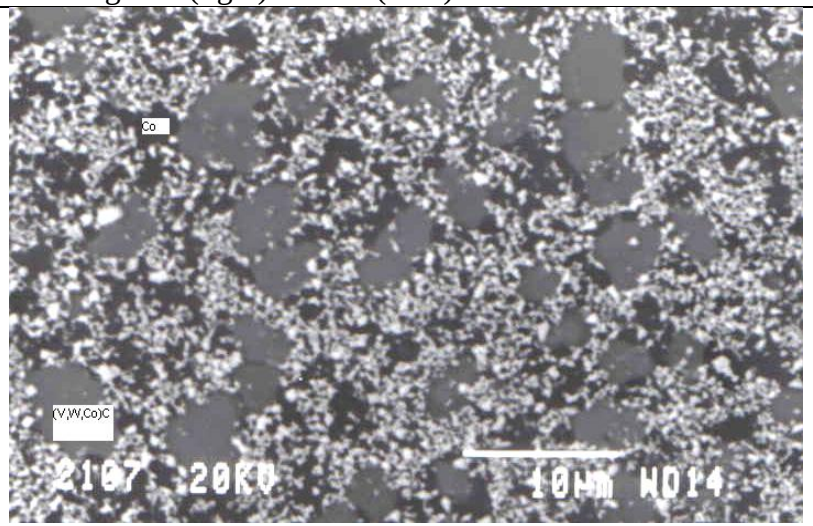


Figure 4.4. SEM image in backscattered electron mode of the WC-10VC-30Co alloy, showing WC (light), (V,W,Co)C (medium) and Co (dark).

Table 4.1. Phases present in alloys determined using backscattered SEM images and EDX.

Alloys	**Phases**
WC-10Co	WC, Co
WC-30Co	WC, Co
WC-67VC-10Co	(V,W,Co)C, Co
WC-10VC-30Co	(V,W,Co)C, WC, Co

The WC-10Co and WC-30Co alloys showed the same phases and the same particle size variation (Figures 4.1 and 4.2). In the WC-67VC-10Co alloy, only two phases were present, Figure 4.3, since all the WC was in solution, either in the VC or in the cobalt. The microstructure showed pores in the mixed carbide grains.

In the WC-10VC-30Co alloy, the tungsten carbide grains were small, typically 0.1-1 μm in size, and much smaller than the mixed carbide phase, Figure 4.4. The cobalt regions between carbide grains were inhomogeneous and could be fairly wide, up to 2 μm in width, while the (V,W,Co) C grains were fairly uniformly distributed and up to 5 μm in size.

4.2. Density measurements

The densities of the test specimens are given in Table 4.2. The measured density from Archimedes principle compared favourably with the calculated (theoretical) density, to within ±2%. Assuming the calculated density does not take porosity into account (perfect structure), and the measured density does, it can be deduced that the porosity levels in the test specimens was around 2%. However, the porosity was not measured. As expected, the density of the materials containing vanadium carbide was lower than that of conventional WC-Co alloys, since VC is less dense than WC. The density of the (V,W,Co)C phase was calculated using the measured density of the WC-67VC-10Co alloy and the density of cobalt (8.87 $g.cm^{-3}$), by applying the following formula:

$$V_{WC\text{-}VC\text{-}Co} = V_{Co} + V_{(V,W,Co)C} \qquad (4.1)$$

where:

$$Volume = \frac{mass}{density}$$

Working from a mass of 100g, the WC-67VC-10Co alloy contained 10g of Co and 90g of (V,W,Co)C. However, this calculated density of (V,W,Co)C is only applicable to the (V,W,Co)C phase. The density of (V,W,Co)C phase was assumed to be that of pure VC, since in this case, (V,W,Co)C has low amount of WC, and the XRD results showed the d-spacings of (V,W,Co)C to be very close to pure VC (Appendix A). The composition could be different in other alloys. The calculated density of each alloy was determined using the following formula:

$$\frac{100}{\rho_{\text{th}}} = \sum \frac{\text{wt}_{\text{i}}\%}{\rho_{\text{i}}} \qquad (4.2)$$

where ρ_i is the density of a phase in the material, and ρ_{th} is the theoretical density (Whitefield, 2011). For WC-10VC-30Co, the density for (V,W,Co)C was also assumed to be that of VC, in order to make the calculations easier.

Table 4.2. Comparison of densities.

Specimen	**Measured density (g.cm^{-3}) using Archimedes' principle**	**Calculated density (g.cm^{-3})**
WC-30Co	12.6 ± 0.09	12.8
WC-10VC-30Co	11.0 ± 0.13	11.2
WC-10Co	14.3 ± 0.09	14.6
WC-67VC-10Co	6.81 ± 0.09	6.97
(V,W,Co)C phase in WC-67VC-10Co	___	6.64

4.3. Hardness measurements

The hardness decreased with higher Co content, and increased with higher VC content (Table 4.3). The hardness of WC-67VC-10Co could not be measured with the same load as used for the WC-10Co alloy (i.e. 30 kg load, as per standard for cemented carbides (http://testequipment, 2004)), since the indenter induced cracks in the sample, making it difficult and meaningless to measure the diagonal of the indentations, as shown in Figures 4.5 (for a cracked sample) and 4.6 (for an uncracked sample). The cracking indicated that the resistance of the material to fracture under this load was poor. Research has indicated that the grain size of the (V,W,Co)C grains must be less or equal to 2 µm, otherwise WC-VC-Co alloys become very brittle (Makhele, 2000). The hardness of WC-67VC-10Co was therefore captured as the microhardness of the mixed carbide grains, which were up to 80 µm across, and thus large enough to measure their microhardness. Figure 4.5 shows transgranular cracks starting from the indentation, indicating that (V,W,Co)C has low resistance to fracture. In contrast, the WC-10Co alloy (Figure 4.6) showed no cracks at its indentations, that is, it had good toughness. No cracks were induced in (V,W,Co)C grains at a load of 300g.

Table 4.3. Hardness values of the alloys using a 30kg load, and a microhardness value using a 300g load.

Specimen	**Hardness (HV_{30})**
WC-10Co	1311± 6
WC-30Co	746 ± 2
WC-10VC-30Co	1020 ± 14
	Microhardness ($HV_{0.3}$)
(V,W,Co)C in WC-67VC-10Co	2073 ± 40

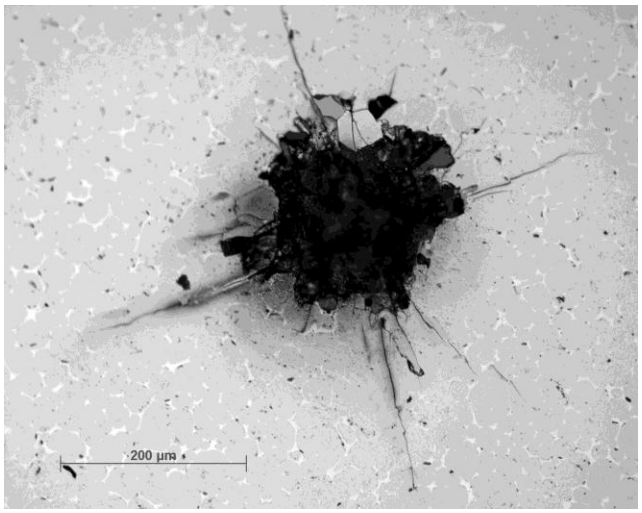


Figure 4.5. Optical micrograph of the WC-67VC-10Co alloy showing cracks radiating from an indentation produced at a load of 30kg.

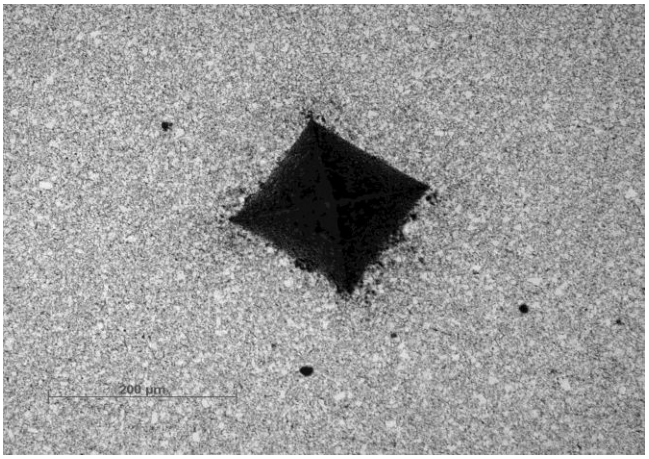


Figure 4.6. Optical micrograph of the WC-10Co alloy showing slightly curved edges of the hardness indentation, and no evidence of cracking at a 30kg load.

The WC-10Co alloy showed slightly curved edges in the hardness indentation (Figure 4.6) which resulted from work hardening that led to a pincushion-shaped indentation.

4.4 Determination of W and V content in the binder

4.4.1 Energy dispersive X-ray analysis (EDX)

The results of the composition of alloys using SEM-EDX are given in Tables 4.4 and 4.5. The EDX system available on the SEM could not detect carbon, because it had a 7.5 μm thick beryllium window between the microscope and the lithium drifted silicon detector, and this absorbs all the carbon X-rays. EDX was also used for the measurement of cobalt content in the mixed carbide grains.

Table 4.4. Average overall compositions (wt%), excluding carbon of the alloys measured by EDX in the JEOL 840 SEM.

Composition (wt%)			
Nominal composition	**W**	**V**	**Co**
WC-10Co	89.1 ± 1.7	-	10.9 ± 1.7
WC-67VC-10Co	26.0 ± 0.7	65.0 ± 1.3	9.0 ± 1.9
WC-30Co	65.6 ± 0.9	-	34.4 ± 0.3
WC-10VC-30Co	58.4 ± 1.2	10.0 ± 1.2	31.6 ± 3.5

EDX in the SEM yielded inaccurate compositions of the small phases, such as the binder, in at least two of the alloys, since X-rays can originate from phases below and surrounding the analyzed area as a result of electron scattering. As a general rule, the interaction volume (with the incident electron beam) producing the X-rays can as much as 3 μm wide and 3 μm deep and possibly even larger (Figure 4.8). While in the TEM, scattering within the sample is much less due to the reduced sample thickness, as a result of the confined space around the sample in the TEM, considerable electron scattering can still occur in the case of EDX measurements. The ideal solution would be to use electron energy loss spectroscopy, EELS, which uses the electrons scattered in the forward direction. Unfortunately, the equipment available turned out to be unreliable.

Table 4.5. Composition (wt%), excluding carbon, of the mixed carbide and binder phases, as measured by EDX in the SEM.

Nominal Compostion	**(V,W,Co)C**			**Co binder**		
	W	**V**	**Co**	**W**	**V**	**Co**
WC-10Co	N/A	N/A	N/A	N/A	N/A	N/A
WC-67VC-10Co	28.1 ± 0.1	71.6 ± 0.2	0.39 ± 0.1	5.4 ± 0.7	3.6 ± 0.9	91.0 ± 1.4
WC-30Co	N/A	N/A	N/A	8.3 ± 1.1	N/A	91.7 ± 1.5
WC-10VC-30Co	58.9 ± 0.6	39.4 ± 0.8	1.7 ± 0.2	7.7± 0.6	0.8 ± 0.3	91.5 ± 1.0

The binder composition on the WC-10Co sample (Table 4.5) could not be determined since the polishing preferentially removed the binder phase.

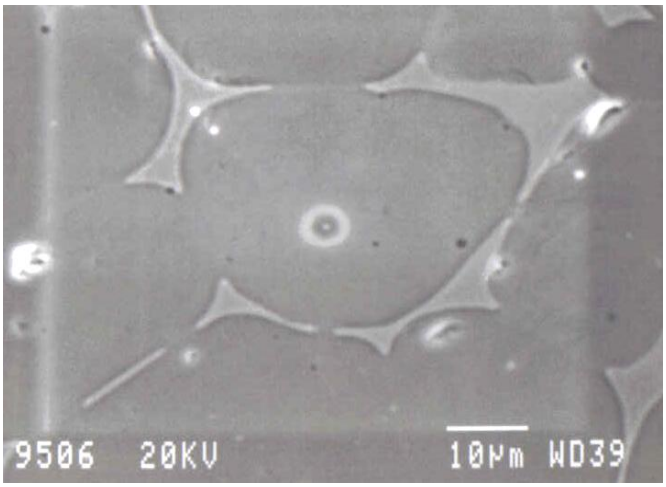


Figure 4.7. SEM image in secondary electron mode of the WC-67VC-10Co alloy showing the contamination spot (centre) resulting from a EDX spot analysis of a (V,W,Co)C grain.

The spectrum in Figure 4.8 confirms the detection of cobalt in the mixed carbide grains of the WC-67VC-10Co alloy. Five different (V,W,Co)C grains were examined for an extended analysis period of 600s each. However, the quantity of the Co could not be accurately determined (Table 4.6), due to contamination build up during the extended analysis period.

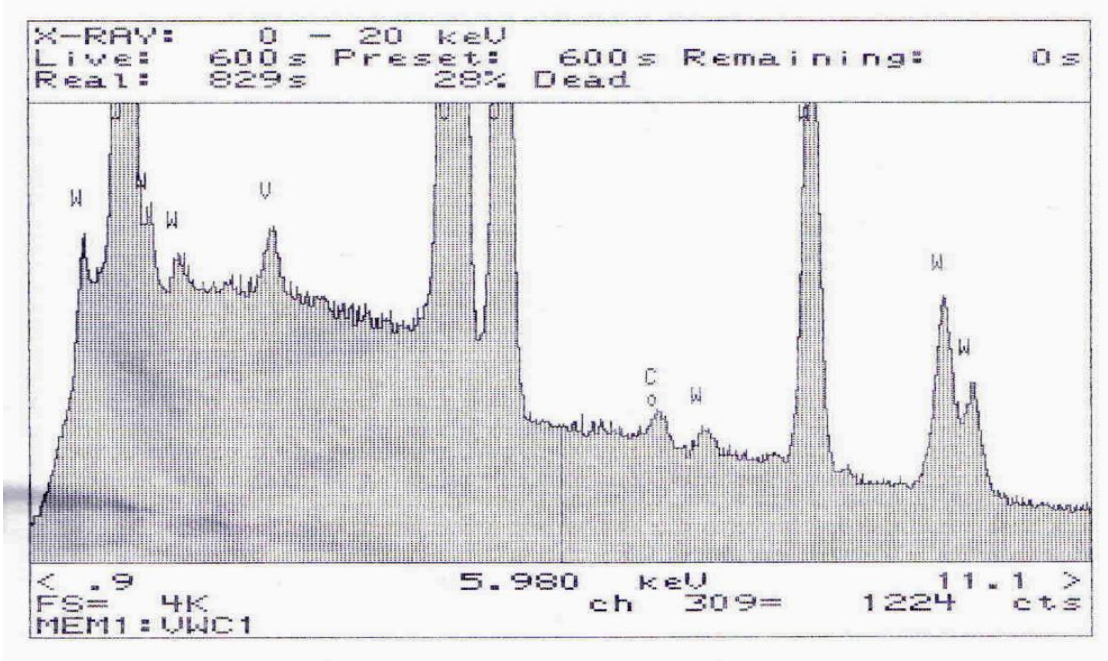


Figure 4.8. EDX spectrum from the (V,W,Co)C phase, showing small a amount of Co.

Table 4.6. Composition (at.%) of the mixed carbide phases, as measured by EDX in the SEM.

Nominal composition	**(V,W,Co)C**			**Empirical formula of (V,W)C**
	W	**V**	**Co**	
WC-67VC-10Co	9.8 ± 0.1	90.2 ± 0.2	___	$(V_{0.9},W_{0.1})C$
WC-10VC-30Co	70.7 ± 0.7	29.3 ± 0.5	___	$(V_{0.7},W_{0.3})C$

The lack of quantification of the Co in the mixed carbide phase by EDX in SEM in the current study is in direct contrast to earlier work (Luyckx, 1996; Broccardo, 2003). Table 4.7 presents results for the mixed carbide phase obtained by Witcomb *et al.* (1997) using EDX in TEM, indicating that Co could be quantified, and that a trend exists towards larger amounts of cobalt in the (V,W,Co)C phase with increasing cobalt content.

Table 4.7. Mixed carbide compositions in the WC-VC-Co alloys of different Co content, ignoring carbon (Witcomb *et al.*, 1997) obtained by EDX in TEM. (* = current work)

Specimen	Compositions in (V,W,Co)C (at.%)		
	V	W	Co
WC-10VC-10Co	59.2 ± 6.6	39.4 ± 3.3	1.4 ± 0.2
WC-10VC-12Co	55.8 ± 5.5	41.8 ± 4.3	2.4 ± 0.2
WC-10VC-15Co	54.7 ± 5.2	42.7 ± 4.3	2.6 ± 0.5
WC-10VC-30Co*	68.6 ± 0.7	28.4 ± 0.5	3.0 ± 0.5

The very low quantities of Co in the mixed carbide could have important implications for corrosion, because Co is a major player in the corrosion of WC-Co (Human, 1994).

4.4.2 Magnetic saturation

The magnetic saturation is the maximum magnetization that can be induced in a material. In WC-Co, the magnetic saturation determines the amount of tungsten dissolved in the cobalt binder, which in turn affects the corrosion resistance of cemented carbides. The average results of five magnetic saturation measurements are given in Table 4.8. The WC-Co material had a much smaller error than WC-67VC-10Co.

Table 4.8. Magnetic saturation measurements.

Specimen	Magnetic saturation, $4\sigma\pi$ ($Gauss.cm^3.g^{-1}$)
WC-10Co	195.78 ± 0.12
WC-67VC-10Co	194.91 ± 0.54

4.5 Determination of fcc-Co/hcp-Co ratio in the binder

4.5.1 X-ray diffraction (XRD)

The XRD patterns for the WC-10Co, WC-67VC-10Co, WC-30Co and WC-10VC-30Co alloys are given in Figures 4.9 to 4.12. The phases detected by XRD were the same to those obtained by EDX in SEM (Table 4.1). The data are given in Appendix A.

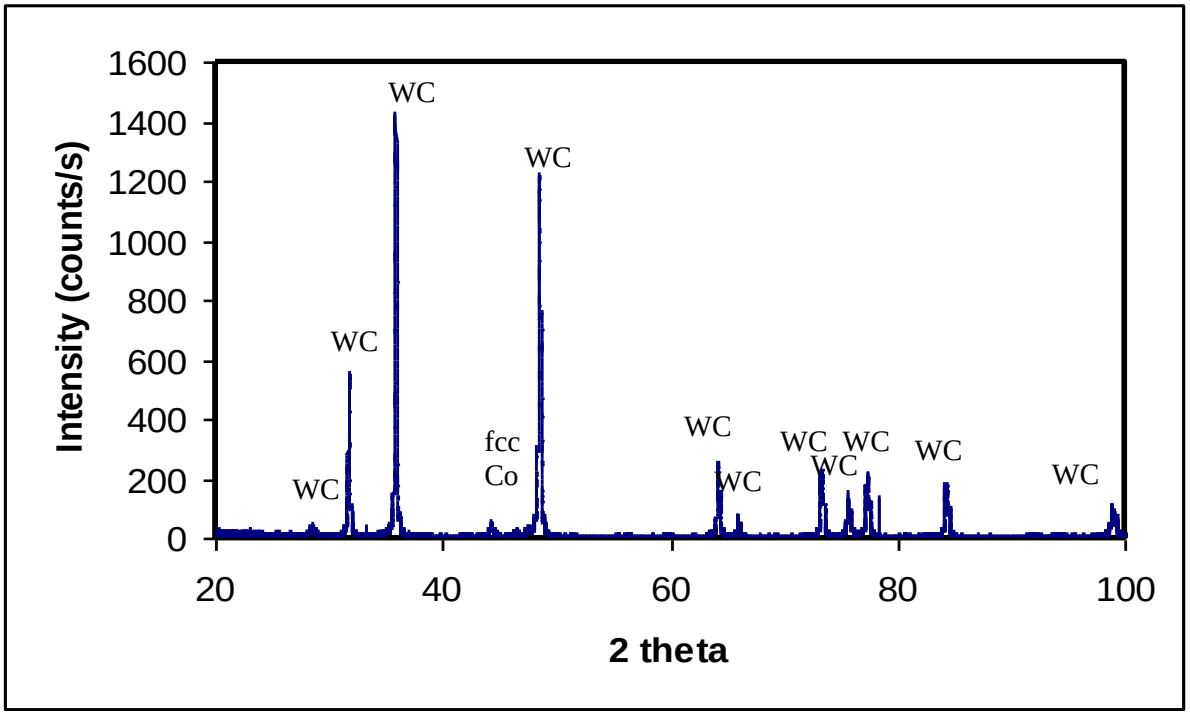


Figure 4.9. XRD pattern of the WC-10Co alloy.

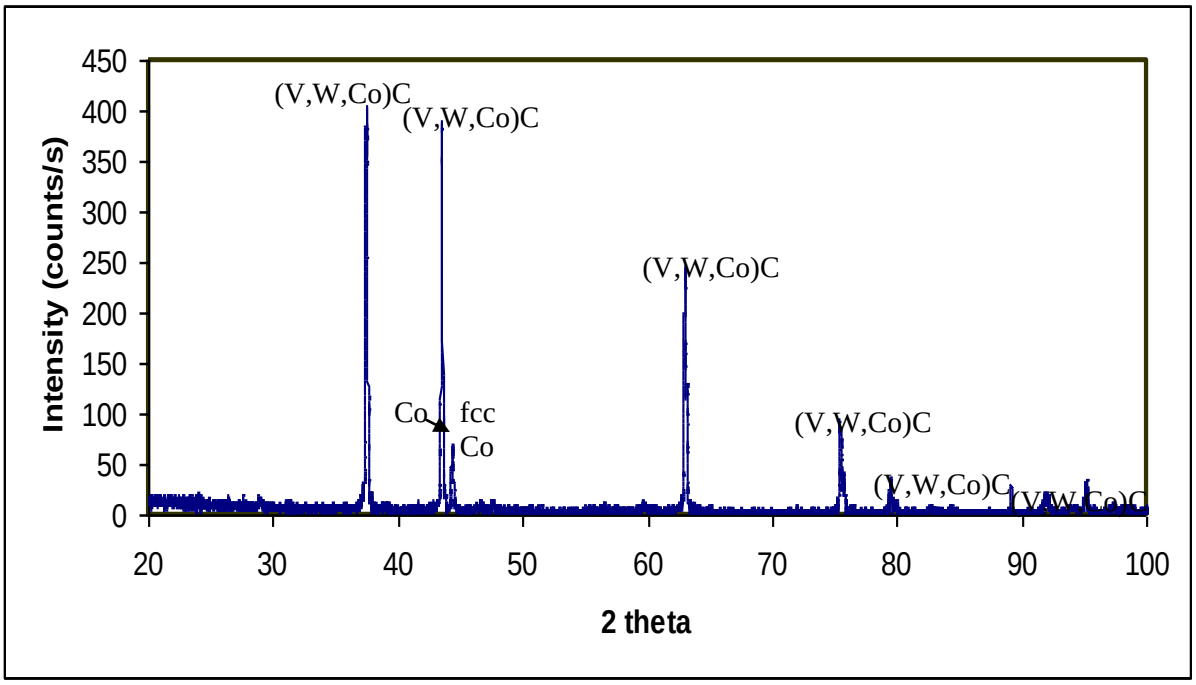


Figure 4.10. XRD pattern from the WC-67VC-10Co alloy showing the absence of any WC phase.

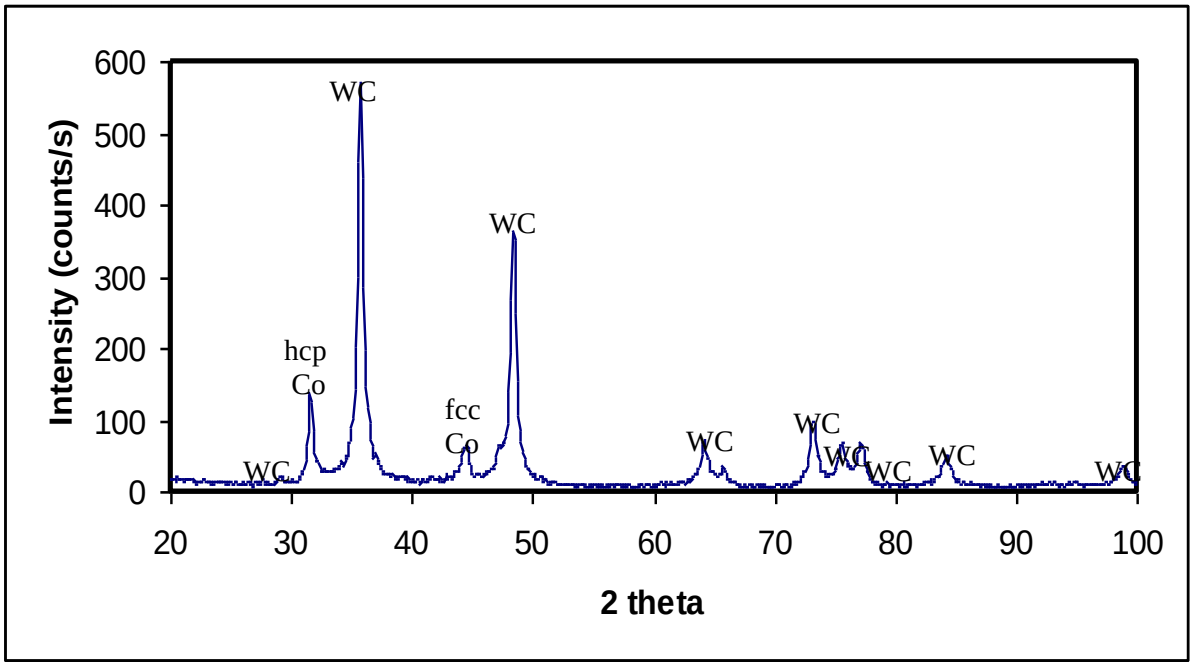


Figure 4.11. XRD pattern of WC-30Co showing the presence of fcc-Co and hcp-Co.

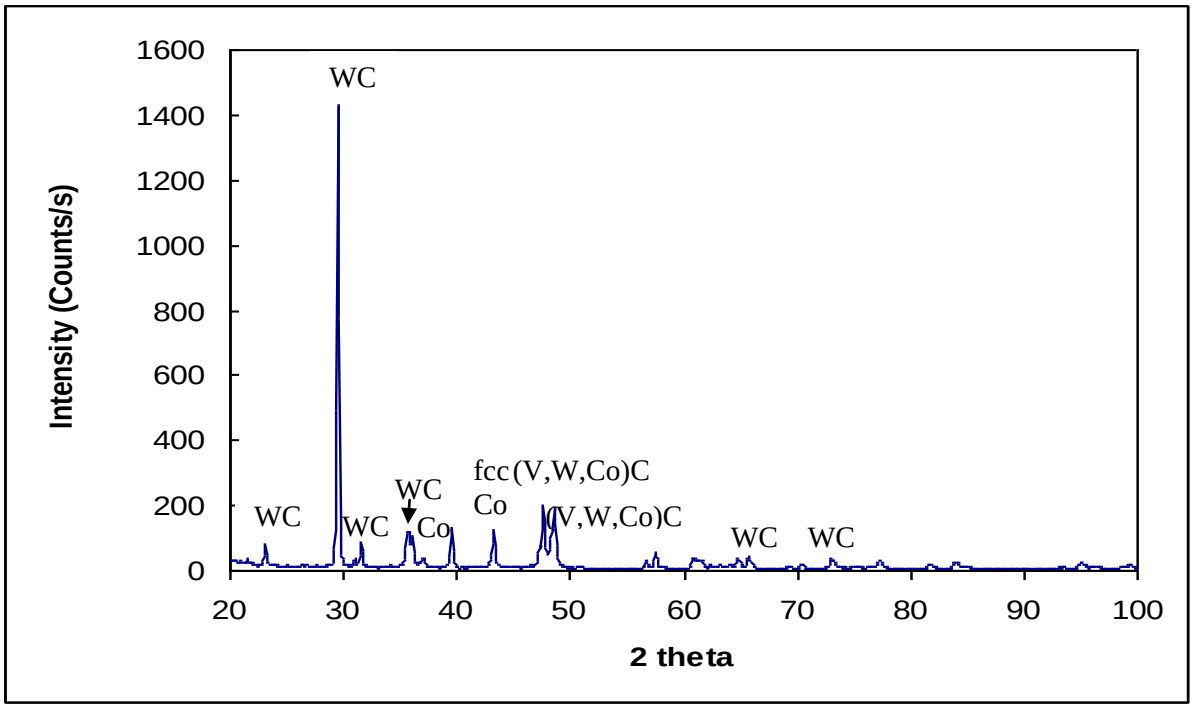


Figure 4.12. XRD pattern of WC-10VC-30Co showing the presence of fcc-Co and hcp-Co.

Qualitative phase analysis was performed using information from the JCPDS database and Rietveld refinement method. Characteristic superimposed experimental and calculated patterns are shown in Figures 4.13 and 4.14, while the differences between the curves are given in Figures 4.15 and 4.16. The results of the quantitative analysis are given in Table 4.9 taken from an average of three measurements. The lattice parameters of the phases are presented in Table 4.10, the surfaces of the samples were thermal spray coated, ground again, polished and measured more than once as denoted with (1) and (2). The fcc to hcp cobalt ratio of each sample obtained using the Rietveld method are given in Table 4.11. The ratios in Table 4.11 confirmed that VC stabilized the fcc Co as noted by Broccardo in 2003, since the ratio of fcc/hcp cobalt was higher in the specimens with VC than in the corresponding conventional WC-Co alloys. The increase is small in the case of 10 wt% Co, roughly 3% as against a 133% increase for 30 wt% Co.

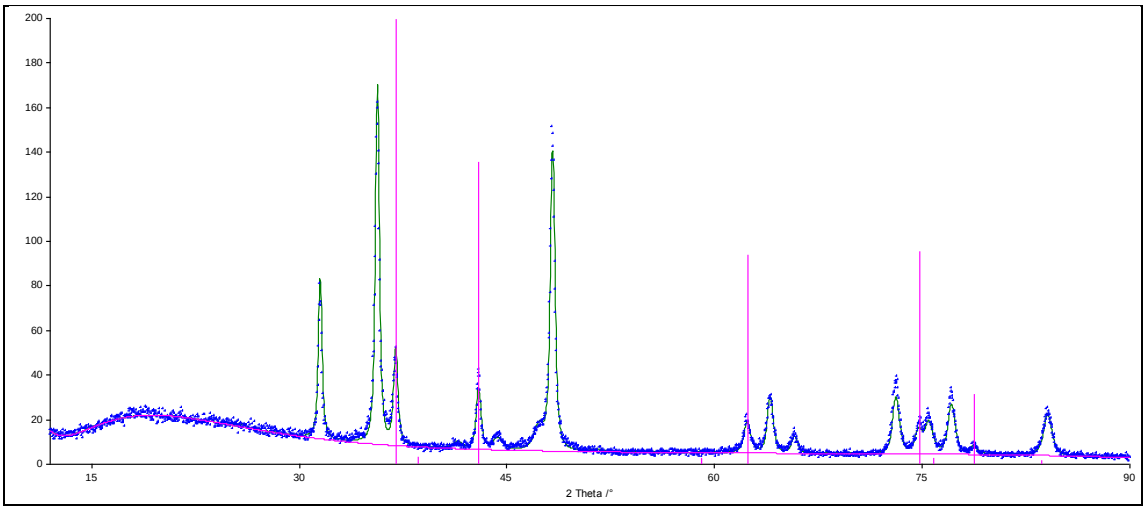


Figure 4.13. Rietveld pattern of WC-VC-Co alloy showing V_8C_7 (red lines), measured data (blue) and calculated data (green).

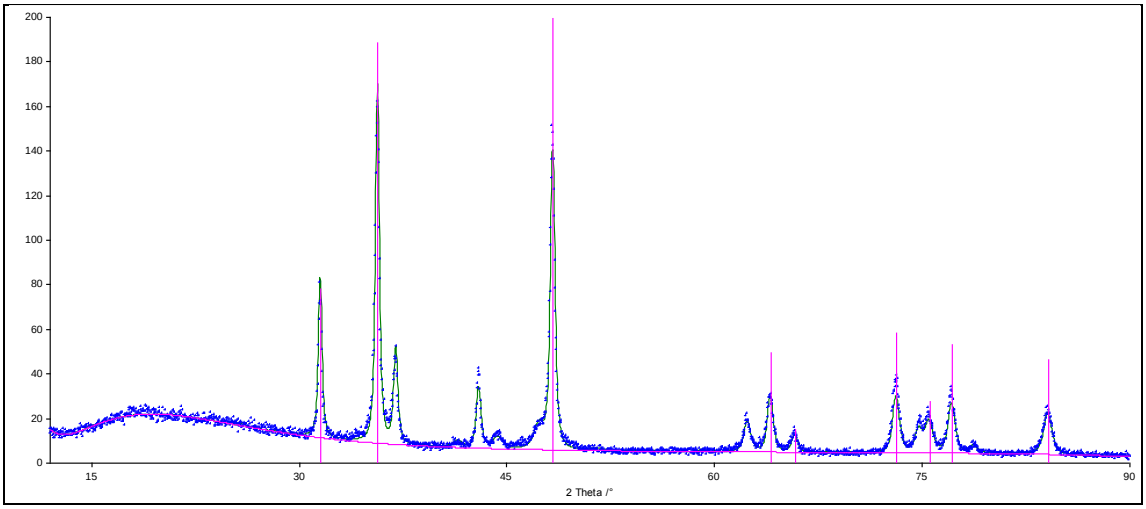


Figure 4.14. Rietveld pattern of WC-VC-Co alloy showing WC (red lines), measured data (blue) and calculated data (green).

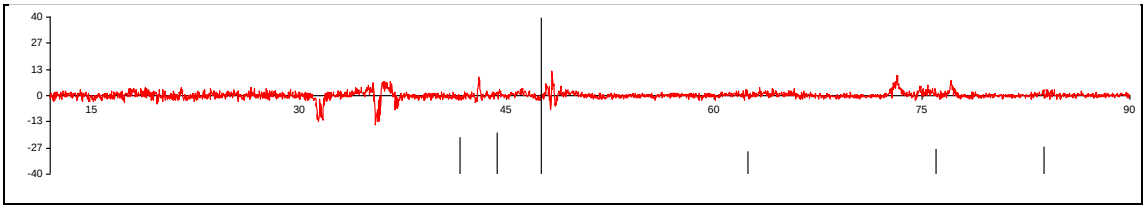


Figure 4.15. Rietveld pattern showing the difference between the calculated and measured data (red) and hcp Co (black lines).

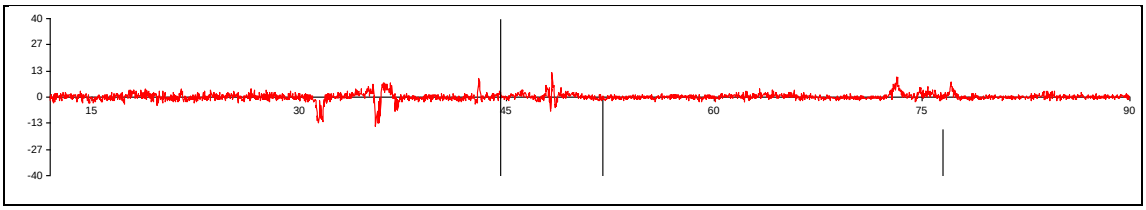


Figure 4.16. Rietveld pattern showing the difference between the calculated and measured data (red) and fcc Co (black lines).

Table 4.9. Quantitative analysis of chemical composition of the phases present in the alloys (wt%).

Sample	**$V_{8(1-x)}C_7$**	**WC**	**V_8C_7**	**Co (hexagonal)**	**Co (cubic)**
WC-30Co	N/A	70.6 ±1.3	N/A	26.9 ±1.4	2.3 ± 1.0
WC-10VC-30Co	0.73	52.4 ± 1.4	27.7 ± 1.0	16.5 ± 1.6	3.5 ± 1.3
WC-10Co	N/A	95.0 ± 3.6	N/A	3.4 ± 2.9	1.6 ± 1.9
WC-67VC-10Co	0.77	-	87.9 ± 2.4	2.7 ± 2.3	9.4 ± 1.4

Table 4.10. Lattice parameters of the phases present in the alloys obtained from Rietveld analysis (nm).

Sample	WC	V_8C_7	Co (hexagonal)	Co (cubic)
WC-30Co (1) Mono	a = 0.29098 ± 0.00003 c = 0.28405 ± 0.00003	N/A	a = 0.25169 ± 0.0001 c = 0.40800 ± 0.0002	___
WC-30Co (2) Mono	a = 0.29085 ± 0.0000096 c = 0.28389 ± 0.000013	N/A	a = 0.25174 ± 0.000085 c = 0.40722 ± 0.00025	a = 0.35435 ± 0.00020
WC- 30Co Mono, polished	a = 0.29085 ± 0.0000096 c = 0.28389 ± 0.000013	N/A	a = 0.25160 ± 0.000085 c = 0.40746 ± 0.00025	a = 0.35425 ± 0.00022
WC-10VC-30Co (1) Mono	a = 0.29092 ± 0.000020 c = 0.28396 ± 0.000024	a = 0.84249 ± 0.000080	a = 0.25168 ± 0.00014 c = 0.40752 ± 0.00049	a = 0.35499 ± 0.00045
WC-10VC-30Co (2) Mono	a = 0.29092 ± 0.000020 c = 0.28396 ± 0.000024	a = 0.84249 ± 0.000081	a = 0.25169 ± 0.00014 c = 0.40751 ± 0.00049	a = 0.35502 ± 0.00045
WC-10VC-30Co Mono, polished	a=0.290860 ± 0.00009 c=0.283920 ± 0.00009	a = 0.84229 ± 0.0009	a = 0.25123 ± 0.0004 c = 0.40760 ± 0.0008	a = 0.35460 ± 0.00045
WC-10 Co (1)*	a = 0.29055 ± 0.000019 c = 0.28381 ± 0.000028	N/A	a = 0.25358 ± 0.00068 c = 0.40780 ± 0.0027	a = 0.35533 ± 0.00062
WC-10Co (2)*	a = 0.29116 ± 0.00100 c = 0.28425 ± 0.00100	N/A	a = 0.25271 ± 0.0012 c = 0.4150	a = 0.35591 ± 0.0012
WC-10Co polished*	*a* =0.29070 ± 0.000020 *c* =0.28380 ± 0.000024	N/A	___	a = 0.35645 ± 0.00045
WC-67VC-10Co*	___	a = 0.83614 ± 0.000017	a = 0.25018+-0.00068 c = 0.4090+-0.0029	a = 0.355569+-0.000047
WC-67VC-10Co polished*	___	a = 0.83618 ± 0.000017	___	a = 0.355561+-0.00006

(1)-First measurement
(2)-Second measurement
Mono - measured with a secondary monochromator.
(*)- measured using a Ni Filter.

Table 4.11. Ratio of fcc-Co to hcp-Co in the alloys.

Sample	fcc Co	hcp Co	fcc Co/hcp Co
WC-10Co	6.1	1.8	3.39
WC-67VC-10Co	9.4	2.7	3.48
WC-30Co	2.5	27	0.09
WC-10VC-30Co	3.5	16.5	0.21

4.5.2 TEM microstructure

TEM studies of the WC-30Co revealed a high density of stacking faults in the Co binder (Figure 4.17). The Co phase in the WC-10VC-30Co alloy (Figure 4.18) was expected to have fewer stacking faults, since VC is known to stabilize fcc cobalt. Stacking faults in the Co phase can also be used to determine the ratio of cubic to hexagonal Co using electron diffraction. The WC-30Co hardmetal had many stacking faults, with smaller stacking faults between the longer stacking faults, whereas with WC-10VC-30Co, there were only parallel sets of stacking faults in the finer grains, which were irregular distributed.

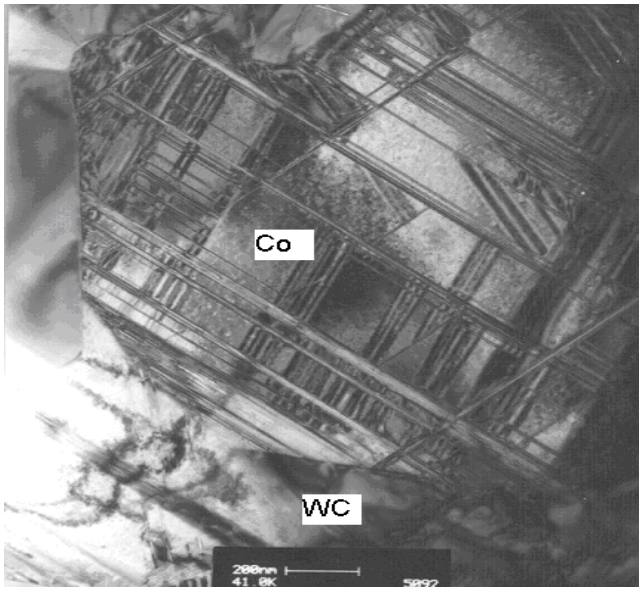


Figure 4.17. TEM image of the WC-30Co alloy showing stacking faults in Co.



Figure 4.18. TEM image of the WC-10VC-30Co alloy showing parallel stacking faults in Co.

The WC-10VC-30Co alloy appeared to contain more dislocations in the WC phase than the WC-Co alloy, and also contained voids, Figures 4.19, 4.20 and 4.21. The mixed carbide grains were large, (V,W,Co)C, and uniformly distributed, essentially defect free and typically contained some small WC grains around 0.2µm in size, Figure 4.22.

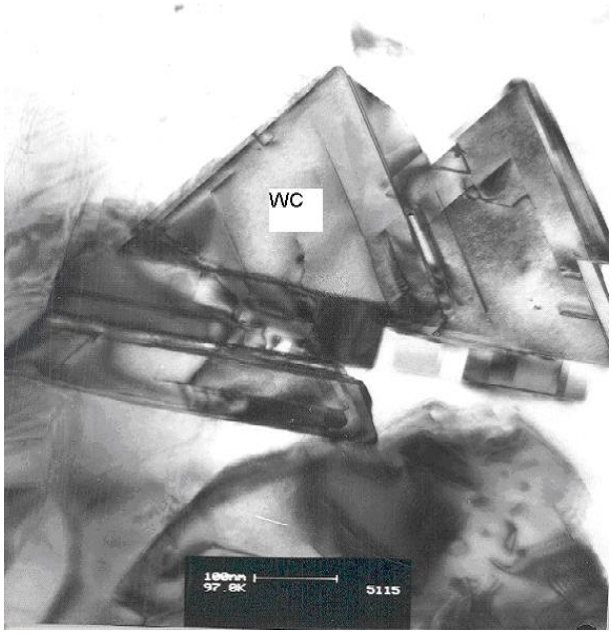


Figure 4.19. TEM image of the WC-30Co alloy showing the triangular cross-section of some WC grains containing faults and dislocations.

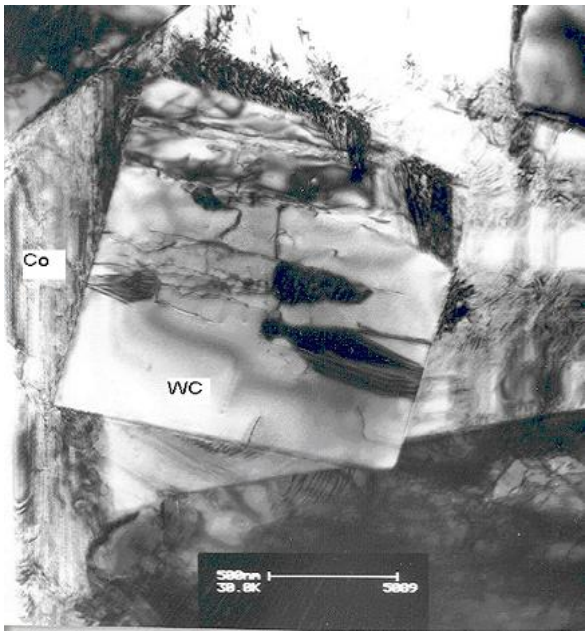


Figure 4.20. TEM image of the WC-30Co alloy showing dislocations in the WC grains.

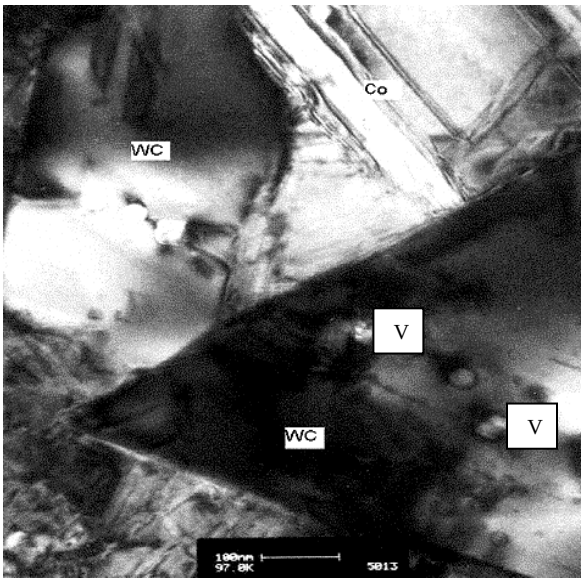


Figure 4.21. TEM image of the WC-10VC-30Co alloy showing dislocations and voids (V) in the WC grains.

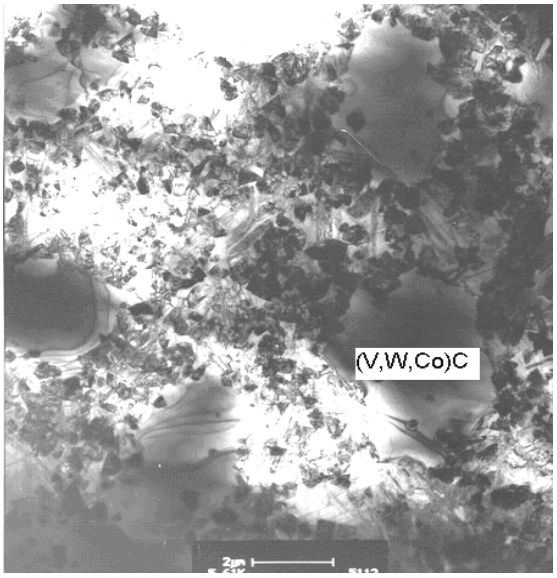


Figure 4.22. Low magnification TEM image of the WC-10VC-30Co alloy, showing large (V,W,Co)C grains and very small WC grains.

4.5.3 Lattice parameter determination in the TEM

The calculated lattice parameters of the Co, (V,W,Co)C and WC phases in WC-10VC-30Co from electron diffraction are given in Table 4.12. The mixed carbide grains studied were confirmed as the fcc phase by the lattice parameter of 0.422 ± 0.02 nm in the WC-10VC-30Co alloy. This agrees with a value of 0.421 ± 0.02 nm previously reported by Witcomb *et al.* (1998) for the mixed carbide in a WC-10VC-10Co alloy containing eta phase. Evidence of short range ordering has been found in the four mixed carbide grains studied, as shown for WC-10VC-30Co alloy in Figure 4.23. The diffuse scattering due to the ordering can be seen as curved streaks surrounding the diffraction spots.

Table 4.12. Lattice parameters of the phases in the WC-10VC-30Co alloy.

Phase	**Structure**	**Lattice parameter, *a* (nm)**	**Lattice parameter, *c* (nm)**	**Literature values of the *a* and *c* values (nm) (Edington, 1976)**
WC	hcp	0.291 ± 0.02	0.280 ± 0.02	a = 0.291, c = 0.283
Co	fcc	0.349 ± 0.05	___	a = 0.354
(V,W,Co)C	fcc	0.422 ± 0.02	___	a = 0.421

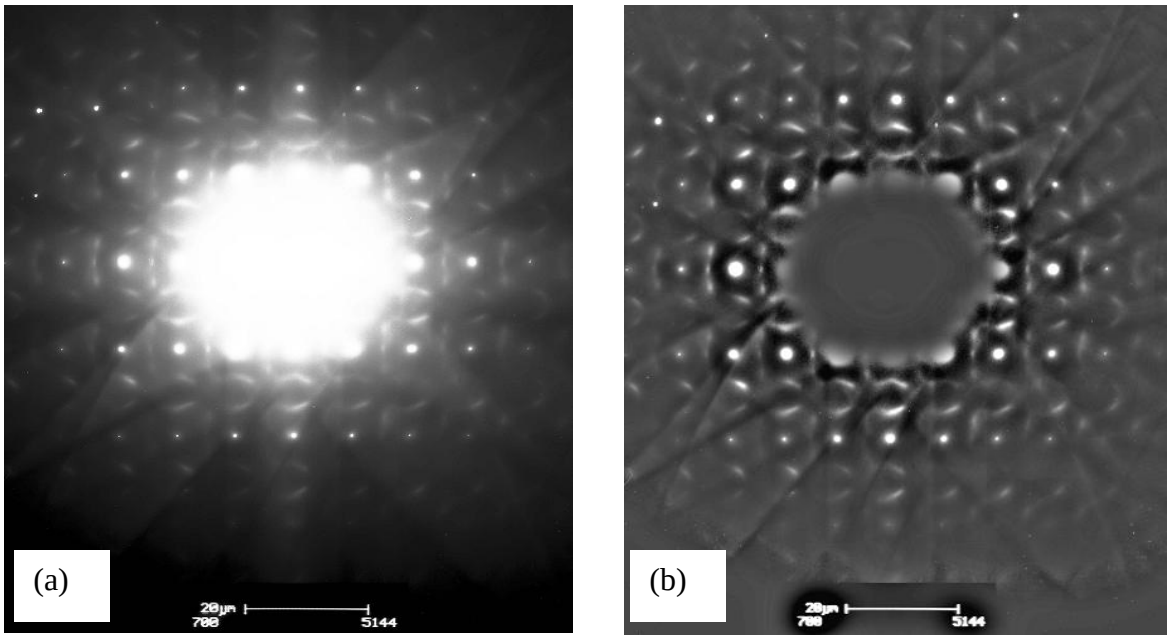


Figure 4.23. (a) TEM diffraction pattern of the mixed carbide grain, (V,W,Co)C, in the WC-10VC-30Co alloy, (b) image in (a) after being subjected to a high pass band filter and auto contrast/brightness to emphasise the ordering intensities.

4.6 Results of corrosion tests

4.6.1 Electrochemical corrosion tests

Three scans for each sample of WC-10Co and WC-67VC-10Co were performed in 1N sulfuric acid solution. The results are shown in Figures 4.24 and 4.25, and indicate that the polarisation behavior had excellent reproducibility. The corrosion current densities were calculated by using the Tafel extrapolation method (Jones, 1996). Table 4.13 lists the average corrosion potentials (E_{corr}) and current densities (i_{corr}) that were obtained from the polarisation scans. The corrosion potentials of the WC-10Co and WC-67VC-10Co alloys were about -240 mV and -310 mV respectively.

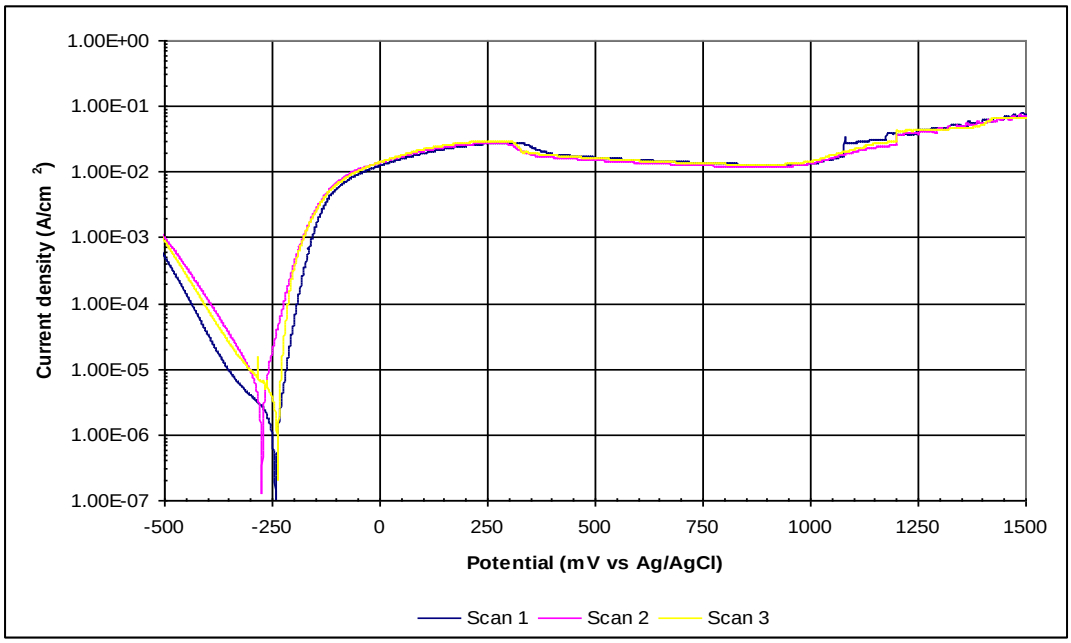


Figure 4.24. Potentiodynamic polarisation scans obtained from one specimen of WC-10Co alloy, after each re-polishing, showing reproducibility.

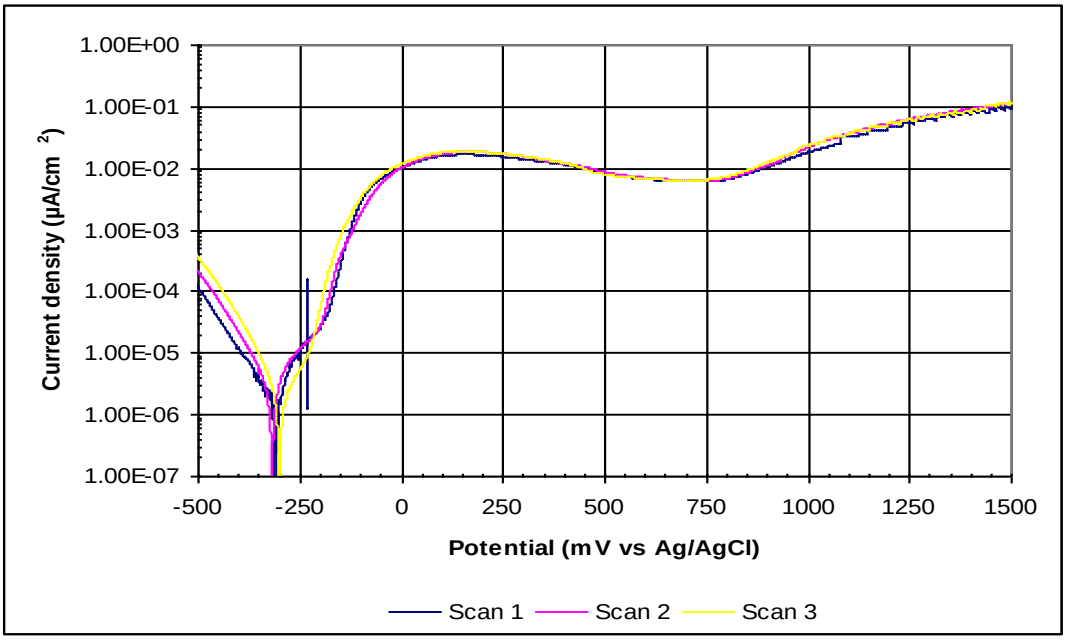


Figure 4.25. Potentiodynamic polarisation scans obtained from one specimen of WC-67VC-10Co alloy, after each re-polishing, showing reproducibility.

Table 4.13. Electrochemical corrosion parameters.

Test samples	**E_{corr} (mV vs. Ag/AgCl)**	**i_{corr} (mA/cm^2)**
WC-10Co	-240.4 ± 4.6	221 ± 57.9
WC-67VC-10Co	-309.7 ± 13.2	215 ± 21.2

The potentiodynamic polarization curves (Figures 4.24 and 4.25) indicate pseudopassivity, a slight drop in current density after the maximum current densities were reached, as already demonstrated by Human (1994). The pseudopassivity region was longer for the WC-10Co grade than for the VC-WC-grade material. This potential region was 350 mV to 950 mV for the WC-10Co alloy, and from 500 mV to 750 mV for WC-67VC-10Co alloy. The corrosion potential, E_{corr}, is a measure of reactivity of a material (Jones, 1996), and here shows that the WC-VC-alloy was more reactive than the WC-Co grade. Even then, the corrosion current densities were similar, indicating that any corrosion that occurred would have the similar kinetics. The high negative potential shows the driving force for dissolution of the material was high, while the converse was true for a high positive potential (Simard, 2000). The rate of corrosion is given by the corrosion current density, i_{corr}; this implies that the higher the current densities, the higher the corrosion rates.

The SEM micrographs of the WC-10Co and WC-67VC-10Co alloys before and after corrosion testing are shown in Figures 4.26 to 4.30. A corrosion product formed on specimens after testing, but appeared to be a continuous (but cracked) layer only for WC-10Co (Figure 4.27), but patchy for WC-67VC-Co (Figure 4.30). The corrosion by-products were not analyzed, but were expected to be hydrated WO_3, and in the high VC content grade, also some $VOSO_4.H_2O$ (Konadu *et al.*, 2010). All specimens were leached of the Co binder (Figure 4.28 and 4.30), indicating that the dissolution of the binder constituted the major form of attack. There was some attack on WC grains in the WC-10Co alloy (Figure 4.28), but the mixed carbide in WC-67VC-Co appeared to withstand corrosion better (Figure 4.30). Figure 4.30 shows corrosion product with no Co after corrosion tests.

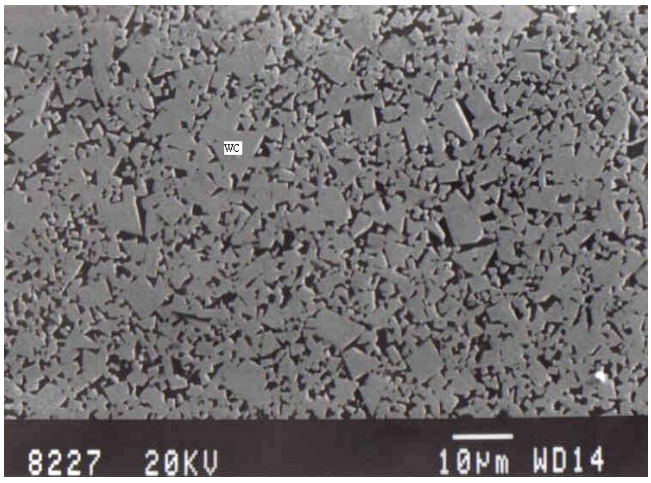


Figure 4.26. SEM image in backscattered electron mode of the WC-10Co alloy, before electrochemical corrosion testing, showing WC (light) and Co (dark).

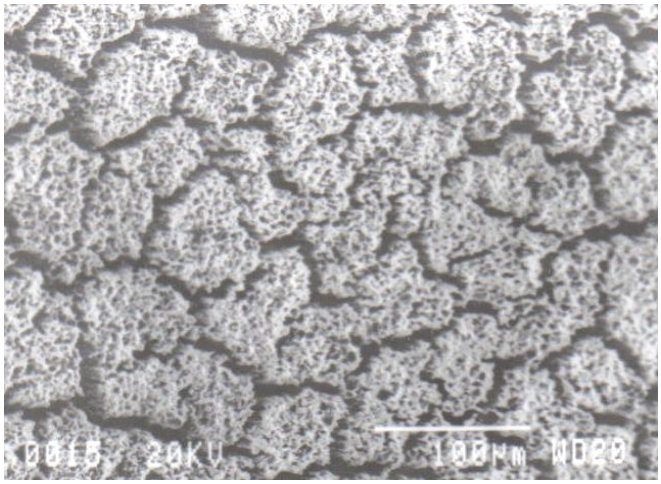


Figure 4.27. SEM image in secondary electron mode of the WC-10Co alloy, after electrochemical corrosion testing, showing a surface film on the WC grains (light) as well as the removal of Co.

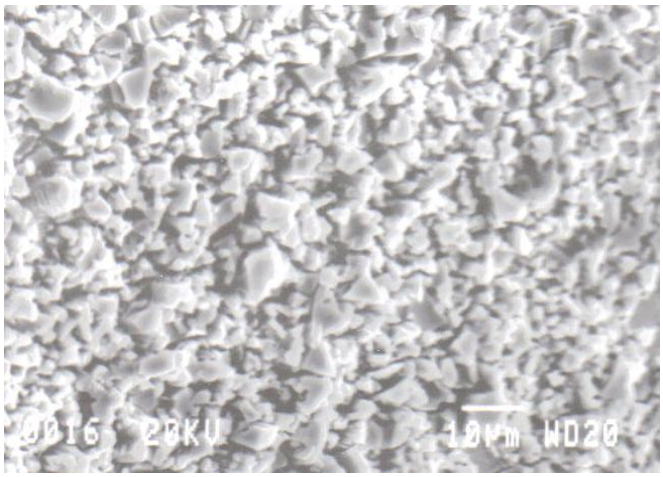


Figure 4.28. SEM image in secondary electron mode of the WC-10Co alloy, after electrochemical corrosion testing, showing some attack on WC grains (light) as well as the removal of Co.

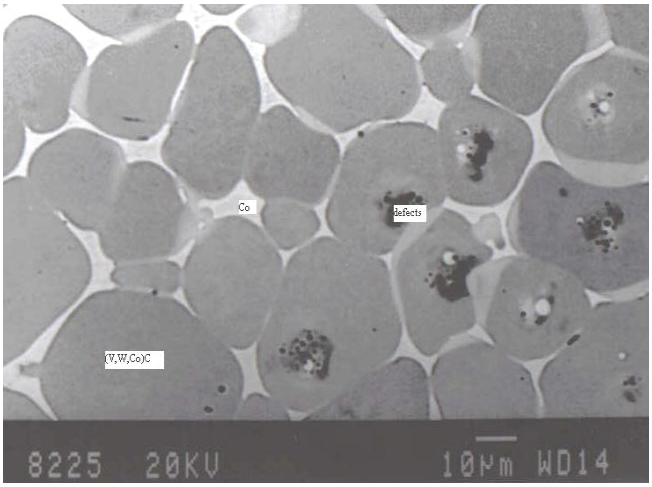


Figure 4.29. SEM image in backscattered electron mode of the WC-67VC-10Co alloy, before electrochemical corrosion testing, showing Co (light), (V,W,Co)C (medium) and defects (dark).

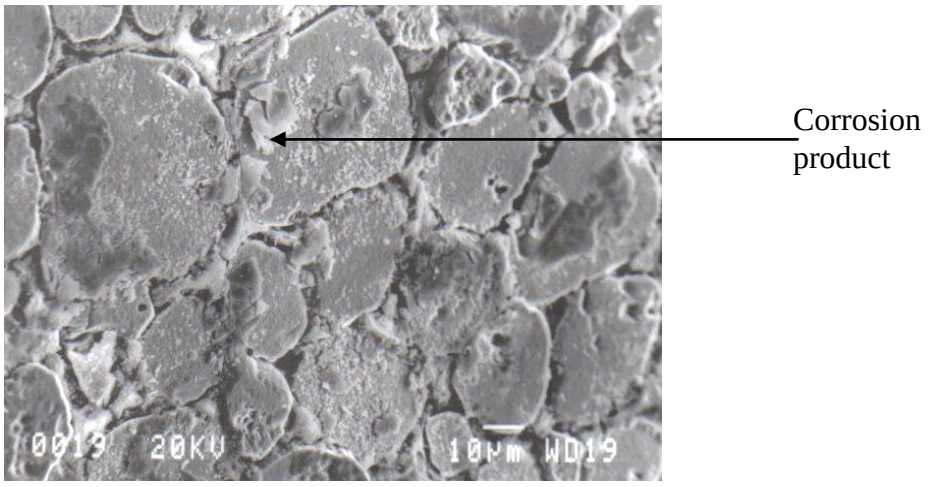


Figure 4.30. SEM image in secondary electron mode of the WC-67VC-10Co alloy, after electrochemical corrosion testing, showing a corrosion product and no Co.

4.6.2. Immersion corrosion testing

Eight samples of WC-Co and WC-10VC-Co alloys which had been subjected to immersion corrosion testing by Broccardo (2003) were examined using the SEM. This was done in an attempt to indicate the possible reasons for the difference in the corrosion behaviour of the alloys. Figures 4.31 to 4.38 are micrographs taken at approximately the same magnification for ease of comparison of the different samples. The dark regions were holes, which remained after the Co binder had been removed by corrosion. Some portions of the dark areas were probably from the loss of carbide grains as the supporting binder cement was removed.

The SEM micrographs (Figures 4.31- 4.37) confirm that the WC grain size was much larger in the WC-Co alloys than in WC-VC-Co. This was expected because VC inhibits grain growth. Alloys with no vanadium consisted entirely of a WC skeleton, whereas those with vanadium had regions of mixed carbide between WC grains. In the WC-10VC-30Co alloy, the mixed carbide formed as a small number of large grains, seemingly evenly dispersed, while in 9, 10, 12 and 15 wt% Co alloys, the mixed carbide formed as a large number of small grains (there was only 10 wt% VC in all of the samples.)

In Figure 4.38, where the transition between corroded and uncorroded material is shown, scattered large dark regions in the corroded region occured, not only from the loss of cobalt binder, but also from the loss of some WC grains which were removed during polishing due to the absence of the binder material.

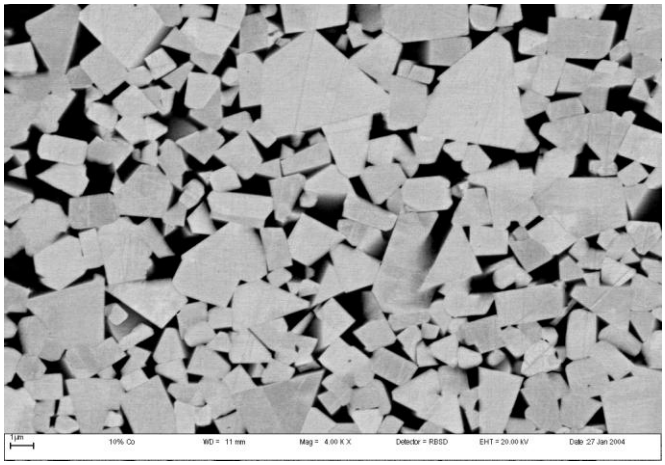


Figure 4.31. SEM image in backscattered electron mode of the corroded WC-10Co alloy, showing no Co (holes (dark)), and WC (light).

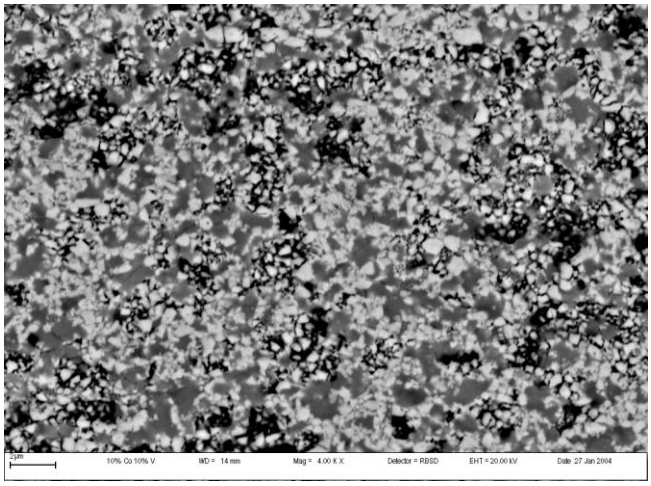


Figure 4.32. SEM image in backscattered electron mode of the corroded WC-10VC-10Co alloy, showing no Co (holes (dark)), no attack on the WC (light) and (V,W,Co)C (medium grey).

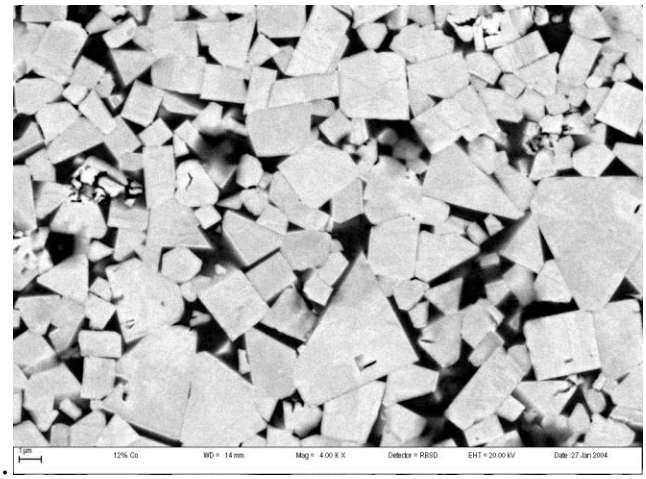


Figure 4.33. SEM image in backscattered electron mode of the corroded WC-12Co alloy, showing no Co (holes (dark)) and WC (light).

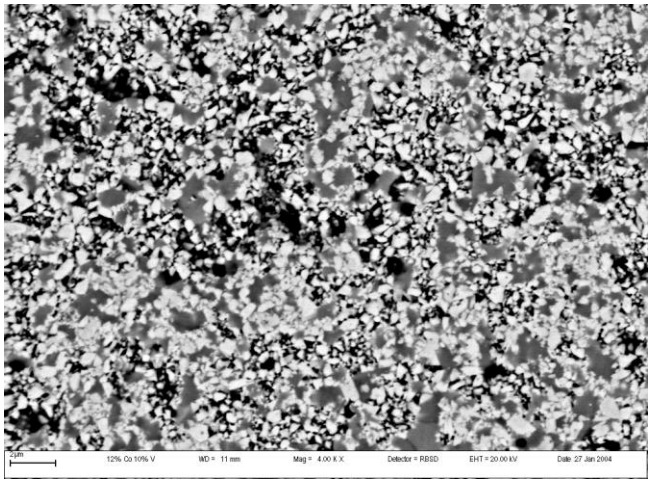


Figure 4.34. SEM image in backscattered electron mode of the corroded WC-10VC-12Co alloy showing no Co (holes (dark)), no attack on the WC (light) and (V,W,Co)C (medium).

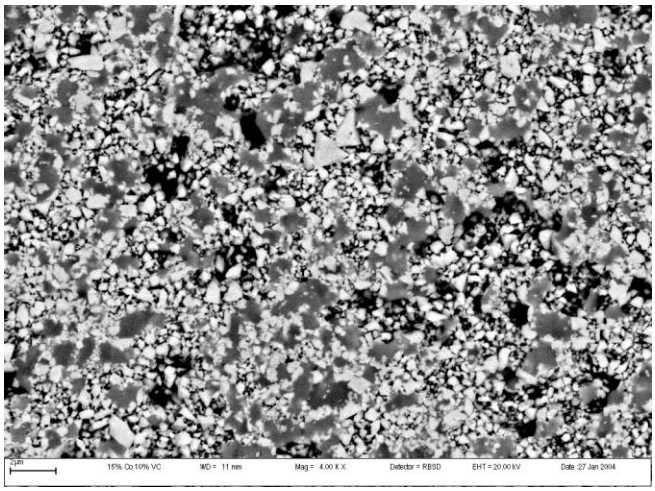


Figure 4.35. SEM image in backscattered electron mode of the corroded WC-10VC-15Co alloy showing no Co (holes (dark)), no attack on WC and (V,W,Co)C.

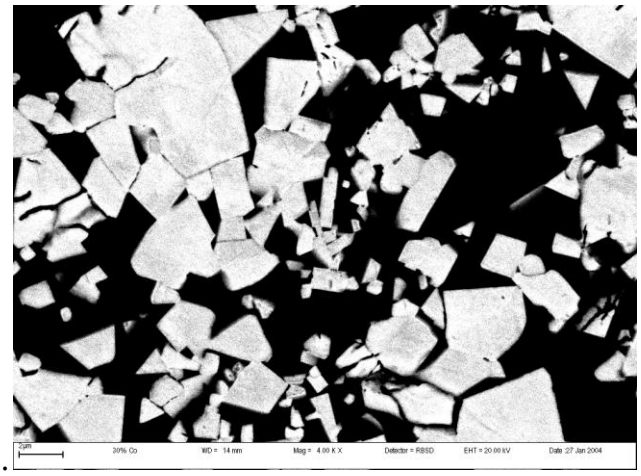


Figure 4.36. SEM image in backscattered electron mode of the corroded WC-30Co alloy showing no Co (holes (dark)) and WC (light).

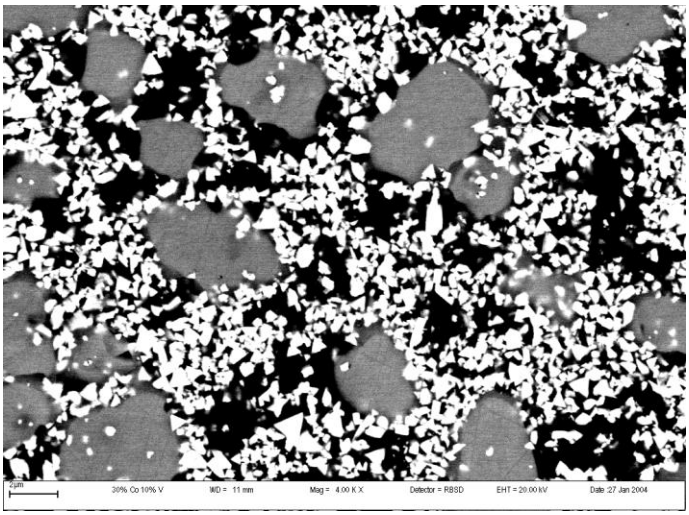


Figure 4.37. SEM image in backscattered electron mode of the corroded WC-10VC-30Co alloy, showing no Co (holes (dark)), no attack on WC (light), and (V,W,Co)C (medium).

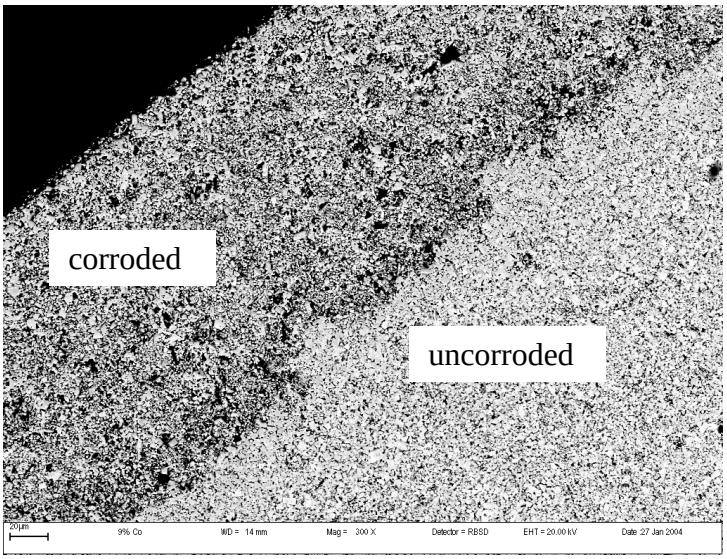


Figure 4.38. SEM image in backscattered electron mode of a polished cross section of the WC-9Co alloy showing the corroded and the uncorroded regions (Broccardo, 2003).

4.6.3. Depth of the corroded layer on the immersion corrosion test samples

The cross-sections of the eight immersion corrosion WC-Co and WC-10VC-Co samples (listed in the experimental procedure, Table 3.1) were studied by optical microscopy to measure the depth of the corroded layer. The depth of the corroded layer for each alloy is given in Table 4.14, showing the current re-measurements and Broccado's (2003) original data without standard deviations.

Table 4.14. Depth of the corroded layers on the immersion tested samples.

Sample	**Maximum corrosion depth (mm) (current work)**	**Maximum corrosion depth (mm) from the same samples. (Broccardo, 2003)**
WC-9Co	0.15 ± 0.009	0.21 ± 0.016
WC-10Co	0.21 ± 0.004	0.22 ± 0.000
WC-12Co	0.19 ± 0.004	0.18 ± 0.012
WC-30Co	0.13 ± 0.002	0.15 ± 0.005
WC-10VC-10Co	1.26 ± 0.021	1.22 ± 0.009
WC-10VC-12Co	0.11 ± 0.075	0.13 ± 0.000
WC-10VC-15Co	0.39 ± 0.011	0.56 ± 0.016
WC-10VC-30Co	0.20 ± 0.009	0.28 ± 0.000

In most cases, the re-measurements showed general agreement with those of Broccardo (2003), as shown in Figures 4.39 and 4.40. In the cases of significant disagreement (e.g. WC-9Co, WC-10VC-15Co and WC-10VC-30Co), it is possible that the fragile corroded layer was damaged or partly lost during handling after Broccardo's measurements were made. This should have made the current values smaller, due to material loss. This was the case for all the differences, except for the WC-12Co and WC-10VC-10Co. The reasons for the differences could have been larger errors than indicated, the entire sample was not checked (and the corrosion depths were not homogeneous) and part of the sample fell off during handling. The samples were not repolished since the corroded layer could have been affected.

The results indicate that, in general, at a constant Co content, introducing VC leads to deeper corroded layers.

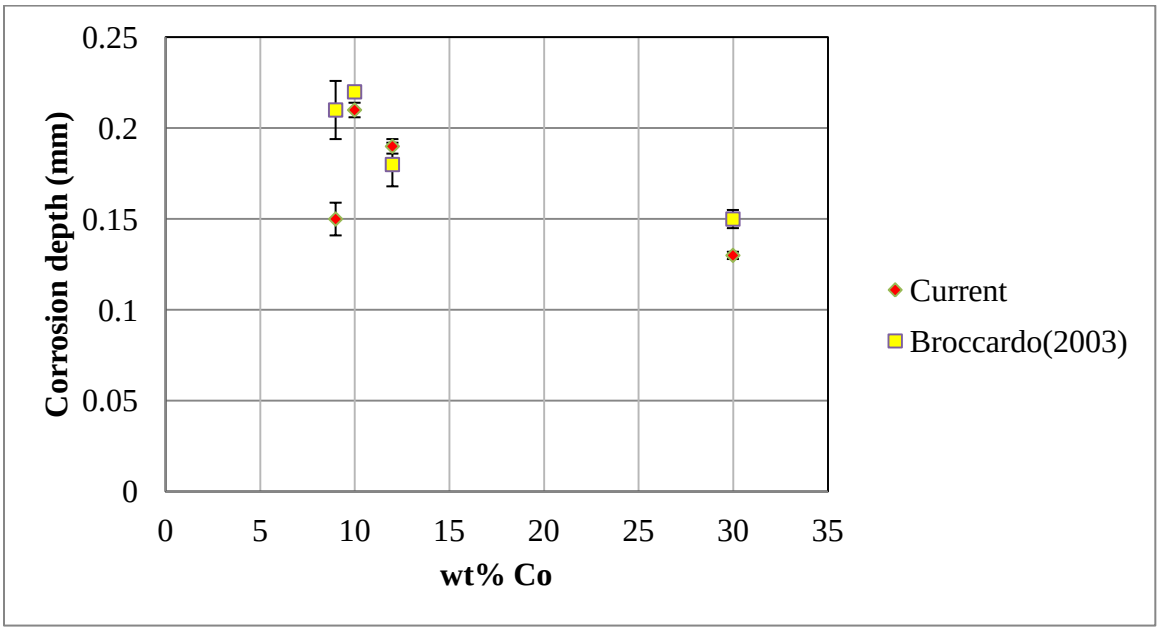


Figure 4.39. Comparison of the corrosion depth of the WC-Co alloys with cobalt content (wt%).

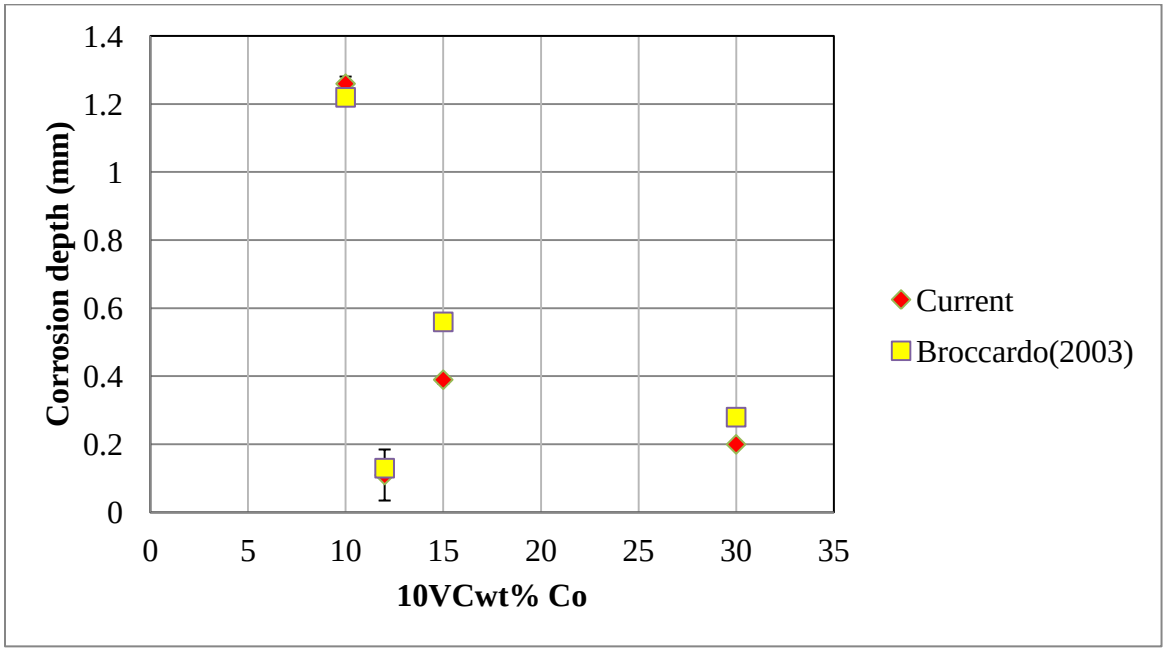


Figure 4.40. Comparison of the corrosion depth of the WC-10VC-Co alloys with cobalt content (wt%).

Chapter 5

Discussion

The discussion of the results of this study is in two parts. The first part puts the characteristics of the test specimens in perspective by comparing their physical, microstructural and phase characteristics to the results of other researchers. The second part addresses the hypotheses of the research.

5.1 Characteristics of the test specimens

5.1.1 Density

It was noted in Section 4.2 that the introduction of large amounts of VC to WC-Co lowers the density of the resulting component compared to the conventional WC-Co grade. This observation of decreased density was first noted by Luyckx *et al.* (1994, 1996), and is one of the reasons for research on WC-VC-Co hardmetals (VC is lighter than WC and has a slightly lower melting point, so less energy utilized to fuse/melt). The density reduction occurs because the density of VC, at 5.6g/cm^3, is about one third the density of WC, which is 15.6g/cm^3 (Luyckx, 1994).

5.1.2 Hardness test

The hardness of the specimens decreased with Co content, and increased with increasing VC content (Table 4.3). This is expected since the hardness of WC-Co results from the WC. The hardness of WC-67VC-10Co could not be measured with the same load as used for the WC-10Co alloy (i.e. 30 kg load, as per standard for cemented carbides (http://testequipment, 2004)), because the indenter induced cracks in the sample, making it impossible to measure the diagonal of the indentations, compared in Figure 4.5 (for a cracked sample) and Figure 4.6 (for an uncracked sample). The cracking indicated that the resistance of the material to fracture under this load was poor. The embrittlement at the very high VC addition is due to the large size of the (V,W)C grains (Figure 4.3). The grain size of (V,W)C formed from the dissolution of WC in VC, which increased with the VC content (Huang, 2008). A large grain size has been associated with increased brittleness; Luyckx (1996) and Makhele (2000) have indicated that the grain size of the (V,W,Co)C grains must be less than or equal to 2 µm, otherwise WC-VC-Co alloys

become very brittle. Also, refining the starting materials to smaller grain size reduced the grain size of the (V,W,Co)C in the final sintered material to less than the critical value for crack initiation and growth (Whitefield, 2011).

Storms (1967) reported the hardness value of vanadium carbide to be in the range from 2094 $kg.mm^{-2}$ to about 3000 $kg.mm^{-2}$. The hardness found for the mixed carbide in WC-67VC-10Co agrees, within experimental error, with these findings. The hardness of the VC based cemented carbide changed with composition, i.e. as the amount of W in solution changed.

Some of the indentations had pin-cushion shapes (Figure 4.6). Pin-cushioning has been explained by Tabor (1970), who stated that when the indenter sinks into the metal, the material adjacent to the indenter becomes work-hardened relative to the undeformed metal farther away, and then relaxes elastically when the indenter is withdrawn. This gives the pincushion effect illustrated in Figure 5.1.

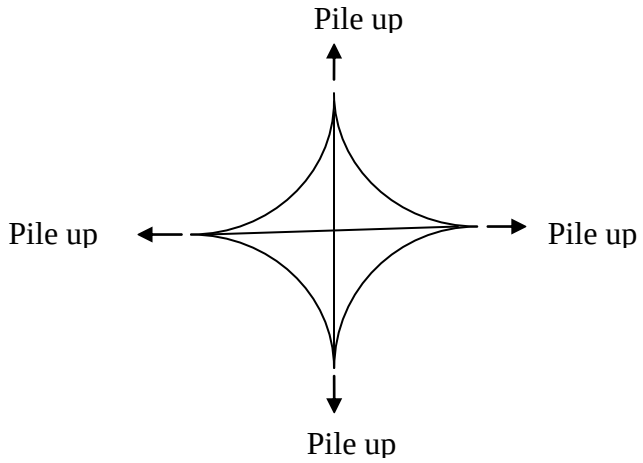


Figure 5.1. Schematic diagram showing the indentation from a pyramidal indenter in a material that work hardens, with arrows representing directions of easy flow (Tabor, 1970).

5.1.3 Magnetic saturation

Magnetic saturation measures the solute content of the cobalt binder and is important for corrosion studies. In plain WC-Co grades, both the tungsten and carbon dissolve in the binder during sintering (Exner 1979). As already noted in Section 3.8, Tillwick and Joffe (1988) have shown that the magnetic saturation of the Co binder decreases with increasing W in solution. Alloys WC-10Co and WC-67VC-10Co essentially had the same magnetic saturation of 195.78 ± 0.12 and 194.91± 0.54 Gauss.cm^3.g^{-1} respectively (Table 4.8). This might imply that the solute content of the binders was similar. As shown in Table 4.5, the solute atoms in binder for the VC specimens also had V in solution, unlike the plain WC-Co grades which had only W in solution. It should be mentioned that carbon was not detected for any of the test specimens.

It can be said therefore, that in this case, magnetic saturation results did not distinguish between the two types of alloys. This could have been expected since the magnetic saturation of Co is, in general, independent of the Co phase. Importantly, it needs to be noted that there is currently no data available on the effect of high amounts of VC on the magnetic saturation of WC-Co except for Whitefield *et al.* (1997, 2000) with 10 wt% VC. The current results appear to suggest that it is the level of solute content, and maybe not necessarily the type of solute atoms that affect the magnetic saturation of the binder.

Generally, magnetic saturation of the binder affects the corrosion response. Mori *et al*. (2003) reported the corrosion resistance to increase with decreasing magnetic saturation, as a result of increasing W in solution in the Co binder. Mori (2003) also found that as the magnetic saturation of WC-Co hardmetals increased, that is with decreasing W content in the Co, the corrosion resistance decreased. The high magnetic saturation of the WC-VC-Co alloys indicated a lower W content in the cobalt binder (Whitefield, 2011). Virtanen *et al*. (2009) clearly observed the monotonous decrease of corrosion current density with decreasing magnetic saturation, which is increasing W content in binder.

5.1.4 Microstructures of specimens

SEM micrographs in the BSE mode for the plain WC-Co grades showed two levels of grey level contrast (Figures 4.1 and 4.2). These are typical of pure WC-Co grades that have been produced with optimized processing parameters (Luyckx, 1997). Areas that appeared with a light grey contrast were WC grains and those with a dark contrast were Co regions.

The SEM micrographs confirmed that the WC grain size was much larger in the WC-Co material than in the WC-VC-Co alloys. This would be expected, since VC inhibits grain growth (Fukatsu *et al.*, 1991; Moyle and Northrop, 1989). The mixed carbide (V,W,Co)C formed as large grains that co-existed with fine WC grains in the WC-10VC-30Co alloy (Figure 4.4). In contrast, no WC grains were observed in the WC-67VC-Co alloy, since all the WC was in solution, either in the VC or in the cobalt. The observations for alloy WC-10VC-30Co are in agreement with Luyckx *et al.* (1996), who showed that the microstructures of all grades of WC-VC-Co with different cobalt percentages exhibited three phases, namely: WC, (V,W)C and Co, while the observations for alloy WC-67VC-10Co are in agreement with Arenas *et al.* (1999).

The weight percentage of tungsten in the binder usually is between 2 and 10 wt% (Exner, 1996), which is consistent with the results in Table 4.5 where tungsten was 8.3 wt% in solution in Co for WC-30Co.

The TEM micrographs (Figures 4.17 - 4.22) showed WC grains with simple shapes. The shapes are due to constrained growth imposed by the basal and prismatic lattice planes of WC (Jia *et al*., 1998; Lay, 2002). The WC grains and the binder were found to contain dislocations, in agreement with Vasel *et al.* (1985); and Jia *et al*. (1998). The dislocations were caused by residual stresses in the WC-Co after sintering, which in turn were caused by differences in the thermal expansion coefficients of WC and Co (Jia *et al*. (1998); Exner (1979)). TEM studies of the WC-30Co revealed a high density of stacking faults in the Co binder (Figure 4.17). The Co phase in the WC-10VC-30Co alloy (Figure 4.18) was expected to have fewer stacking faults, since VC is known to stabilize fcc cobalt. Stacking faults in the Co phase can also be used to determine the ratio of cubic to hexagonal Co using electron diffraction. The WC-30Co hardmetal had many stacking faults, with smaller stacking faults between the longer stacking faults,

whereas with WC-10VC-30Co, there were only parallel sets of stacking faults in the finer grains and they were more clumped with VC.

Unlike the WC grains that had simple shapes, (V,W)C grains had grown extensively in all directions (Figure 4.22). Such growth has been observed by Hashe *et al*., (2007), and occurs because of the absence of crystallographic anisotropy (Exner, 1979).
The short range order obtained for the (V,W,Co)C grains (Figure 4.23) is a carry-over from the structure of VC. The VC is ordinarily non-stoichiometric and tends towards short range order in its non-metal sublattice (Lengauer and Lipatnikov, 1997).

5.1.5 Specimen phase composition

XRD patterns for the four alloys (Figures 4.9 to 4.12) revealed the phases in the specimens to be WC, Co and, for the VC-containing specimens, also (V,W,Co)C. This is in agreement with the SEM and TEM results. The XRD patterns also showed that the Co was present both as hcp and fcc variants. Normally, the additions of VC to WC-Co will lead to the formation of a meta-stable phase called eta (Co_3W_3C), which is detrimental to the alloy's mechanical properties (Luyckx, 1996). This phase was not detected by XRD, SEM or TEM. This could be because of free carbon and free oxygen being removed from the powders before sintering the alloys (Upadhyaya, 1998).

The occurrence of the (V,W,Co)C and not VC, has already been explained to be a consequence of the dissolution of WC in VC (Exner, 1979). The dissolution was extensive, such that in the WC-67VC-10Co alloy, no peaks for WC were observed in its XRD pattern (Figure 4.10), the same as for a sintered 70wt% V_8C_7 – 30wt%WC powder mixture (Huang, 2005).

The occurrence of Co as both hcp and fcc (Table 4.11) is in line with literature (Exner, 1979; Krawitz *et al*., 1985). Cobalt is hcp at room temperature and fcc above about 400ºC. However, the allotropic transformation on cooling is usually sluggish, resulting in the co-existence of the two phases at room temperature (Krawitz *et al*., 1985). The transformation is slowed further by solute atoms. The crystal lattice parameters obtained by XRD for the allotropes (Table 4.10) were larger than those of reference samples where the lattice parameters for hcp Co were *a* =

0.2507 and c = 0.4070 nm and a = 0.3545 nm for fcc Co (Ram, 2001). This expansion is believed to be caused by the presence of solute atoms in the Co.

The lattice parameters of WC obtained by XRD (Table 4.10) were larger than those of single crystal WC which were a = 0.2907, c = 0.2829 nm (Nabarro *et al*., 2006). This variance occurred because the WC in WC-Co alloys was under compressive residual stresses and Co in tension, as a result of the cooling during sintering (Mari *et al*., 1996).

The lattice parameters obtained from the XRD measurements for V_8C_7 (Table 4.10) were slightly larger than those of Huang and co-workers (2005). The latter, working on (V,W)C obtained from V_8C_7 and WC diffusion couples, found that the lattice parameter varied from 0.8323 to 0.8405 nm with increasing WC content up to 60 wt%. The larger values obtained in the current study are likely to have been caused by the tensile stress imposed on the grains during cooling after sintering.

5.1.6 Electrochemical corrosion tests

The potentiodynamic polarization curves (Figures 4.24 and 4.25) indicated pseudopassivity, a slight drop in current density after the maximum current densities were reached, a feature already demonstrated by Human (1994). The pseudopassivity region was found to be 2.4 times longer for the WC-10Co alloy than for the WC-67VC-Co material. This region spanned potentials between 350 mV and 950 mV for the WC-10Co alloy, and between 500 mV and 750 mV for WC-67VC-10Co alloy. Since the corrosion potential, E_{corr}, is a measure of the reactivity of a material (Jones, 1996), and a high negative potential indicates that the driving force of the material to dissolve is high, the present results indicate that the WC-VC-Co alloy was rather more active than the WC-Co alloy. The rate of corrosion is given by the corrosion current density, i_{corr}; the higher the current density, the higher the corrosion rate. At first glance, the i_{corr} values do not appear to show any real difference between the two alloys, but the true trend is most likely masked by the large errors associated with the readings.

Concurrent work by Potgieter *et al.* (2011) varied the amount of ruthenium (Ru) in plain WC-10Co and in the same alloy with 0.4 wt% VC. As the ruthenium content was increased, the

corrosion resistance of WC-10Co increased proportionally, although the 0.4 wt% VC sample showed slower open circuit potential compared to the WC-10Co alloy. Figure 2.4 shows all polarization curves in 1M H_2SO_4 had the same typical active-passive transition behavior at varying voltages, while Figures 4.24 and 4.25 showed pseudopassivity at different voltages. The work of Human (1994) and Human *et al*. (1998) did not exhibit the same behavior in the same solution, but had direct passivation. Small additions of ruthenium were used in stainless steel for corrosion resistance improvements by Potgieter *et al*. (1993). Broccardo (2003) reported no corrosion improvements at low cobalt content (10 wt% Co) with or without VC addition and as was observed in current study, although VC addition lowered the corrosion rate at high cobalt contents. However, Potgieter *et al*. (2011) reported that a difference was observed at the same cobalt content with addition of small amounts of ruthenium (0.4 wt% to 2 wt%).

The SEM micrographs confirmed that the WC grain size was much larger in the WC-Co material than in the WC-VC-Co alloys and Tomlinson and Ayerst (1989) reported that an increase in the WC grain size results in decreasing corrosion resistance in 0.01 M H_2SO_4. VC refines grain size of WC-Co alloy; one might make assumption that the smaller WC grain size, the better the corrosion resistance. Thus, this contradicts Human and Exner (1994, 1998); showing that grain size does not affect the corrosion rate in H_2SO_4. The role of grain size on corrosion has also been noted by Vasel *et al.* (2009) which could be difficult to justify, because the grades used also had grain refiners like Cr_2C_3, which are known to improve corrosion resistance. Thus, it can be argued that the observations could not necessarily be attributed to the effect of grain size alone. In general, it is difficult to compare observations by different researchers, because the test specimens were different and the different researchers did not characterize their specimens to the same degree. However, generally, there appears to be agreement that W in Co alters corrosion behavior, Human (1994).

Figure 4.28 and 4.30, confirms the Human (1994) observation that of corrosion of WC-Co hardmetals occurs mainly by the oxidation of the cobalt binder phase, as both specimens were leached of the Co binder. It emphasized the overall corrosive failure of the hardmetal occurred by the selective dissolution of the binder phase, leaving behind a WC or mixed carbide skeleton.

Figure 4.30 showed the corrosion by-product which was not analyzed, but was expected to be hydrated WO_3, and in the high VC content grade, also some $VOSO_4.H_2O$ (Konadu *et al.*, 2010).

5.2 Hypotheses

The aim of this investigation was to determine the causes of the differences in the corrosion behaviour of WC-Co and WC-VC-Co alloys of equal Co mass fraction. The hypotheses made were that the possible causes were:

1. There is a difference in the composition of the Co-based binders (since the binder is mainly responsible for the corrosion of these alloys),
2. There is a difference in the fcc-Co/hcp-Co ratio (since it has been shown that fcc-Co is more corrosion resistant that hcp-Co (Human, 1994)), and
3. There is a difference in the Co surface fraction exposed to corrosion in alloys of equal mass fraction.

5.2.1 Composition differences in the binder

The first hypothesis was that the composition of the binder should be different in the WC-Co and WC-VC-Co alloys, and this would affect the corrosion resistance.

In order to verify the difference in the composition of the binder phase, it was necessary to determine the W and V content in the binder of the WC-VC-Co alloy, and the W content of the binder of the WC-Co alloy. If the total atomic percentage of the solute was different, the corrosion rate also would be expected to be different, as shown for example by Mori *et al.* (2001, 2003). In order to prove or disprove this hypothesis, SEM-EDX and magnetic balance measurements were utilized.

In Table 4.5, even though there are only entries for three of the four alloys under the Co binder column, the results show that the composition of the binder in the WC-Co and WC-VC-Co alloys was different. The binder in WC-Co grades was a solid solution of W in Co, while in the WC-VC-Co alloys, the binder was a solid solution of W and V in Co. In general, determining the binder composition was hampered by the fact that the Co regions in some of the alloys were

quite small, so yielding significant errors. Within the errors, the total percentage of solute was the same for the three alloys.

The differences in the binder composition did not affect the potentiodynamic anodisation behavior of the specimens. Figures 4.25 and 4.26 showed that all the specimens exhibited a pseudo-passive behavior, this being greater for the WC-Co alloys. The binder composition also did not appear, within experimental error, to have influenced the corrosion current densities at the free corrosion potential (Table 4.13). The depths of the corroded layers indicate that introducing VC, and therefore changing the binder composition, increases the depth of the corroded layer, but that this difference decreases as the VC content increases.

5.2.2 Difference in the fcc-Co/hcp-Co ratio

The second hypothesis was that the difference in corrosion behaviour between the WC-Co and WC-VC-Co alloys was caused by a higher fcc/hcp Co ratio in the alloys with VC, since it has been reported that cubic Co is more corrosion resistant than hexagonal cobalt (Human, 1994).

XRD was used to try to prove or disprove this hypothesis. TEM studies were also employed to attempt to determine the stacking fault densities in the two binders, but this proved inconclusive, although the appearances were different (Figures 4.17 and 4.18).

Rietveld analysis of XRD patterns revealed that all the test specimens had cobalt present in both the fcc and hcp forms. Table 4.9 shows the amount present of the two forms in the low (10 wt%) and high (30 wt%) cobalt content alloys. Table 4.11, using data from Table 4.9, indicates that the presence of VC enhanced the fcc Co/hcp Co ratio, especially at higher Co concentrations. At the 10 wt% Co level, the addition of VC the ratio slightly increased by 3%. However, as already mentioned, the improvement was highest at 30 wt% Co, where a 133% increase was achieved.

Unfortunately, the results obtained for corrosion current densities for the 10 wt% Co specimens (Table 4.13) could not yield any difference between the two alloys due to large experimental errors. When the errors were included, the spread of possible values was large, especially for the WC-Co alloy, therefore both ranges overlapped and no difference could be detected. Thus, the

hypothesis did not hold in the case of the immersion corrosion tests for any of the alloy combinations, with or without VC containing the same percentage Co. The depth of the corrosion layer was always larger for the alloy containing VC, even when quoted experimental errors were taken into account. The high experimental errors were due to the corroded depths being irregular (Figure 4.38).

5.2.3 Difference in the Co surface fraction exposed to corrosion

The third hypothesis was that the lower corrosion rate of the WC-VC-Co alloys observed in literature was due to the fact that VC-containing materials have less Co volume percentage for equal Co weight percentage.

The Co fractions in the VC-containing samples were slightly less than in the equivalent WC-Co alloys (Table 4.4). However, within experimental error, the corrosion current densities were identical (Table 4.13). Since the corrosion current density was proportional to the corrosion rate, it follows that the corrosion rates of the WC-10Co and WC-67VC-10Co alloys were similar (Table 4.13). This confirms the results of Broccardo (2003) in that there was no difference between the corrosion rate of WC-Co and WC-10VC-Co alloys at low cobalt contents (10 wt% Co). The expectation from Human (1994) and Human *et al*. (1998) was that the higher the Co surface fraction exposed, the higher the corrosion current densities, which was not the case in the current study, because the corrosion current densities overlapped within experimental error (Table 4.13).

Electrochemical tests on high cobalt content alloys were not undertaken in this project due to a lack of samples. However, from immersion corrosion testing, the VC grade, with a lower exposed Co fraction, had a larger mean corrosion depth than the plain WC-30Co grade (Table 4.14), which had a higher exposed Co fraction, indicating that the hypothesis was not valid.

From the immersion tests, the corrosion depth of the WC-10VC-Co alloys was found to decrease with increasing Co content, in agreement with the results from electrochemical corrosion data reported by Broccardo (2003). In the case of WC-Co alloys, the trend was similar, although much less pronounced, but this does not agree with the well known decrease in corrosion

resistance with increasing Co content (Human *et al*., 1998). For a given Co content, the corrosion depths for WC-Co alloys were lower than for WC-VC-Co alloys, which is consistent with the results from electrochemical corrosion tests reported by Broccardo (2003). While both the current results and Broccardo's results (2003) showed a decrease in corrosion depth with increasing Co in the 10VC alloys, an expected steady decrease was not observed. This, however, may be due to the material loss.

The failure of the three hypotheses to account for Broccardo's results (2003) that the corrosion resistance of WC-VC-Co is better than that of WC-Co raises the possibility that Broccardo's conclusions (2003) may possibly be incorrect.

Chapter 6

Conclusions

The present study sought to explain purported differences in the corrosion resistance of WC-Co and WC-VC-Co alloys against three possible hypotheses:

1. There is a difference in the composition of the Co-based binders (since the binder is mainly responsible for the corrosion of these alloys),
2. There is a difference in the fcc-Co/hcp-Co ratio (since it has been shown that fcc-Co is more corrosion resistant that hcp-Co (Human, 1994), and
3. There is a difference in the Co surface fraction exposed to corrosion in alloys of equal mass fraction.

In order to achieve this, a comprehensive characterization of the alloys was required.

The introduction of large amounts of VC in WC-Co was found to lower the density of the resulting component compared to the plain WC-Co grade, since the density of VC is nearly a third of the density of WC (Luyckx, 1994). The hardness of the specimens was found to decrease with higher Co content, and increase with increasing VC content. This is expected as the VC inhibits the grain size of WC, and the smaller the grain size, the harder the material. The SEM micrographs confirmed that the WC grain size was much larger in the WC-Co material than in the WC-VC-Co alloys. This would also be expected, since VC inhibits grain growth (Fukatsu *et al.* 1991; Moyle and Northrop, 1989). Whitefield, (2011) has noted that the hardness could be increased by optimizing the microstructure and decreasing the grain size of the (V,W,Co)C phase.

The WC-10Co, WC-67VC-10Co, WC-30Co and WC-10VC-30Co alloys all contained the WC, Co phases, while the alloys with VC also had the (V,W,Co)C phase present. XRD revealed that the Co was present in both the fcc and hcp variants.

Magnetic saturation results could not distinguish between the two types of alloys. This might have been expected since the magnetic saturation of Co is, in general, independent of the phase of the Co.

The effect of binder composition was assessed. Differences in the binder composition did not affect the potentiodynamic anodisation behavior of the specimens and the corrosion current densities at the free corrosion potential. Only the depths of the corroded layers indicated that introducing VC, and therefore changing the binder composition, increased the depth of the corroded layer.

The effect of the fcc Co/hcp Co ratio on corrosion current densities was inconclusive due to the significantly large experimental errors. However, the immersion corrosion tests yielded a greater depth of corrosion for VC-containing alloys compared to their equivalents not containing VC. Since the addition of VC was found to increase to increase the corrosion depth, and it has been shown that the fcc/hcp Co ratio increases with VC addition, it could be postulated that an increased fcc/hcp Co ratio reduces the corrosion resistance, a result in disagreement with Human (1994). Even though there is considerable scatter in the VC alloy corrosion depth measurements, there does appear, at least, to be a markedly significant difference between the WC-10VC-10Co alloy and those with increasing Co content.

The third hypothesis was based on the effect of the VC additions on the Co fraction. This hypothesis also fails, because neither does reducing the Co volume fraction result in a reduction in the corrosion density, nor does it reduce the thickness of the corroded layer.

The failure of the three hypotheses to account for Broccardo's results that the corrosion resistance of WC-VC-Co is better than that of WC-Co raises the possibility that Broccardo's conclusions were incorrect, as the results were afflicted with large scatter.

In addition, it must be recognized that the possibility exists that there may have been some loss of corroded layers in a difficult experimental environment, or by handling.

References

Aguzzoli, C., Figueroa, C. A., de Souza, F. S., Spinelli, A. and Baumvol, I.J.R. Corrosion and nanomechanical properties of vanadium carbide thin film coatings of tool steel, *Surface & Coatings Technology*, **206** (2012) 2725–2731.

Alekseev, V. I., Yusupov, V. S., Perkas, M. M. and Lazarenko, G. Yu. On the nature of metal passivation during cathode depolarization by oxygen dissolved in an electrolyte, *Russian Metallurgy*, **1** (2012) 48–54.

Arenas, F., de Arenas, I.B., Ochoa, J. and Cho, S.-A. Influence of VC on the microstructure and mechanical properties of WC – Co sintered cemented carbides, *Int. J. Refract. Metals & Hard Mater*. **17** (1999) 91-97.

ASTM G5-94: Standard Reference Test Method for Making Potentiostatic and Potentiodynamic Anodic Polarization Measurements. ASTM Book of Standards (2000).

Balke, P. The composition and microstructure of the WC-VC-Co hardmetal. *Technical Report*, University of Groningen & University of the Witwatersrand (1997).

Bhagga Fazluddin, S., Koursaris, A., Ringas, C. and Cowie, K. Corrosion behavior of vanadium carbide produced by a thermal diffusion process. *Mater. & Manuf. Proc.* **10-2**(1995) 159-165.

Broccardo, S., Sephton, M. and Luyckx, S.B. The effect of vanadium carbide (VC) additions on the corrosion of WC-Co. 15th International Corrosion Conference (ICC), Granada, Spain, September 2002, paper 787.

Broccardo, S. An investigation into the corrosion resistance of WC-VC-Co hardmetals. *MSc dissertation*, University of the Witwatersrand (2003).

Brookes K.J.A. World Directory and Handbook of Hardmetals and Hard Materials, 5th Edn., International Carbide Data, East Barnet, Hertfordshire, United Kingdom (1992).

Brookes K.J.A. Hardmetal and other Hard Materials, 3rd Edn., International Carbide Data (1998).

Chikazumi, S. Physics of Ferromagnetism, Oxford University Press, New York, USA, Appendix 4, (1997).

Edington, J.W. Practical Electron Microscopy in Materials Science, Techbooks, Herdon, Virginia, USA, (1976) p. 290.

Exner, H.E. Physical and chemical nature of cemented carbides. *Int. Metals Rev.* **243** (1979) 149-173.

Fourie, J.T. A theory of surface-originating contamination and a method for its elimination, Scanning Electron Microscopy/1979/II, SEM Inc., AMF O'Hare, USA, (1979) pp. 87-102.

Fukatsu, T., Kobori, K. and Ueki, M. Micro-grained cemented carbide with high strength, *Refract. Metals & Hard Maters*. **10** (1991) 57-60.

Gil, L. E., Liscano, S., Goudeau, P., Le Bourhis, E., Puchi-Cabrera E. S., and Staia, M. H. Effect of TiAlN PVD coatings on corrosion performance of WC–6%Co, Surface Eng., 000, (2008) 1-5.

Haglund, S. and Agren, J.W. content in Co binder during sintering of WC-Co, *Acta Mater*. **46** (1998) 2801-2807.

Hashe, N.G., Neethling J.H., Berndt, P.R., Andrén, H. and Norgren, S. A comparison of the microstructures of WC–VC–TiC–Co and WC–VC–Co cemented carbides, *Int. J. Refract. Metals & Hard Mater.* **25** (2007) 207-213.

Hellsing, M. High resolution microanalysis, developments and applications to cemented carbides, *PhD thesis*, Department of Physics, Chalmers University of Technology, Göthenberg (1985).

Hellsing, M. High resolution microanalysis of binder phase in as-sintered WC-Co cemented carbides. *Mater. Sci. Technol*. **4** (1988) 824-829.

Hermann, M. Private Communication, Fraunhofer Institute, Dresden, Germany, (2004).

Huang, S.G., Vanmeensel, K., Van der Biest, O. and Vleugels, J. Binderless WC and WC-VC materials obtained by pulsed electric current sintering, *Int. J. Refract. Metals & Hard Mater*. **26**, (1) (2008) 41-47.

Huang, S.G., Vleugels J., Lin Li., and Van der Biest, O. Experimental investigation and thermodynamic assessment of the V-W-C system, J. Alloys and Compounds **395** (2005) 68-74.

Human, A.M., Northrop, I.T., Luyckx, S.B. and James, M.N. A comparison between cemented carbides containing cobalt- and nickel-based binders. *J. Hard Mater.* **2** (1991) 245-256.

Human, A.M. The corrosion of tungsten carbide based cemented carbides. *PhD thesis*, Technical University of Darmstadt, 1994.

Human, A.M. and Exner, H.E. Electrochemical behaviour of tungsten-carbide hardmetals. *Mater. Sci. & Eng.* ***A*209** (1996) 180-191.

Human, A.M. and Exner, H.E. Relationship between electrochemical behaviour and in-service corrosion of WC based cemented carbides. *Int. J. Refract. Metals & Hard Mater*. **15** (1997) 65-71.

Human, A.M., Roebuck, B. and Exner, H.E. Electrochemical polarisation and corrosion behaviour of cobalt and Co(W,C) alloys in 1N sulphuric acid. *Mater. Sci. & Eng.* **241** (1998) 202-210.

Jia, K., Fischer, T.E., and Gallois, B. Microstructure, hardness and toughness of nanostructured and conventional WC-Co composites, *Nanostructured Materials* **10** (5) (1998) 875-891.

Jones, D. Principles and Prevention of Corrosion, 2nd Edn., Prentice-Hall, New Jersey, USA. (1996).

Krawitz, A.D. The use of X-ray stress analysis for WC-based cermets. *Mater. Sci. & Eng.* **75** (1985) 29-36.

Kursawe, S., Pott, Ph., Sockel, H.G., Heinrich, W. and Wolf, M. On the influence of binder content and binder composition on the mechanical properties of hardmetals, *Int. J. Refract. Metals & Hard Mater*. **19** (2001) 335-340.

Lee, H.R., Kim, D.J, Hwang, N.M. and Kim, D.-Y. Role of vanadium carbide additive during sintering of WC-Co: Mechanism of grain growth inhibition. *Amer. Cer. Soc*. **86** (2003) 152-154.

Lipatnikov, V. N., Lengauer, W., Ettmayer, P., Keil, E., Groboth, G. and Kny, E. Effects of vacancy ordering on structure and properties of vanadium carbide, J. *Alloys and Compounds*, **261** (1997) 192-197.

Luyckx, S. (V,W)C-based hardmetal and its resistance to wear and erosion. *Proc. Powder. Metall. World Congress PM '94*, Paris, 6-9 June, **1** (1994) 169-171.

Luyckx, S. Vanadium carbide in hardmetals, *XVth CMMI Congress*, Johannesburg, SAIMM, **2,** (1994) 11-13.

Luyckx, S., Cornish, L., Osborne, C. and Whitefield, D. Fine grained WC-VC-Co hardmetal, *Powder. Met*. **39** (1996) 210-212.

Luyckx, S., Cornish, L. and Osborne, C. On the preparation of fine V_8C_7-WC and V_4C_3-WC Powders, *Int. J. Refract. Metals & Hard Mater*. **15** (1997) 163-168.

Luyckx, S. and Love, A. The relationship between the abrasion resistance and the hardness of WC-Co alloys, SAIMM, (2004) 579-582.

Machio, C. N., Konadu, D. S., J. H. Potgieter, J. H., Potgieter-Vermaak, S. and Van der Merwe, J. Corrosion of WC-VC-Co hardmetal in neutral chloride containing media, IRSN Corrosion, **2013**, (2012).

Makhele, L.Z. The relationship between the hardness, grain size and mean free path in WC-Co, *MSc dissertation*, University of the Witwatersrand, South Africa, (2000) pp. 6-7.

Manyatsa, R., Microstructure analysis and corrosion behaviour of WC-VC-Co materials. *Technical Report*, University of the Witwatersrand, 2000.

Mari, D., Krawitz, A.D., Richardson, J.W. and Benoit, W. Residual stress in WC-Co measured by neutron diffraction, *Mater. Sci & Eng.* **A209** (1996) 197- 205.

Mori, G., Zitter, H., Lackner, A. and Schretter, M. Influencing the corrosion resistance of cemented carbides by addition of Cr_3C_2, TiC and TaC. *Int. Plansee Seminar*, **2** (2001) 222-236.

Mori, G. and Sutthiruangwong, S. Corrosion of Co-based cemented carbides in acidic solutions, *Int. J. Refract. Metals & Hard Mater.* **21** (2003) 135-145.

Moyle, D.R. and Northrop, R.F., Physical and microstructural effects of increasing sintering temperature and VC content on WC-Co hardmetal alloys, *Int. Plansee Seminar*, **12** (1989) 97-112.

Nabarro, F.R.N., Luyckx, S. B. and Waghmare, U.V. Slip in tungsten monocarbide: I. Some experimental observations, *Mater. Sci & Eng.* **A483-484** (2008) 139-142.

Obbard, E.G., Luyckx. S., Hamar-Thibault. S. and Allibert. C.H. Determination of the composition range suitable to the formation of WC-$(V,W)C_x$-Co materials. *Int. J. Refract. Metals & Hard Mater.* **19** (2001) 349-357.

Potgieter, J.H., Thanjekwayo, N., Olumbabi, P., Maledi, N. and Potgieter-Vermaak, S.S. Influence of Ru additions on the corrosion behavior of WC-Co cemented carbide alloys in sulfuric acid. *Int. J. Refract. Metals & Hard Mater.* **29** (2011) 478-487.

Ram, S. Allotropic phase transformations in hcp, fcc and bcc metastable structures in Co-nanoparticles, *Mater. Sci. & Eng.* **A304-306** (2001) 923-927.

Roebuck, B. and Almond, E.A. The influence of composition, phase transformation and varying the relative fcc and hcp phase contents on the properties of dilute Co-W-C alloys. *Mater. Sci. & Eng.* **66** (1984) 179-194.

Sarin, V.J. and Johannesson, J. On the deformation of WC-Co cemented carbides. *Metal Sci*. **9** (1975) 472-475.

Schollenberger, H.J. A comparison of the corrosion resistance of VC-WC-Co, TiC-TaC-WC-Co and WC-Co hard metals of equal cobalt content, *Technical Report*, University of the Witwatersrand, South Africa (1991).

Schuhmacher, G. and Ostermann, G. Hard metals in modern technology. *Cobalt & Cobalt Abstracts*, **4**, (1973) 77-92.

Schlumberger Electronics Ltd, 1286 Electrochemical Interface, Operating Manual Solartron Instruments, (1985).

Shing T.L., Luyckx S., Northrop I.T. and Wolff, I. The effect of ruthenium additions on the hardness, toughness and grain size of WC-Co, *Int. J. Refract. Metals & Hard Mater.* **19** (2001) 41-44.

Simard, S., Arsenault, K., Laul, and Dorfman, M.R. Performance of HVOF-sprayed carbide coatings in aqueous corrosive environments, Thermal Spray: Surface Engineering via Applied Research, *Proc. 1st ITSC*, Montreal, Canada, 8-11 May, 2000, C C Berndt (Ed.), *ASM Int.* (Pub), 983-990.

Spiegler. R., Schmauder S. and Exner, H.E. Finite element modelling of the thermal residual stress distribution in a WC10wt'X, Co alloy, *J. Hard Mater.*, **3** (1992) 143-151.

Spriggs, G.E., A history of fine grained hardmetal, *Int. J. Refract. Metals & Hard Mater.* **13** (1995) 241-255.

Stern, M., Surface area relationships in polarization and corrosion, *Corrosion* **14** (1958), 329-332.

Storms, E.K. The Refractory Metal Carbides, Academic Press, New York (1967).

Stratton. R.P and Kitchingman, W.J. Stacking fault densities in hexagonal gold alloys, *Brit. J. Appl. Phys.* **17** (1966) 1039-1042.

Tabor, D. The hardness of solids, *Rev. Phys. Technol*. **1** (1970) 145- 179.

Tillwick, D.L. and Joffe, I. Magnetic properties of Co-W alloys in relation to sintered WC-Co composites. *Scripta Metall*. **7** (1973) 479-484.

Tomlinson, W.J. and Linzell, C.R. Anodic polarization and corrosion of chemical carbides with cobalt and nickel binders, *J. Mater. Sci.* **23** (1988) 914-918.

Tomlinson, W.J. and Ayerst, N.J. Anodic polarization and corrosion of WC-Co hardmetals containing small amounts of Cr_2C_3 and/or VC. *J. Mater. Sci.* **24** (1989) 2348-2354.

Upadhyaya, G.S., Cemented Tungsten Carbides: Production, Properties, and Testing, Noyes Publications, Westwood, New Jersey, USA (1998).

Van Vlack, L.H. Elements of Materials Science and Engineering, 6th Edn, University of Michigan, Addison-Wesley Pub. Co., Reading, Massachusetts, USA (1989) 62-74.

Vasel, C.H., Krawitz, A.D., Drake, E.F. and Kenik, E.A. Binder deformation in WC-Co, Ni cemented carbide composites, *Metall. Trans.* **16A**, (1985) 2309-2317.

Virtanen, S., Lynch, R., and Kellner, F.J.J. Effect of WC grain size on the corrosion behavior of WC-Co hardmetals in alkaline solutions, *Int. J. Refract. Metals & Hard Mater.* **27** (2009) 806-812.

Virtanen, S., Lynch, R., and Kellner, F.J.J. Influence of Ca ions and temperature on the corrosion behavior of WC-Co hardmetals in alkaline solutions, *Int. J. Refract. Metals & Hard Mater.* **28** (2009) 370-376.

Votava, E. The phase transformation in thin cobalt films, *J. Inst. Metals*, **90** (1961) 129-132.

Whitefield, D.J., Luyckx, S.B., Witcomb, M.J., and Cornish, L.A. Microstructure and properties of fine grained WC-VC-Co hardmetal with cobalt content ranging from 10 to 15 wt%, *Proc. Int. Plansee Seminar* **2** (1997).

Whitefield, D.J. The optimization and evaluation of VC-WC-Co hardmetals, *PhD thesis*, University of the Witwatersrand (2011).

Witcomb, M.J., Westers, A.R. and Luyckx, S. Characterisation of phases in a VC-WC-Co hardmetal, *Proc. Microsc. Soc. South. Afr.* **27** (1997) 28.

Zinyana, J., Broccardo, S., Hamar-Thibault. S., Cornish, L.A., Witcomb, M.J., Allibert, C.H. and Luyckx, S. Effect of composition on the (V,W)C constitution in V-W-C-Co alloys, *Int. Plansee Seminar*, **4** (2000) 291-298.

http://testequipment.globalspec.com/LearnMore/Labware_Test_Measurement/Product_Material_Testing /Hardness_Testers, 2004.

http://www.chem.ox.ac.uk/icl/heyes/structure_of_solids/lecture1/lec1.html.

(Accessed June 2012).

Appendix A

X-ray diffraction analysis

Table A.1. XRD data for the WC-10Co alloy giving the d-spacings of each peak in the pattern. (Figure 4.9)

Pos. (°2 theta)	Height (counts)	FWHM (°2 theta)	d-spacing (nm)	Rel. Int. (%)	Tip width (°2 theta)	Matched by
31.66	414.95	0.1200	0.2824	36.65	0.1000	00-025-1047
35.79	1132.25	0.0600	0.2507	100.00	0.0500	00-025-1047
41.90	2.81	1.1520	0.2154	0.25	0.9600	00-015-0806
44.10	28.84	0.1920	0.2052	2.55	0.1600	00-015-0806
46.27	12.31	0.2880	0.1961	1.09	0.2400	00-015-0806
48.42	1064.55	0.1080	0.1879	94.02	0.0900	00-025-1047
64.16	214.10	0.1680	0.1454	18.91	0.1400	00-025-1047
65.88	54.68	0.1200	0.1417	4.83	0.1000	00-025-1047
73.24	177.84	0.2160	0.1291	15.71	0.1800	00-025-1047
75.58	111.42	0.1200	0.1257	9.84	0.1000	00-025-1047
77.23	176.25	0.1920	0.1234	15.57	0.1600	00-025-1047

78.22	44.23	0.0120	0.1221	3.91	0.0100	00-025-1047
84.16	145.55	0.1920	0.1149	12.85	0.1600	00-025-1047
91.50	2.89	0.7680	0.1075	0.26	0.6400	00-025-1047
93.95	4.09	0.7680	0.1054	0.36	0.6400	00-025-1047
98.83	82.82	0.3360	0.1014	7.31	0.2800	00-025-1047

Table A.1.1. Identified patterns list for the WC-10Co alloy (Figure 4.9). (* = All visible or noted peaks on the XRD pattern.)

Visible	Reference code	Compound Name	Displacement (°2 theta)	Scale factor	Chemical formula
*	00-025-1047	Tungsten carbide	0.000	0.607	WC
*	00-015-0806	Cobalt	0.000	0.708	Co
*	01-089-4308	Cobalt	0.000	0.254	Co

Table A.2. XRD data for the WC-67VC-10Co alloy giving the d-spacings of each peak in the pattern (Figure 4.10).

Pos. (°2 theta)	Height (counts)	FWHM (°2 theta)	d-spacing (nm)	Rel. Int. (%)	Tip width (°2 theta)	Matched by
37.3773	354.91	0.0840	0.2404	94.09	0.0700	01-073-0476
37.4728	364.13	0.0720	0.2398	96.53	0.0600	01-073-0476
43.4899	377.22	0.1080	0.2079	100.00	0.0900	01-073-0476
44.3160	58.08	0.1920	0.2042	15.40	0.1600	00-015-0806
59.5851	6.03	0.2880	0.1550	1.60	0.2400	00-035-0786
62.9693	234.45	0.1200	0.1475	62.15	0.1000	01-073-0476

75.3918	87.35	0.1440	0.1260	23.16	0.1200	01-073-0476
75.7172	27.73	0.1440	0.1255	7.35	0.1200	01-073-0476
79.4106	29.57	0.1920	0.1206	7.84	0.1600	01-073-0476
91.9175	15.35	0.3840	0.1072	4.07	0.3200	01-073-0476
95.1187	26.19	0.3360	0.1044	6.94	0.2800	01-073-0476
97.2244	5.05	0.5760	0.1027	1.34	0.4800	00-035-0786

Table A.2.1. Identified patterns list for the WC-67VC-10Co alloy (Figure 4.10). (* = All visible or noted peaks on the XRD pattern.)

Visible	**Reference code**	**Compound Name**	**Displacement (°2 theta)**	**Scale factor**	**Chemical formula**
*	00-035-0786	Vanadium carbide	0.000	0.572	V_8C_7
*	00-015-0806	Cobalt	0.000	0.067	Co
*	01-073-0476	Vanadium carbide	0.000	0.606	VC

Table A.3. XRD data for the WC-30Co alloy giving the d-spacings of each peak in the pattern, (Figure 4.11).

Pos. (°2 theta)	**Height (counts)**	**FWHM (°2 theta)**	**d-spacing (nm)**	**Rel. Int. (%)**	**Tip width (°2 theta)**	**Matched by**
31.5554	85.34	0.2880	0.2833	22.82	0.2400	00-025-1047
35.7463	374.01	0.2880	0.2510	100.00	0.2400	00-025-1047
44.3644	28.40	0.7680	0.2040	7.59	0.6400	00-015-0806 01-089-4308
48.3400	247.82	0.2880	0.1881	66.26	0.2400	00-025-1047
64.0642	37.85	0.3840	0.1452	10.12	0.3200	00-025-1047
73.1558	66.54	0.3840	0.1293	17.79	0.3200	00-025-1047

75.5595	40.59	0.3840	0.1257	10.85	0.3200	00-025-1047
77.2549	37.26	0.6720	0.1234	9.96	0.5600	00-025-1047
84.0901	26.87	0.5760	0.1151	7.18	0.4800	00-025-1047

Table A.3.1. Identified patterns list for the WC-30Co alloy (Figure 4.11). (* = All visible or noted peaks on the XRD pattern.)

Visible	Reference code	Compound Name	Displacement (°2 theta)	Scale factor	Chemical formula
*	00-025-1047	Tungsten carbide	0.000	0.607	WC
*	00-015-0806	Cobalt	0.000	0.708	Co
*	01-089-4308	Cobalt	0.000	0.254	Co

Table A.4. XRD data for the WC-10VC-30Co alloy giving the d-values of each peak in the pattern (Figure 4.12).

Pos. (°2 theta)	Height (counts)	FWHM (°2 theta)	d-spacing (nm)	Rel. Int. (%)	Tip width (°2 theta)	Matched by
29.5451	1183.74	0.1440	0.3021	100.00	0.1200	00-051-0939
31.5587	52.45	0.2880	0.2833	4.43	0.2400	00-051-0939
35.6894	82.65	0.2880	0.2514	6.98	0.2400	00-051-0939
37.0294	21.25	0.2880	0.2426	1.79	0.2400	01-089-1096
39.5457	115.78	0.1680	0.2277	9.78	0.1400	00-051-0939
43.2802	101.02	0.1920	0.2089	8.53	0.1600	00-051-0939
47.6052	162.16	0.2400	0.1909	13.70	0.2000	01-089-4308
48.6059	162.86	0.1680	0.1872	13.76	0.1400	01-089-1096
57.4916	47.95	0.1920	0.1602	4.05	0.1600	01-089-1096
60.8081	19.41	0.5760	0.1522	1.64	0.4800	01-089-1096
64.7755	19.23	0.2880	0.1438	1.62	0.2400	00-051-0939
65.7055	36.26	0.2400	0.1420	3.06	0.2000	00-051-0939
70.3378	12.73	0.2880	0.1337	1.08	0.2400	00-051-0939
72.9911	26.58	0.4800	0.1295	2.25	0.4000	00-051-0939

77.2759	23.72	0.2880	0.1234	2.00	0.2400	00-051-0939
81.6438	9.04	0.5760	0.1178	0.76	0.4800	01-089-1096
83.9259	16.77	0.5760	0.1152	1.42	0.4800	00-051-0939
95.0187	11.14	0.7680	0.1045	0.94	0.6400	00-051-0939

Table A.4.1. Identified patterns list for the WC-10VC-30Co alloy (Figure 4.12). (* = All visible or noted peaks on the XRD pattern.)

Visible	**Reference code**	**Compound Name**	**Displacement (°2 theta)**	**Scale factor**	**Chemical formula**
*	00-051-0939	Tungsten carbide	0.000	0.073	WC
*	01-089-4308	Cobalt	0.000	0.027	Co
*	01-089-1096	Vanadium carbide	0.000	0.073	V_8C_7

Appendix B

1. Publications from this work

CHARACTERISATION OF THE (V,W,Co)C PHASE IN A WC-VC-Co HARDMETAL

T. T. Sebeya[1, 2], M. J. Witcomb[2], M. Sephton[1] and S. Luyckx[1]

[1]School of Process and Materials Engineering, University of the Witwatersrand, Johannesburg
[2] Electron Microscope Unit, University of the Witwatersrand, Johannesburg

It has been found that the corrosion resistance of WC-VC-Co hardmetal decreases with increasing cobalt content, while the corrosion resistance of conventional WC-Co hardmetal increases with increasing cobalt content.[1] Since it was expected that both materials would behave in a similar way, a study was initiated to determine the reason for this difference and, in particular, to explain the dramatic difference between the corrosion resistance of WC-VC-Co and WC-Co alloys at high cobalt contents. The grades used in the latter case were WC-10VC-30Co and WC-30Co where the compositions refer to the starting powders and not to the final phases formed during the preparation of the materials.

The work reported here focuses on the initial results obtained for the (V,W,Co)C phase in WC-10VC-30Co.

Characterization involved the determination of the composition and microstructure of both materials and phases by scanning (SEM) and transmission (TEM) electron microscopy, energy dispersive X-ray analysis (EDS) and X-ray diffraction (XRD).

XRD studies indicated the presence of three phases in the WC-10VC-30Co material: WC, (V,W,Co)C and Co. This is in contrast to the WC-30Co alloy where only two phases, WC and Co, were found. Cobalt was found to be present in both fcc and hcp forms in both alloys. However, the fcc/hcp ratio was higher in the WC-10VC-30Co alloy.[1]

Table 1 compares the results from the present WC-10VC-Co grade alloy with results obtained from previously examined WC-10VC-Co grades.[2] The empirical formula obtained from our EDS measurements is $(V_{0.69},W_{0.28},Co_{0.03})C_{1-x}$. From the XRD measurements the lattice parameter of this material is 4.21 ± 0.01 A. This is consistent with previous findings[3] according to which the lattice parameter of $(V_{0.68},W_{0.30},Co_{0.02})C_{0.71}$ and $(V_{0.73},W_{0.26},Co_{0.01})C_{0.73}$ after a 5 hours heat treatment was 4.20 ± 0.01 A. The compositions in ref. 3, are likely to be close to the equilibrium composition of this material. Therefore, our results suggest that at 30 wt% Co, (V,W,Co)C can reach an equilibrium composition even after only 1 hour of sintering

Table 1 suggests a trend towards larger amounts of cobalt in the (V,W,Co)C phase with increasing cobalt content.

From SEM studies, the size of the (V,W,Co)C grains was found to increase with cobalt content. For the WC-10VC-30Co material, the (V,W,Co)C grains were fairly uniformly distributed having a grain size up to about 1 μm, see Fig. 1.

Initial TEM investigations suggest a similar microstructure of the mixed carbide grains for all the WC-10VC-Co alloys. That is, essentially a defect free structure.

Financial support from NRF and Vanitec are gratefully acknowledged.

References

1. Broccardo, S. An investigation into the corrosion resistance of WC-VC-Co hardmetals. (2003) MSc dissertation, University of Witwatersrand.
2. Witcomb, M.J., Balke, P., Luyckx, S.B., Cornish, L.A. and Whitefield, D. (1997) Proc. Microsc. Soc. South. Afr. 27, 28.
3. Zinyana, J., Broccardo, S., Hamar-Thibault, S., Cornish, L.A., Witcomb, M.J., Allibert, C.H. and Luyckx, S.B. (2003) Int. Plansee Seminar, 4, 291-298.

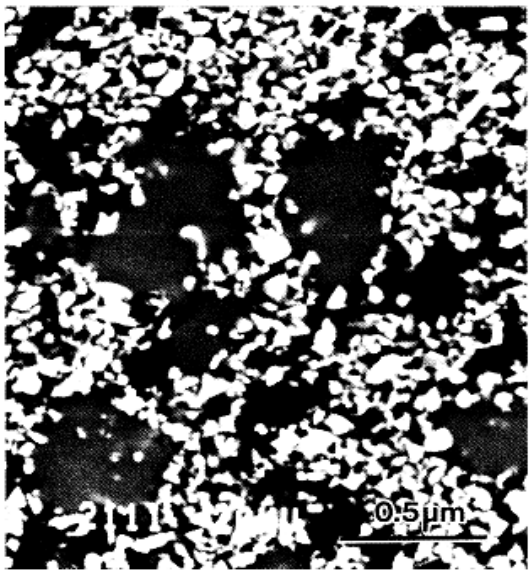


Figure 1. SEM backscattered electron mode image of the WC-10VC-30Co alloy, showing WC (light), (V,W,Co)C (grey) and Co (dark).

Table 1. Mixed carbide compositions in the different Co content WC-VC-Co alloys.

Co (wt %)	Compositions in (V,W,Co)C (at.%)		
	V	W	Co
10	59.2 ± 6.6	39.4 ± 3.3	1.4 ± 0.2
12	55.8 ± 5.5	41.8 ± 4.3	2.4 ± 0.2
15	54.7 ± 5.2	42.7 ± 4.3	2.6 ± 0.5
30	68.6 ± 0.7	28.4 ± 0.5	3.0 ± 0.5

DIFFERENCE IN MICROSTRUCTURE OF WC-30Co AND WC-VC-30Co ALLOYS

T.T. Sebeya[1,2], M.J. Witcomb[2], L.A. Cornish[1,2] and M. Hermann[3]

[1]School of Chemical and Metallurgical Engineering, University of the Witwatersrand, Johannesburg, [2]DST/NRF Centre of Excellence in Strong Materials, University of the Witwatersrand, Johannesburg, [3]Fraunhofer Institute, Dresden, Germany

WC-VC-Co of equal cobalt content with WC-Co has superior hardness, toughness and corrosion resistance[1]. The addition of VC improved the corrosion resistance of WC-Co[2]. This difference in corrosion resistance was presumed to be caused by a higher fcc/hcp Co ratio in the alloys with VC, since fcc Co was more corrosion resistant than hcp Co[1,3] although the difference was small. The current investigation was carried out to compare the microstructures of WC-Co and WC-10VC-Co at 30% cobalt content, and relate them to reported corrosion behavior, which for ~10% Co showed no significant difference[1]. Here, the two alloys were characterized by TEM, SEM, and by Rietveld XRD to derive the ratio between the fcc Co and hcp Co structures.

Table 1 shows that the fcc : hcp ratio in WC-10VC-30Co was higher than in WC-30Co, agreeing with previous work[1,3] that VC helped to stabilize fcc Co, since the ratio of fcc/hcp cobalt increased when VC was added. Earlier results[1] showed that fcc cobalt promotes better corrosion resistance than hcp cobalt. When the difference in the fcc/hcp Co ratio was small, as for the 10wt% Co alloys, the difference in their corrosion resistance was small[1]. However, with the larger difference (≈ 2.3) for the 30wt% Co alloys, the corrosion resistance of WC-10VC-30Co was much higher.

TEM studies of the WC-30Co revealed a high density of stacking faults, the hcp form of Co, in the fcc Co binder (Fig. 1). The Co phase in the WC-10VC-30Co alloy (Fig. 2) was expected to have fewer hcp stacking faults, since VC is known to stabilize fcc cobalt. The WC-30Co hardmetal had stacking faults on more than one plane, whereas WC-10VC-30Co only had visible stacking faults on one plane. However, only one orientation is shown. Additionally, the Co grains studied were much larger in WC-Co.

EDX showed that Co in WC-30Co had 8.3±1.2wt% W, whereas no W was detected in WC-10VC-30Co. No vanadium was detected in Co in either alloy. Tungsten stabilized high temperature fcc Co in conventional WC-Co[4], which did not happen here, due to the larger Co content (30wt%).

The results of the TEM study gave no additional information for the difference in corrosion resistance, and it can only be assumed that the tungsten solubility in cobalt impaired the corrosion resistance in the conventional alloy.

References

1. Broccardo, S. (2003) MSc dissertation, WITS.
2. Konado, D.S. *et al.* (2010) Corr. Sci. 52, 3118.
3. Human, A. M. (1994) PhD thesis, Technical University of Darmstadt.
4. Rettenmayr, R., Exner, H.E. and Mader, W. (1988) Mat. Sci. Tech. 4, 984.

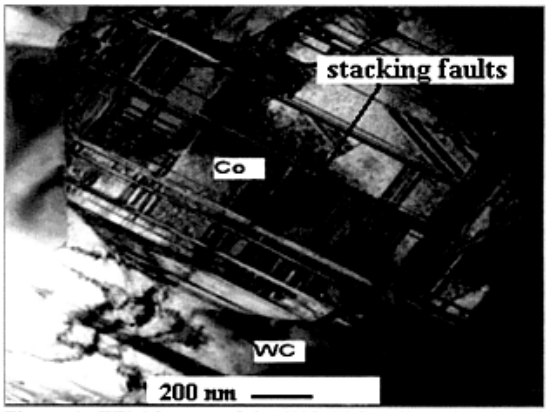


Figure 1. TEM image of the WC-30Co alloy showing fcc Co with hcp stacking faults.

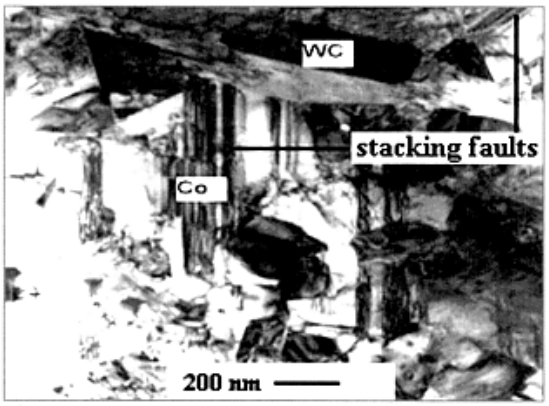


Figure 2. TEM image of the WC-10VC-30Co alloy showing parallel hcp stacking faults in fcc Co.

Table 1.Ratio of fcc-Co to hcp-Co by Rietveld XRD.

Specimen (wt%)	fcc Co/hcp Co
WC-30Co	2.5/27 = 0.09
WC-10VC-30Co	3.5/16.5 = 0.21

Corresponding author: *ThaboS@consol.co.za*